Event topology dependence of J/ψ production in proton+proton collisions at $\sqrt{s} = 13$ TeV with ALICE at the LHC and Study of elliptic flow in heavy-ion collisions using event shape and machine learning techniques

Ph.D. Thesis

By

NEELKAMAL MALLICK

DEPARTMENT OF PHYSICS

INDIAN INSTITUTE OF TECHNOLOGY INDORE

July 2024

Event topology dependence of J/ψ production in proton+proton collisions at $\sqrt{s} = 13$ TeV with ALICE at the LHC and Study of elliptic flow in heavy-ion collisions using event shape and machine learning techniques

A THESIS

Submitted in partial fulfillment of the requirements

for the award of the degree

of

DOCTOR OF PHILOSOPHY

by

NEELKAMAL MALLICK

DEPARTMENT OF PHYSICS

INDIAN INSTITUTE OF TECHNOLOGY INDORE

July 2024

INDIAN INSTITUTE OF TECHNOLOGY INDORE

I hereby certify that the work which is being presented in the thesis entitled **Event topology dependence of J/ψ production in proton+proton collisions at $\sqrt{s} = 13$ TeV with ALICE at the LHC and Study of elliptic flow in heavy-ion collisions using event shape and machine learning techniques** in the partial fulfillment of the requirements for the award of the degree of **DOCTOR OF PHILOSOPHY** and submitted in the **DEPARTMENT OF PHYSICS**, **Indian Institute of Technology Indore**, is an authentic record of my own work carried out during the time period from June 2019 to July 2024 under the supervision of Prof. Raghunath Sahoo, Professor, Department of Physics, Indian Institute of Technology Indore.

The matter presented in this thesis has not been submitted by me for the award of any other degree of this or any other institute.

Neelkamal Mallick 18/07/24

Signature of the student with date

(Neelkamal Mallick)

This is to certify that the above statement made by the candidate is correct to the best of my knowledge.

RSahoo 18.07.2024

Signature of Thesis Supervisor with date

(Prof. Raghunath Sahoo)

Mr. Neelkamal Mallick has successfully given his Ph.D. Oral Examination held on 18th July 2024

RSahoo 18.07.2024

Signature of Thesis Supervisor with date

(Prof. Raghunath Sahoo)

Dedicated

to my parents, and my little brother, with love,

to my esteemed teachers, with gratitude,

and

to my late aunt Ms. Anima Swain, with reminiscence.

ACKNOWLEDGEMENTS

Finally, the day has come to acknowledge everyone who has immensely impacted my journey through the entire tenure of my Ph.D. here at IIT Indore. I express my heartfelt gratitude to all of them who have been kind enough to help me in the most significant academic journey of my life. Although I am careful to recall everyone's contribution, I may be forgiven if I fail to acknowledge someone.

First and foremost, I sincerely thank my thesis supervisor and our team leader, Prof. Raghunath Sahoo, for his invaluable guidance, everlasting support, and continuous encouragement during the journey of my Ph.D. His expertise and knowledge in the subject have always been instrumental in shaping this work. He has gone to extremes and often beyond his comfort to help me finish things in time and stand for me even in matters related to individual interests. He is always a phone call away and eager to listen to me. He has offered me more opportunities and resources than I ever asked for, which helped me enhance my skills and profoundly helped me in my research. I sincerely acknowledge his understanding and kindness towards me, which made my Ph.D. journey more comfortable and enjoyable. I can not thank him enough through words to bring out the best in me, yet I would always carry his teachings and advice in my mind and heart.

In 2007, in primary school, I learned about the world's most powerful particle accelerator, the Large Hadron Collider, CERN, Switzerland. Today, I feel privileged to work in the ALICE collaboration at the LHC. I thank DST and DAE, Govt. of India, and IIT Indore, for whom I could participate in the experimental analysis and data-taking operations by visiting ALICE at CERN. I extend my sincere gratitude to the Conveners of Dileptons and Quarkonia Physics Working Group, Dr. Cristiane Jahnke and Dr. Luca Micheletti, and previous Conveners, Dr. Laure Marie Massacrier and Dr. Fiorella Fionda, and to the co-ordinators of Quarkonium to muon decays Physics Analysis Group, Dr. Maxime Rene Josep Guilbaud and Dr. Batoul Diab, for invaluable help and guidance in the matters of this experimental analysis.

I want to extend my heartfelt thanks and gratitude to Prof. Gergely Gábor Barnaföldi for giving me an opportunity to work with him and inviting me to the Wigner Research Center of Physics, Budapest. I have learned a lot from him, not only physics but also professionalism, discipline, and a lot of the history of Hungary. He supported me in every way possible, which made my work life and stay in Budapest comfortable and productive. I also acknowledge the support from the IITI-Wigner RCP MoU for research. A special shout out to Akos, Gábor, Balazs, Muneeb, Archana, and Naina for their help and support during my stay in Budapest. I also gratefully acknowledge the usage of computational resources provided by the Wigner Scientific Computing Laboratory (WSCLAB) at the HUN-REN Wigner RCP, Budapest. I am grateful to Prof. Tamas Biro and Prof. Guy Paic for all our discussions and their invaluable advice in pursuing a career in science. I thank Prof. Antonio Ortiz for all the discussions and support during the work of event-shape analysis, a subject of which he is a pioneer.

I want to thank my PSPC members, Dr. Dipankar Das and Dr. Sumanta Samal, for their excellent comments and constructive criticisms during my presentations related to the thesis. I would also like to thank all the esteemed faculty members of the Department of Physics, IIT Indore, especially Prof. Manavendra Mahato and Dr. Dipankar Das, for their outstanding teaching and guidance during the coursework. I want to thank Mr. Vedprakash and Mr. Prashant for handling the official paperwork at IIT Indore, which eased my life. I also thank Prof. Suhas Joshi, Director, IIT Indore, for attending my Ph.D. open seminar and providing his invaluable insights and suggestions.

I am sincerely grateful to my seniors, Dr. Sushanta Tripathy, Dr. Aditya Nath Mishra, and Dr. Arvind Khuntia, as they always helped me get in the right direction whenever I felt troubled and helped me solve many issues related to my analyses. I also thank Dr. Dhananjay Thakur, Dr. Rutuparna Rath, and Dr. Suman Deb for all their help and guidance during my Ph.D. I extend my sincere gratitude to all my lab mates, Dr. Captain Rituraj Singh, Dr. Jayanta Dey, Girija, Dushmanta, Suraj, Debadatta, Kshitish, Kamaljeet, Bhagyarathi, Kangkan, Aswathy, and Purnima for maintaining a friendly environment in the lab. Working with you has been an outstanding experience, and I thank you all for your suggestions and criticisms during many discussions in our lab. Special thanks to Aswathy, Kshitish, and Suraj for preparing a few figures and diagrams, which are part of this thesis.

I would also like to thank my teacher, Dr. Tejraj Patra, whose lectures piqued my curiosity about pursuing a career in physics. I am grateful to my late teacher, Mr. Santosh Dash, for all his teachings, encouragement, and advice.

I sincerely thank Dr. Gayatri Sahu for her kind help and support during my stay at IIT Indore. I shall always cherish all the beautiful and fun moments with Mamun and Papun.

I sincerely appreciate my parents and little brother for their unwavering support, faith, and understanding. Their struggles and sacrifices have always been the driving force for me. They are indeed the unsung heroes of my life. Their love, care, and optimism have encouraged me on my scientific journey. I sincerely thank Saswati for all her love, care, patience, and affection. She always motivated me to move forward and be a better person. I would also like to thank Saroj for always being there for me and for all the fun moments we spent together; he is a true friend for life.

This thesis would not have been possible without the collective support of all these individuals and institutions. Thank you all for being a part of this journey.

(Neelkamal Mallick)

ABSTRACT

Studies related to heavy-ion collisions at the most powerful particle accelerators in the world, the Large Hadron Collider (LHC) at CERN, Switzerland, and the Relativistic Heavy Ion Collider (RHIC) at BNL, USA, have primarily focused on the creation and properties of the primordial matter consisting quarks and gluons. This extremely dense and hot state of thermalized partons is also known as quark-gluon plasma (QGP). Due to the shorter lifetime of QGP, experiments rely on several indirect signatures that hint towards the formation of QGP in ultra-relativistic collisions of nuclear matter. While the formation of QGP has been established for a long time in heavy-ion collisions, its presence in small collision systems still needs to be determined. However, recent measurements of heavy-ion-like behavior in high-multiplicity pp collisions at the LHC have drawn the attention of the heavy-ion physics community. The appearance of ridge-like structures and the enhancement of strangeness add to these speculations.

Increased production of strange hadrons can only be explained via forming a strongly interacting medium at thermal and chemical equilibrium. To determine whether the underlying physics processes involved in the strangeness production can also be probed with topological event selection instead of the average charged-particle multiplicity, a relatively new event shape classifier has been introduced at the LHC, known as the transverse spherocity (S_0). This event-shape observable can decouple the jet-dominated events from the events with spherical soft emission of particles. The first event is called the jetty type, and the latter is called the isotropic type. Jetty events result from enhanced contributions of perturbative QCD processes; however, isotropic events arise due to the interplay of several soft QCD processes, such as the multi-parton interactions and the initial and final state radiations. It is found that the production rates of strange particles are slightly higher for soft isotropic events and highly suppressed in hard jetty events. This supports the hypothesis that in high-multiplicity pp collisions,

heavy-ion-like effects such as strangeness enhancement and radial flow are manifested in the isotropic events. Thus, transverse spherocity can separate events based on azimuthal topology and control heavy-ion-like effects in high-multiplicity pp collisions.

A similar study of strange hadron production with topological event selection can also be performed for the case of charm hadrons. In the presence of QGP, the yield of charmonium ($c\bar{c}$) is suppressed compared to the yield in the non-QGP scenarios in hadronic collisions. Therefore, studies involving charm hadrons with different topological event selections can help us understand its production mechanism and constrain various phenomenological models. Additionally, it can help us understand the observed heavy-ion-like effects in isotropic events in high-multiplicity pp collisions at the LHC. With these motivations, this analysis measures the $p_{\rm T}$-differential yield of inclusive J/ψ as a function of transverse spherocity in high-multiplicity pp collisions at $\sqrt{s}$ = 13 TeV with ALICE. For this analysis, the reconstruction of J/ψ is performed through the electromagnetic decay channel, $J/\psi \rightarrow \mu^{+}\mu^{-}$, B.R. = $(5.961 \pm 0.033)\%$ in forward rapidity, $2.5 < y < 4.0$, using the forward muon spectrometer. For the estimation of transverse spherocity, midrapidity tracklets ($|\eta| < 0.8$) are reconstructed using the Silicon Pixel Detector (SPD), which is the innermost central barrel detector in ALICE. The V0 scintillator detectors with a pseudorapidity coverage of $2.8 < \eta < 5.1$ (V0A) and $-3.7 < \eta < -1.7$ (V0C) have been used for the estimation of event multiplicity.

Such event shape-based analysis can also be implemented in heavy-ion collisions for different purposes. The appearance of strong transverse collectivity in non-central heavy-ion collisions is considered to be another signature of QGP. In non-central heavy-ion collisions, the initial spatial anisotropy gets converted into the final state momentum anisotropy during the medium evolution process and is reflected in the azimuthal momentum distribution of the charged particles. This is quantified as the anisotropic flow coefficients. To study the effect of topological event selection on the anisotropic flow coefficients, we implement transverse spherocity-based event shape analysis in heavy-ion collisions. Using transverse spherocity as an event shape tool, this study will complement the current event shape approach based on flow vectors in heavy-ion collisions. We report an extensive study of transverse spherocity dependence of elliptic flow of charged particles in Pb–Pb collisions at $\sqrt{s_{\mathrm{NN}}}$ = 5.02 TeV using a multiphase transport model (AMPT). The elliptic flow for identified light-flavor hadrons and their number-of-constituent-quark scaling are also investigated in different event classes using transverse spherocity at RHIC and LHC energies. This study implements the two-particle correlation method to extract the transverse momentum differential elliptic flow coefficients. The two-particle correlation method helps in removing substantial nonflow from the calculation using a relative pseudorapidity cut between the particle pairs.

Over the years, special attention has been given to the theoretical understanding of elliptic flow by modeling the medium evolution through relativistic hydrodynamics and various transport models. From the experimental side, the standard event plane method or the complex reaction plane identification method, the multi-particle correlation, and the cumulant method are usually followed to estimate elliptic flow. For the first time, we implement a feed-forward deep neural network to estimate the elliptic flow coefficient from the final state particle kinematics in heavy-ion collisions. The flow coefficients are embedded in the final state multi-particle correlations; hence, a deep neural network can be trained on simulated data to learn these correlations and efficiently measure the flow coefficients. The machine learning (ML) model is trained on simulated minimum bias Pb–Pb collisions at $\sqrt{s_{\mathrm{NN}}}$ = 5.02 TeV using the AMPT string melting model. After successful training, the same ML model is applied across several collision systems at RHIC and LHC energies. Since elliptic flow has several dependencies, such as centrality, transverse momentum, particle species (or mass), and collision energy, it is interesting to explore the prediction capability of the ML model in these sectors. The model predictions for the elliptic flow of light-flavor hadrons and the number-of-constituent-quark scaling depicting the partonic level collectivity are also covered. These results from the ML model are compared to experimental findings, wherever possible.

PUBLICATIONS

List of Publications

Publications included in this thesis

1. *"Study of J/ψ production as a function of transverse spherocity in pp collisions at $\sqrt{s}$ = 13 TeV"*, **Neelkamal Mallick** and Raghunath Sahoo. https://alice-notes.web.cern.ch/node/1491 [ALICE Collaboration Internal Link] ID Number: ANA-1491.

2. *"Study of Transverse Spherocity and Azimuthal Anisotropy in Pb-Pb collisions at $\sqrt{s_{\rm NN}} = 5.02$ TeV using A Multi-Phase Transport Model"*, **Neelkamal Mallick**, Raghunath Sahoo, Sushanta Tripathy, and Antonio Ortiz, J.Phys.G **48**, 045104 (2021).

3. *"Event topology and constituent-quark scaling of elliptic flow in heavy-ion collisions at the Large Hadron Collider using a multiphase transport model"*, **Neelkamal Mallick**, Sushanta Tripathy, and Raghunath Sahoo, Eur. Phys. J. C **82**, 524 (2022).

4. *"Estimating Elliptic Flow Coefficient in Heavy Ion Collisions using Deep Learning"*, **Neelkamal Mallick**, Suraj Prasad, Aditya Nath Mishra, Raghunath Sahoo, and Gergely Gábor Barnaföldi, Phys.Rev.D **105**, 114022 (2022).

5. *"Deep learning predicted elliptic flow of identified particles in heavy-ion collisions at the RHIC and LHC energies"*, **Neelkamal Mallick**, Suraj Prasad, Aditya Nath Mishra, Raghunath Sahoo, and Gergely Gábor Barnaföldi, Phys.Rev.D **107**, 094001 (2023).

Other Publications

1. *"Inclusive, prompt and non-prompt J/ψ identification in proton-proton collisions at the Large Hadron Collider using machine learning"*, Suraj Prasad, **Neelkamal Mallick**, and Raghunath Sahoo, Phys. Rev. D **109**, 014005 (2024).

2. *"Effects of clustered nuclear geometry on the anisotropic flow in O–O collisions at the LHC within a multiphase transport model framework"*, Debadatta Behera, Suraj Prasad, **Neelkamal Mallick**, and Raghunath Sahoo, Phys.Rev.D **108**, 054022 (2023).

3. *"Probing initial geometrical anisotropy and final azimuthal anisotropy in heavy-ion collisions at Large Hadron Collider energies through event-shape engineering"*, Suraj Prasad, **Neelkamal Mallick**, Sushanta Tripathy, and Raghunath Sahoo, Phys.Rev.D **107**, 074011 (2023).

4. *"Event topology and global observables in heavy-ion collisions at the Large Hadron Collider"*, Suraj Prasad, **Neelkamal Mallick**, Debadatta Behera, Raghunath Sahoo, and Sushanta Tripathy, Sci. Rep. **12**, 3917 (2022).

5. *"Predictions on global properties in O+O collisions at the Large Hadron Collider using a multi-phase transport model"*, Debadatta Behera, **Neelkamal Mallick**, Sushanta Tripathy, Suraj Prasad, Aditya Nath Mishra, and Raghunath Sahoo, Eur. Phys. J. A **58**, 175 (2022).

6. *"Estimation of Impact Parameter and Transverse Spherocity in heavy-ion collisions at the LHC energies using Machine Learning"*, **Neelkamal Mallick**, Sushanta Tripathy, Aditya Nath Mishra, Suman Deb, and Raghunath Sahoo, Phys.Rev.D **103**, 094031 (2021).

7. *"A new logistic growth model applied to COVID-19 fatality data"*, S. Triambak, D.P. Mahapatra, **N. Mallick**, and R. Sahoo. Epidemics **37**, 100515

(2021).

8. *"Role of clustered nuclear geometry in particle production through p–C and p–O collisions at the Large Hadron Collider"*, Aswathy Menon K R, Suraj Prasad, **Neelkamal Mallick**, and Raghunath Sahoo, arXiv:2407.03823 [hep-ph].

9. *"A machine learning-based study of open-charm hadrons in proton-proton collisions at the Large Hadron Collider"*, Kangkan Goswami, Suraj Prasad, **Neelkamal Mallick**, Raghunath Sahoo, and Gagan B. Mohanty, arXiv:2404.09839 [hep-ph] [Phys. Rev. D (In press)].

10. *"Investigating radial-flow-like effects via pseudorapidity and transverse spherocity dependence of particle production in pp collisions at the LHC"*, Aswathy Menon K R, Suraj Prasad, Sushanta Tripathy, **Neelkamal Mallick**, and Raghunath Sahoo, arXiv:2309.08336 [hep-ph].

11. *"First implementation of transverse spherocity analysis for heavy-ion collisions at the Large Hadron Collider energies"*, **Neelkamal Mallick**, Sushanta Tripathy, Raghunath Sahoo, and Antonio Ortiz, arXiv: 2001.06849 [hep-ph].

Conference Proceedings

1. *"A machine learning approach in estimating the coefficient of azimuthal anisotropy in heavy-ion collisions"*, **Neelkamal Mallick**, Suraj Prasad, Aditya Nath Mishra, Raghunath Sahoo, and G. G. Barnaföldi, DAE Symp.Nucl.Phys. **67**, 1091 (2024).

2. *"A Deep Learning Based Estimator for Elliptic Flow in Heavy Ion Collisions"*, **Neelkamal Mallick**, Suraj Prasad, et al., PoS LHCP2022, 259 (2023).

3. *"Studying the constituent-quark scaling of elliptic flow with transverse spherocity in heavy-ion collisions at the RHIC and LHC energies"*, **Neelkamal Mallick**, Sushanta Tripathy, and Raghunath Sahoo, DAE Symp.Nucl.Phys. **66**, 960 (2023) [**Recipient of Best Poster Award**].

4. *"Estimation of impact parameter and transverse spherocity in heavy-ion collisions at the LHC using machine learning techniques"*, **Neelkamal Mallick**, Sushanta Tripathy, et al., DAE Symp.Nucl.Phys. **65**, 642 (2022).

5. *"Dynamics of Hot QCD Matter – Current Status and Developments"*, Santosh K. Das, Prabhakar Palni, ..., **Neelkamal Mallick**, ..., et al., Int.J.Mod.Phys.E **31**, 12 (2022).

6. *"Transverse spherocity dependence of azimuthal anisotropy in heavy-ion collisions at the LHC using a multi-phase transport model"*, **Neelkamal Mallick**, Raghunath Sahoo, Sushanta Tripathy, and Antonio Ortiz, PoS LHCP2021, 227 (2021).

7. *"Implementation of machine learning techniques to predict impact parameter and transverse spherocity in heavy-ion collisions at the LHC"*, Aditya Nath Mishra, **Neelkamal Mallick**, Sushanta Tripathy, Suman Deb, and Raghunath Sahoo, PoS LHCP2021, 265 (2021).

8. *"Pseudorapidity and transverse spherocity dependence of particle production in proton+proton collisions at the LHC"*, Aswathy Menon K. R., Suraj Prasad, **Neelkamal Mallick**, Sushanta Tripathy, Raghunath Sahoo, DAE Symp.Nucl.Phys. **67**, 1029 (2024).

9. *"A review on event shape studies in ultra-relativistic collisions at the LHC energies"*, Sushanta Tripathy, Suraj Prasad, **Neelkamal Mallick**, Bhagyarathi Sahoo, Raghunath Sahoo, DAE Symp.Nucl.Phys. **67**, 1135 (2024).

10. *"Studying the dependence of transverse spherocity on the initial and final state anisotropies in heavy-ion collisions"*, Suraj Prasad, **Neelkamal Mallick**, Sushanta Tripathy, Raghunath Sahoo, DAE Symp.Nucl.Phys. **67**, 1133 (2024).

11. *"Effects of α–cluster geometry on the azimuthal anisotropy in O–O collisions at the LHC"*, Debadatta Behera, Suraj Prasad, **Neelkamal Mallick**, Raghunath Sahoo, DAE Symp.Nucl.Phys. **67**, 1043 (2024).

12. *"Segregating the topological productions of J/ψ at the Large Hadron Collider using machine learning""*, Suraj Prasad, **Neelkamal Mallick**, Raghunath Sahoo, DAE Symp.Nucl.Phys. **67**, 989 (2024).

13. *"Transverse spherocity dependence of global observables in heavy-ion collisions at the LHC using AMPT model"*, Suraj Prasad, **Neelkamal Mallick**, et al., PoS LHCP2022, 331 (2023).

14. *"Global properties in O+O collisions at $\sqrt{s_{\rm NN}} = 7$ TeV using AMPT model"*, Debadatta Behera, **Neelkamal Mallick**, et al., PoS LHCP2022, 305 (2023).

15. *"Transverse spherocity dependence of the global observables in heavy-ion collisions at the LHC"*, Suraj Prasad, **Neelkamal Mallick**, et al., DAE Symp.Nucl.Phys. **66**, 1016 (2023).

16. *"Global properties in O+O collisions at $\sqrt{s_{\rm NN}} = 7$ TeV using a multi-phase transport model"*, Debadatta Behera, **Neelkamal Mallick**, et al., DAE Symp.Nucl.Phys. **65**, 718 (2022).

Contents

List of Figures

List of Tables

Chapter 1

Introduction

1.1 Preamble

Particle physics deals with the study of *"elementary"* particles and their interactions or the fundamental forces responsible for the existence of the entire Universe. Elementary particles are *point-like* objects with no substructure. The history of the hunt for elementary particles dates back to the discovery of *electrons* by J. J. Thomson in 1897. A few years later, from the α-particle scattering experiment of Rutherford, the existence of a hard, tiny, and heavy atomic center, known as the nucleus, was confirmed. Evidently, Rutherford named the nucleus of the lightest atom (hydrogen) as *proton*. This was followed by the discovery of *neutron* – an electrically neutral twin of proton, in 1932 by Chadwick. The electron, proton, and neutron were then believed to be the basic constituents of ordinary matter. In the next few years, with the rapid developments in the theory of relativity, quantum mechanics, and nuclear physics, the existence of many new particles and their anti-particles were postulated. Thanks to the experiments with cosmic rays, most of them were discovered sooner or later. The study of particle physics further blossomed with the advancement of high-energy particle accelerators and state-of-the-art detection techniques. It turns out that four fundamental forces, strong, electromagnetic, weak, and gravitational, govern the various interactions among these particles and are responsible for all the physical processes and structures in the Universe, starting from the subatomic domain to the massive galaxies and beyond.

1.2 Standard Model of particle physics

The Standard Model of particle physics is the theory of elementary particles and the three fundamental interactions – strong, electromagnetic, and weak [1]. Developed in the 1970s, the Standard Model could practically account for all the experimental results from high-energy particle experiments [2–4]. The Standard Model is based on quantum field theory with the gauge symmetry $SU(3)\times SU(2)\times U(1)$. According to this model, all elementary particles can be divided into two groups based on their spin. These are the half-odd integer spin particles or the *fermions* and the integer spin particles or the *bosons*. As shown in Fig. 1.1, there are 12 fundamental fermions – six *leptons* and six *quarks*, divided into three generations. Leptons carry integer electrical charge, and they interact via electromagnetic and weak interactions. The negatively charged leptons are the electron, muon, and tauon (e^-, μ^-, τ^-), and the neutral leptons are the neutrinos. These neutrinos are left handed (ν_e^L, ν_μ^L, ν_τ^L). Similarly, their anti-particles are positively charged leptons (e^+, μ^+, τ^+) and right-handed anti-neutrinos ($\bar{\nu_e}^R$, $\bar{\nu_\mu}^R$, $\bar{\nu_\tau}^R$).

Quarks (q) carry fractional electrical charges. There are six flavours of quarks namely *up* (u), *down* (d), *charm* (c), *strange* (s), *top* (t), and *bottom* (b) and their respective anti-quarks ($\bar{q}$). The u, c, and t quarks carry $+2e/3$ electrical charge while the d, s, and b quarks carry $-1e/3$ electrical charge. Quarks combine to form hadrons. Hadrons are divided into mesons, which are bound states of a pair of quark and anti-quark ($q\bar{q}$), and baryons (or anti-baryons), which are bound states of three quarks (qqq) (or anti-quarks, $\bar{q}\bar{q}\bar{q}$). Since quarks are spin half

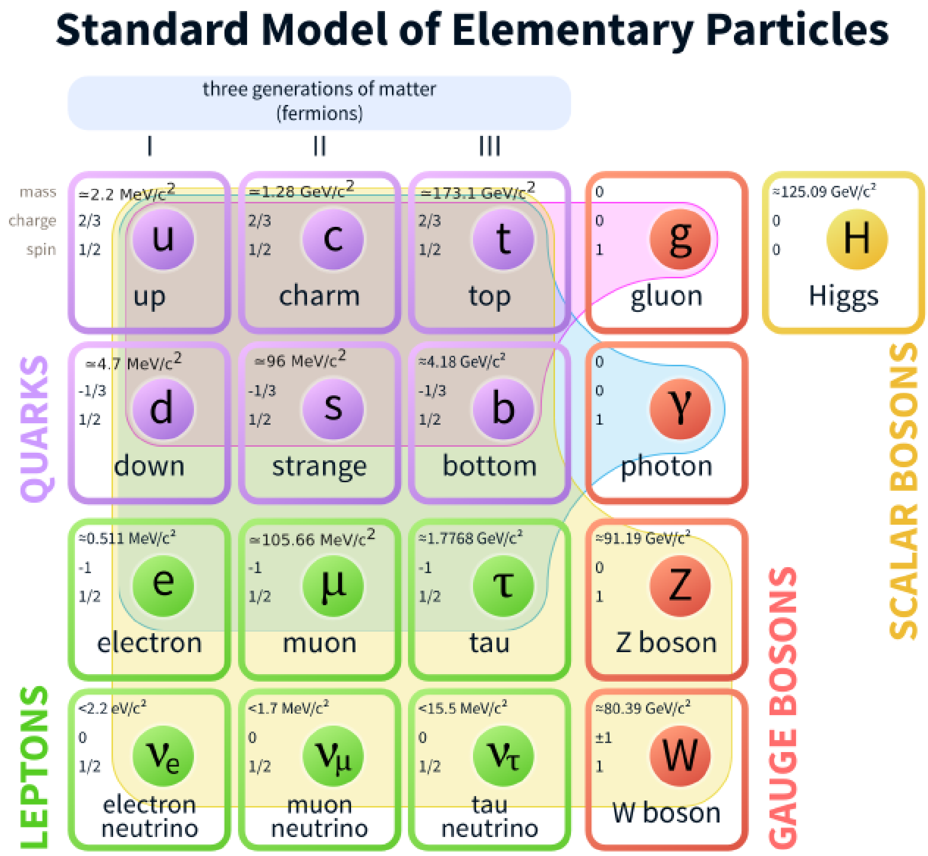

Figure 1.1: Schematic representation of the elementary particles in the Standard Model.

particles, they follow Pauli's exclusion principle just like the leptons. In the case of a baryon, all three quarks can not be identical. Therefore, quarks have an additional quantum number known as the *color* charge. There are three types of color charges: red ($r = +1$), green ($g = +1$), and blue ($b = +1$). An anti-quark carries a negative color charge ($r = -1$, $g = -1$, or $b = -1$). All naturally occurring hadrons are color-neutral. To become color neutral, a pair of quarks having equal and opposite color charges should be present (*e.g.*, $r\bar{r}$), or all three quarks should carry color in equal amounts (e.g., rgb). Thus, each quark can carry one unit of color charge along with its fractional electrical charge. Due to the presence of color charges, quarks can interact via all three interactions present in the Standard Model, *i.e.*, strong, electromagnetic, and weak interactions. Both leptons and quarks have three generations with a mass hierarchy. The ordinary matter consists of the first generation of leptons and quarks. Due to their higher mass, the second and third-generation leptons and quarks are unstable, and they decay quickly to the first-generation leptons and quarks, which are stable.

The description of the Standard Model seems incomplete without a discussion of the fundamental interactions. In quantum mechanics, the interaction among fermions is understood via the exchange of characteristic vector bosons. In the Standard Model, the vector bosons are *photon* (γ), *gluon* (g), $W^{\pm}$ and Z^0 bosons. Elementary particles with electrical charges interact via electromagnetic interactions, which are mediated via photons. Thus, leptons and quarks that have electrical charges can interact via electromagnetic interactions. Neutrinos are excluded as they are charge-neutral. Photons are chargeless, massless particles, and they do not self-interact. The theory of electromagnetic interactions is Quantum Electrodynamics (QED) and is described with Abelian gauge theory with symmetry group $U(1)$. The weak interactions are slow processes mediated by massive vector gauge bosons, $W^{\pm}$ and Z^0. They are responsible for nuclear β decays involving neutrinos and also flavour-changing decays of quarks. In the 1960s, the electromagnetic interaction was unified with the weak interaction with symmetry group $SU(2) \times U(1)$ by Sheldon Glashow, Abdus Salam, and Steven Weinberg, which is popularly known as the electroweak unification. This states that the electromagnetic force and the weak force are two aspects of the single electroweak force. Finally, as the name suggests, the strong interaction is the strongest fundamental interaction, and particles with color charges can only interact via strong interactions. This is mediated via gluons, which are massless and electrically chargeless particles, yet they carry net color charges. Due to this reason, gluons can self-interact, and the theory of strong interaction – Quantum Chromodynamics is described with a non-Abelian *SU(3)* symmetry group. Quarks, gluons, and hadrons can interact via strong interaction; however, this is limited to a small range ($\leq 10^{-15}$ m).

1.3 Quantum Chromodynamics (QCD)

The theory of strong interaction is described by Quantum Chromodynamics (QCD). This is a quantum field theory with $SU(3)$ gauge symmetry. It explains the interaction of elementary particles with color charges such as quarks, gluons, and hadrons. The color conservation rule applies to all processes involving strong interaction. QCD belongs to a special class of field theories known as *gauge field theories* in which the Lagrangian is invariant under local gauge transformation. This invariance is termed as *gauge invariance* [5]. This requires that the quanta of the gauge field should be massless. Thus, just like photons in QED, gluons are massless in QCD. Since gluons carry one unit of both color and anti-color charges, there should be $3^2 = 9$ gluons. However, this is not the case, as one state corresponds to a colorless singlet state in the form of $r\bar{r}+g\bar{g}+b\bar{b}$; hence, there are only eight gluons. The possibility of having a massless colorless gluon is also ruled out, as the existence of such a gluon will lead to a long-range (strong) interaction between the colorless hadrons, which is not observed. In QED, photons do not carry any electrical charges. Thus, there are no first-order photon-photon interactions. However, gluons have self-interactions, thanks to their color degrees of freedom, and this makes the QCD processes more complex. Now, we proceed to discuss two of the most important aspects of QCD: confinement and asymptotic freedom.

1.3.1 Confinement

One of the fundamental features of QCD is that under ordinary conditions, quarks can not be isolated from the hadrons, meaning they are always confined within the hadronic dimension. In fact, no single isolated quark has ever been observed experimentally. This is known as *"quark confinement"* [5]. The QCD static potential can be written as follows [6],

$$V_{\text{QCD}}(r) = -\frac{4}{3}\frac{\alpha_s}{r} + kr. \tag{1.1}$$

Here, α_s is the strong coupling parameter, k is the color string tension constant ($\simeq$ 0.85 GeV fm^{-1}), and r is the distance between the interacting partons[1]. The first term, similar to Coulomb potential, arises due to single-gluon exchange at smaller r. The second term, which is linear in r, leads to the confinement of quarks. Since, at a large distance, the second term dominates, and the QCD potential grows larger, making the overall interaction attractive. At large r, the color field lines between two interacting partons are squeezed to form color tubes due to the gluon-self interaction. In other words, the effective color field grows at large r. As a consequence, the energy provided in separating the partons favors the creation of a quark and anti-quark pair instead of producing two free partons. Now, to explain how gluon-self interaction develops the color field strength at a large distance, one has to understand the phenomena of *"vacuum polarization"*. In QED, vacuum polarization refers to a process in which the background electromagnetic field produces virtual electron-positron (e^+e^-) pairs. In the presence of such virtual particles, the interaction among other particles is diminished due to a screening effect, and the effective charge distribution gets modified. This is also known as the self-energy of gauge bosons (photons). Analogically, the QCD vacuum can also produce virtual quark-anti-quark and gluon pairs. The virtual $q\bar{q}$ pairs screen the color field at a large distance, just like virtual e^+e^- pairs in QED. However, gluon self-interaction leads to an anti-screening effect, and it outweighs the screening from virtual $q\bar{q}$ at large distance [5, 6]. Therefore, it explains the increase in the strength of interaction at large distances and quark confinement.

[1]Quarks and gluons are together called as partons, named by Prof. R. Feynman.

1.3.2 Asymptotic freedom

Quark confinement also leads to an immediate conclusion that the strong coupling parameter, α_s, is not a constant. This means the effective strength of interaction between quarks and gluons depends on the distance or momentum transfer. From the interaction of high momentum electrons with quarks inside hadrons in the deep inelastic scattering experiments, it was understood that quarks inside hadrons behave in a way as if they are almost free. An interaction with high momentum transfer corresponds to an interaction at a short distance. Thus, it was understood that the interaction weakens at short distances or high momentum transfer, yet it gets extremely stronger at a larger distance scale. This is known as *"asymptotic freedom"*, and it is a characteristic feature of non-Abelian gauge theory[2] such as the QCD [5].

In general, the strong coupling parameter, $\alpha_s(Q^2)$, measured at one scale, *e.g.*, $Q^2 = \mu_0^2$, can be used to estimate the coupling at another scale, by using the so-called renormalization group equation [6]. This is known precisely only up to the first order, which is given as [7],

$$\frac{4\pi}{\alpha_s(\mu_0^2)} - \frac{4\pi}{\alpha_s(Q^2)} = \beta_0 \ln\left(\frac{\mu_0^2}{Q^2}\right). \tag{1.2}$$

Here, $\alpha_s(\mu_0^2)$ is the measured value of the strong coupling parameter at momentum transfer μ_0^2. This can be further simplified using the QCD *scale parameter*, Λ, as follows [7].

$$\alpha_s(Q^2) = \frac{4\pi}{\beta_0 \ln(Q^2/\Lambda^2)} \tag{1.3}$$

Here, $\Lambda^2 = \mu_0^2 \exp\left(-4\pi/\beta_0\alpha_s(\mu_0^2)\right)$, and $\beta_0 = \left(11 - \frac{2}{3}n_f\right)$ given the computation is done only with *one-loop* effective coupling of the gluon propagator [7]. n_f is the number of flavors. From Eq. 1.3, it is clear that the strong coupling constant, $\alpha_s(Q^2)$, depends on both momentum transfer (Q) and the scale parameter

[2]In a non-Abelian gauge theory, the operators of the gauge field do not commute.

(Λ). Now, at asymptotically large momentum transfer (large Q^2), the coupling $\alpha_s(Q^2) \to 0$, making the effective interaction so small that quarks behave as if free. However, $\alpha_s(Q^2)$ becomes very large at low Q^2 (or at a large distance). The experimental data supporting this behavior of the coupling parameter is shown in Fig. 1.2. The value of the strong coupling parameter around the Z^0 boson mass is also shown, which is $\alpha_s(M_Z^2) = 0.1179 \pm 0.0009$.

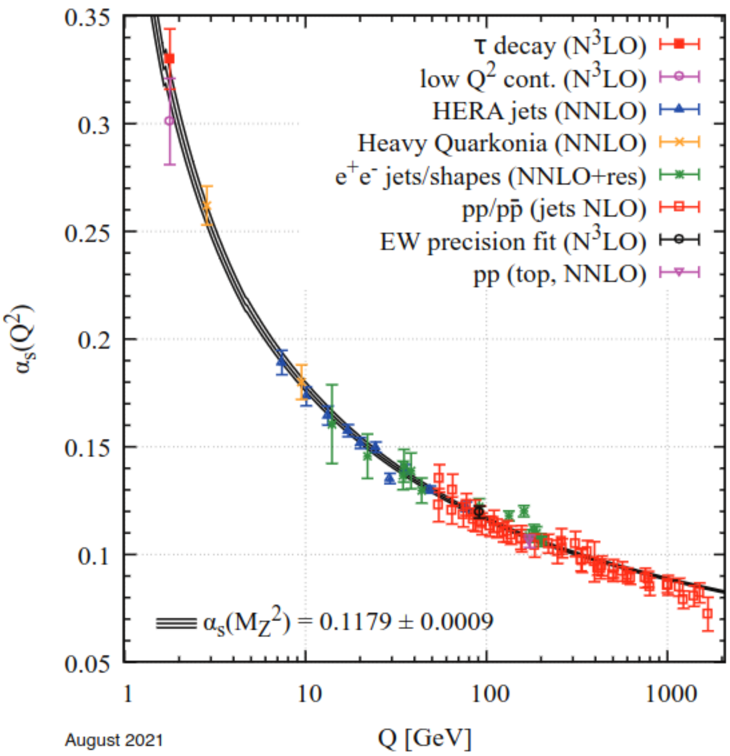

Figure 1.2: Running coupling constant $\alpha_s(Q^2)$ plotted as a function of momentum transfer (Q), extracted using different degrees of QCD perturbation theory which are mentioned in the legend [8].

1.4 Quark-gluon plasma (QGP)

Interactions involving high momentum transfer (large Q^2) can make quark matter behave as if it is almost free, thanks to asymptotic freedom. In fact, QCD predicts the existence of a deconfined phase of the quark matter under extreme conditions such as at high temperature (T) and high baryon chemical potential (μ_B). This phase of the QCD matter is believed to have existed in the microsecond ($\sim 10^{-6}$ s) old Universe just after the *Big Bang*, when the temperature of the Universe was extremely high ($\sim 10^{12}$ K)[3]. In this phase, hadrons melt down to produce a hot and dense soup of quarks and gluons, thus leading to the manifestation of their color degrees of freedom beyond hadronic dimensions. This phase of locally thermalized and deconfined quark matter is known as quark-gluon plasma (QGP). Evidently, a phase transition from a state of confined color singlet hadrons to QGP is thus anticipated. In fact, ultra-relativistic heavy-ion collisions provide enough energy density (or temperature) for the formation of QGP. The details of this will be covered in the next section. Here, we would like to focus on the QCD phase diagram.

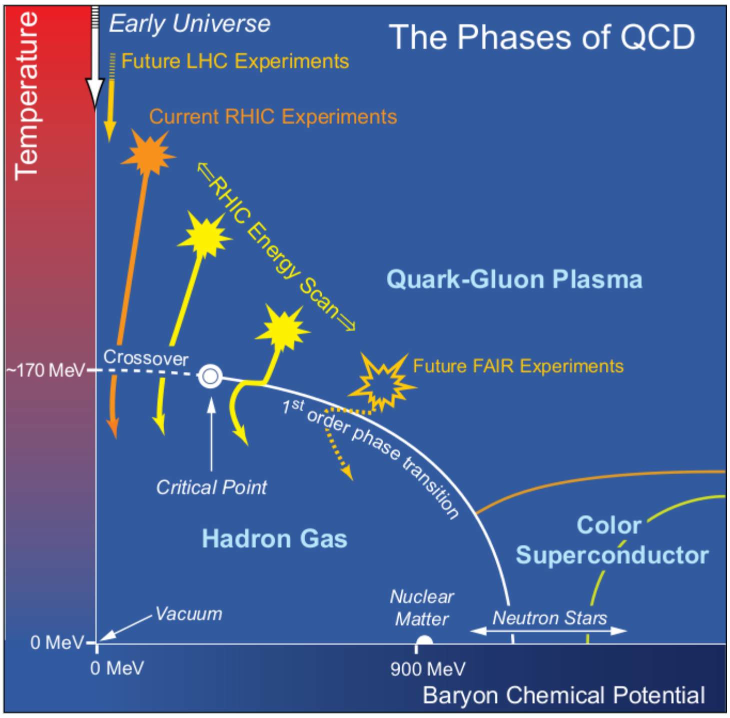

Figure 1.3: Conjectured QCD phase diagram [9].

[3]The temperature of the core of the Sun is $\sim 1.5 \times 10^7$ K.

Figure 1.3 shows the conjectured QCD phase diagram for various combinations of T and μ_B. Generally, temperature is associated with the energy density of the system due to the microscopic kinetic motion of its constituents[4]. The baryon chemical potential determines the energy required to add or remove a baryon at fixed pressure and temperature. At low T and low μ_B, quarks are confined inside hadrons, which is the state of nuclear matter under ordinary conditions. At $\mu_B \sim 0$ and high temperature, the phase diagram corresponds to the early Universe scenario, and under such conditions, the quarks and gluons are already deconfined to form the QGP phase. Such conditions are made possible in collisions of nuclear matter at ultra-relativistic speeds. Again, at $\mu_B \sim 0$, lattice QCD predicts a smooth crossover phase transition between the hadron phase to the QGP phase at $T \sim (150 - 160)$ MeV [10, 11]. This is shown as dashed lines in Fig. 1.3. However, at high μ_B, there is a conjectured first-order phase transition between the hadron phase and the QGP phase, shown as a solid line in Fig. 1.3. A first-order phase transition is characterized by the appearance of discontinuity in the first-order derivative of the free energy of the system. In a crossover phase transition, such discontinuity is not observed; hence, some call this an analytical crossover instead of an actual phase transition [11]. Additionally, there exists a *critical point* in the QCD phase diagram at which the first-order phase transition changes its characteristics. The precise location of the QCD critical point is still unknown, yet lattice QCD model predictions report that the location of the critical point is within the range of T and μ_B accessible at RHIC energies. The search for this critical point is one of the important objectives of the Beam Energy Scan (BES) program at RHIC [12], the discovery of which shall mark a landmark achievement.

Finally, Fig 1.4 shows the lattice QCD predictions for the QCD equation-of-state (EoS) using (2+1) flavor calculations at vanishing μ_B [13]. The solid

[4] Absolute zero (0 K) is the temperature at which all microscopic movements of the matter cease to exist.

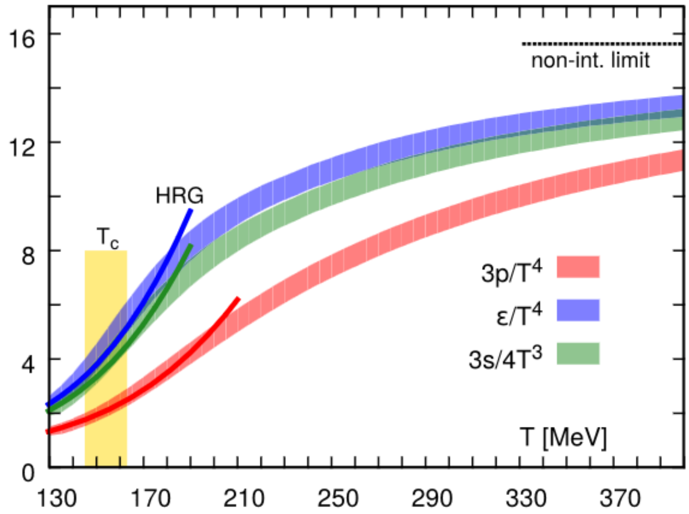

Figure 1.4: Lattice QCD predictions for the normalized pressure, energy density, and entropy density as a function of temperature at vanishing μ_B. The solid lines show the predictions from the Hadron Resonance Gas (HRG) model [13].

lines represent the predictions from the Hadron Resonance Gas (HRG) model. The observables shown in the plot correspond to the number of thermodynamic degrees of freedom of the QCD matter at a given temperature. The rapid (continuous) rising trends of the thermodynamic quantities such as the normalized pressure ($3p/T^4$), energy density (ϵ/T^4), and entropy density ($3s/4T^3$) as a function of temperature reflect the rapid increase in the number of degrees of freedom of the system at higher temperature due to the phase transition (or analytical crossover) of the hadronic matter to the QGP phase. The sharp rising trend begins to appear around $T \sim 155$ MeV, suggesting the beginning of a smooth crossover from the hadronic phase to the QGP phase at this temperature. At a high T limit, the QCD EoS approaches $\epsilon = 3p$, which is expected for massless particles; however, it is far from the Stefan-Boltzmann limit for being treated as an ideal (non-interacting) gaseous state.

1.5 Heavy-ion collisions

Over the last couple of decades, studies involving high-energy nuclear collisions have provided a wealth of information on various aspects of QGP [14–16]. By colliding the nuclei of heavier elements (or heavy ions) at ultra-relativistic speeds, experiments can achieve the necessary energy density required for producing a deconfined phase of the QCD matter at high temperature and $\mu_B \sim 0$. As an outcome of such violent interactions of nuclear matter, a multitude of final-state particles are formed. The goal of experiments is then to study the debris of such collisions through various observables and look for possible explanations using theoretical and phenomenological models [17]. The evolution from QGP to the final-state hadrons is a dynamic process, and the spacetime evolution of heavy-ion collisions is briefly described below.

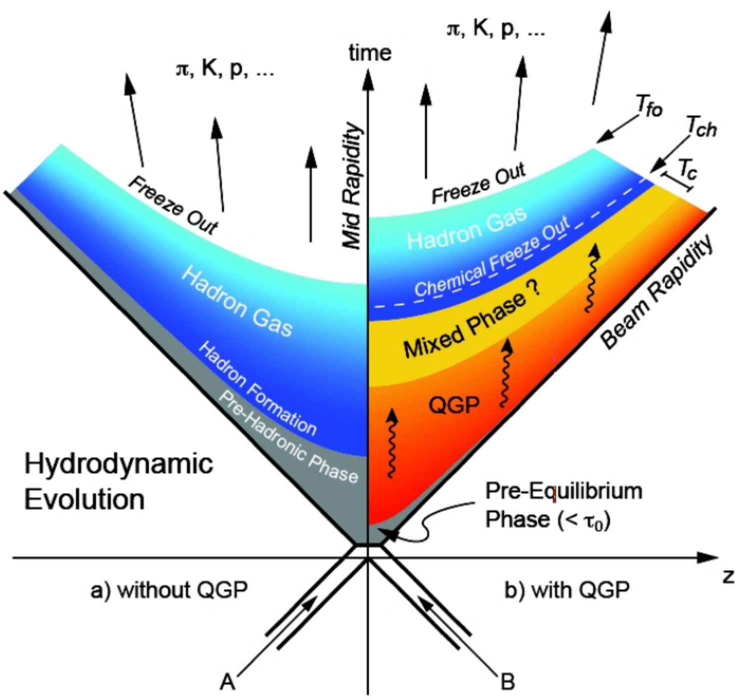

Figure 1.5: Schematic representation of the spacetime evolution of relativistic hadronic and nuclear collisions [18].

Figure 1.5 shows the schematic representation of the spacetime evolution of relativistic hadronic and nuclear collisions. On the left side, the evolution process involving no QGP phase has been shown, whereas the right side shows the complete evolution picture for collisions involving the formation of QGP. First, let us focus on the system evolution with the QGP medium, which is described as follows.

- **Pre-equilibrium dynamics:** Just after the collision of two Lorentz contracted nuclei, the system undergoes multiple hard partonic interactions in the collision overlap zone. A significant amount of kinetic energy is deposited at the collision point, which provides enough energy density to melt the hadrons and liberate the partons; yet, the partons are not (locally) thermalized in this phase. Creation of heavier quarks such as *charm* and *beauty* also takes place in this phase due to the availability of a huge amount of initial energy density. The exact processes involved in the pre-equilibrium phase are still not very well known. However, studies involving the Glauber model [19] and Color Glass Condensate (CGC) [20] are the popular approaches in describing this initial state of the collision. The typical time scale of this phase is about $\tau \leq 1$ fm/c.

- **Evolution of QGP:** The produced partons from the initial interactions are further scattered among themselves, which leads to the local thermalization of the fireball. At this point, QGP is supposed to have been formed. Thus, its evolution can be described by relativistic viscous hydrodynamics with dissipative effects [21]. During this phase, partons undergo both inelastic and elastic collisions, and the flavor composition of the QGP keeps on changing. The QGP phase continues to exist until $\tau \leq 10$ fm/c, after which the hydrodynamic evolution of the fireball is not applicable anymore. The upper time limit of the QGP phase varies with the centrality and center-of-mass energy of the collisions.

- **Hadronization and freezeout:** As the fireball expands and cools down further, the energy density of the system falls below a level where partons can no longer stay deconfined. Thus, the coupling constant, α_s, becomes strong enough to begin the binding of partons into hadrons. This process of parton to hadron conversion is called *hadronization*. There are two possible pictures of hadronization, namely recombination and fragmentation. The recombination process leads to the production of hadrons from the quark coalescence mechanism by combining nearby partons in the phase space to form hadrons. This usually is applicable for the hadrons produced at low to intermediate p_{T}. At high-p_{T}, hadronization occurs through the fragmentation of the color flux tubes. Fragmentation takes place when the color strings formed between the leading (or high-p_{T}) quark-antiquark (or quark-diquark) pairs are pulled apart so strongly that the color field splits into producing particle-antiparticle pairs out of the QCD vacuum. The newly produced partons can then combine to form hadrons with well-defined quantum numbers. Once all the partons are converted into hadrons, *chemical freezeout* occurs, and the corresponding temperature is denoted as T_{ch}. The produced hadrons then undergo further evolution through elastic collisions. Unstable particles and resonances undergo decay during this evolution process. Once the mean free path of the hadrons exceeds the system size, *kinetic freezeout* occurs, and the hadrons emerge with fixed momenta. The corresponding temperature is denoted by T_{fo}. Only a handful of stable hadron species are then detected and measured in the detector. All other particles from their decay daughters can be reconstructed using the invariant mass reconstruction technique. The evolution of particles in the hadron gas phase is usually modeled with relativistic transport model descriptions based on the Boltzmann equation [22].

The left side of Fig. 1.5 shows the spacetime evolution of a system without

QGP. This case is suitable for low-energy heavy-ion or hadronic collisions, where the necessary energy density requirements for the deconfinement phase transition from hadronic to the partonic phase are not satisfied. In such collisions, there might be a possibility of deconfinement of the partons, yet the small system size does not allow thermalization of the medium. Hence, hydrodynamic descriptions are not applicable. Such a system undergoes a pre-hadronic phase with dominant hadronic productions, followed by a hadron gas phase involving hadron-hadron interactions and finally freezeout.

1.6 Signatures of QGP

Due to the short timescale of strong interaction, which is of the order of a few fm/c, the existence of any direct probe for the detection and study of the properties of the QGP phase is impossible. In the absence of any direct measurements, experiments rely on studying several indirect signatures through the production of final-state charged particles, leptons, or photons, which hint towards the formation of QGP in high-energy nuclear collisions. Some of the key signatures depicting the formation of QGP medium in ultra-relativistic collisions of nuclear matter are briefly discussed below.

1.6.1 Strangeness enhancement

The enhanced production of strange hadrons in heavy-ion collisions has long been considered one of the most spectacular signatures of the formation of QGP. This is usually studied through the yield ratio of strange and multi-strange hadrons (*e.g.* $K^{\pm}$, K^0_{s}, $\Lambda+\bar{\Lambda}$, $\Xi^-+\bar{\Xi}^+$, $\Omega^-+\bar{\Omega}^+$) to non-strange hadrons (*e.g.* $\pi^++\pi^-$). However, recent measurements with ALICE have reported a similar level of strangeness enhancement in high-multiplicity proton+proton (pp) and p–Pb collisions as that of Pb–Pb collisions at the LHC [23, 24]. The same is shown in

Fig. 1.6. As the formation of QGP is already established in Pb–Pb collisions at the LHC, these results have triggered new questions. Whether the formation of QGP is overlooked in small collision systems is yet to be re-examined.

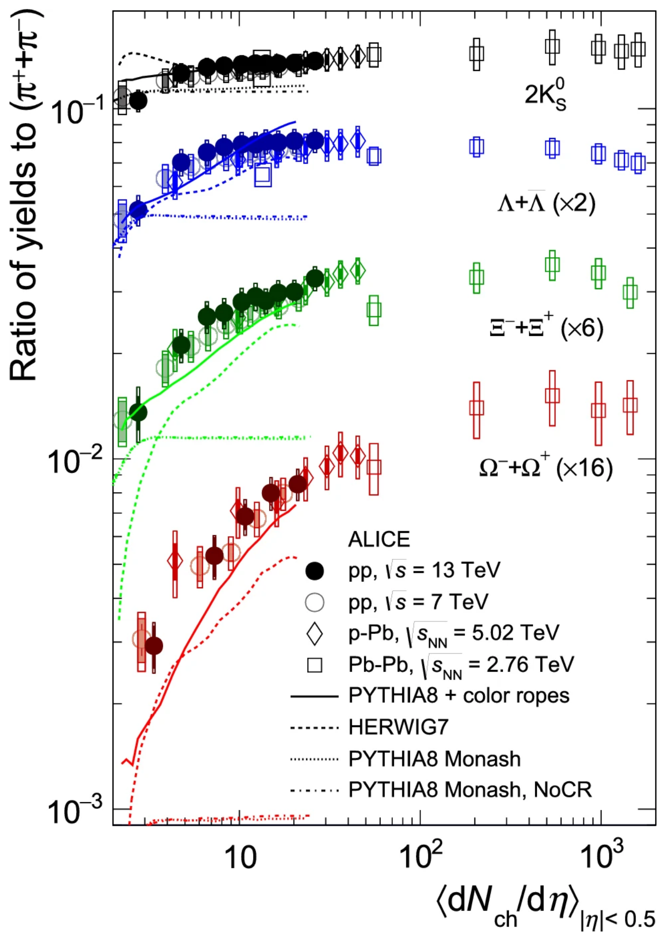

Figure 1.6: Multiplicity dependent yield ratios of strange and multi-strange hadrons to $(\pi^+ + \pi^-)$ in pp, p–Pb, and Pb–Pb collisions at the LHC [23, 24].

In nuclear collisions under no QGP scenario, strangeness enhancement can occur only if the hadron gas phase gets enough time so that the inelastic hadronic collisions can drive the system toward chemical equilibrium. This process turns out to be extremely slow. Estimates show that the chemical equilibration time in the hadronic gas phase for multi-strange hadrons such as Ω–baryon can take as long as 100 fm/c [25, 26]. Thus, the typical small time scale of heavy-ion collisions

($\sim 10 - 15$ fm$/c$) is not sufficient enough to explain the observed strangeness enhancement if no QGP scenario is imposed. However, if QGP is formed, the strangeness equilibration will proceed very fast, mainly due to the following two reasons: the gluon flavor democracy and consequences from the chiral symmetry restoration [27]. The first case is due to the availability of large gluon density in QGP, which results in efficient production of strangeness through gluon fusion, $gg \rightarrow s\bar{s}$ [5]. The second case related to the chiral symmetry restoration ensures a decrease in the energy threshold for the strangeness production in QGP as compared to that of pure hadron gas scenario [27]. Hence, strangeness enhancement is always associated with the presence of deconfined QCD matter under thermal and chemical equilibrium.

1.6.2 Anisotropic flow

The appearance of strong transverse collectivity in non-central heavy-ion collisions is considered to be another signature of QGP [28]. This transverse collectivity of the system is anisotropic. Thus, it is often called the anisotropic flow. In non-central heavy-ion collisions, the nuclear overlap region looks like an ellipsoid that has initial spatial anisotropy. In the presence of QGP, this initial spatial anisotropy induces a strong differential pressure gradient inside the medium. Thus, the initial spatial anisotropy gets converted into the final state momentum anisotropy during the medium evolution process and is reflected in the azimuthal momentum distribution of the charged particles [29]. The predictions for the nonvanishing anisotropic flow coefficients can be explained by evolving the QGP medium with relativistic hydrodynamics. For this, the thermalization of the medium is evident. Hence, the presence of finite anisotropic flow indeed reflects the presence of early thermalization of the deconfined QCD medium.

Since this thesis deals with the study of elliptic flow in heavy-ion collisions, which is the second-order anisotropic flow coefficient, the necessary descriptions and formulation of this quantity have been covered in Chapter 4 and 5.

1.6.3 Jet quenching

In the context of high-energy nuclear collisions, jets are a collimated spray of high-p_{T} partons, often produced back-to-back to conserve four momenta. It has been observed that the evolution of jets in heavy-ion (A-A) collisions is very different from that of pp collisions. In the absence of any medium, any dijet produced in pp collisions will deposit two back-to-back sharp energy peaks in the calorimeter. However, when a dijet is produced inside QGP, the jet that traverses a longer distance inside the medium loses more energy, resulting in an imbalance in the four momenta between the two jets. Thus, the jet that loses energy appears to be suppressed in the presence of a medium. This phenomenon is called jet quenching. The interaction between the hard partons and the thermalized partons in the medium leads to both collisional and radiative energy losses [30, 31], which makes jet quenching a final-state effect.

The quenching of high-p_{T} partons leads to a suppression in the yield of final-state hadrons at high-p_{T}. This is usually reported with the nuclear modification factor R_{AA}, which is the normalized single particle yield ratio in A-A to pp collisions. R_{AA} is given as,

$$R_{\mathrm{AA}} = \frac{d^2N_{\mathrm{AA}}/(dy\ dp_{\mathrm{T}})}{\langle N_{\mathrm{coll}}\rangle\ d^2N_{\mathrm{pp}}/(dy\ dp_{\mathrm{T}})}. \tag{1.4}$$

Here, $\langle N_{\mathrm{coll}}\rangle$ is the average number of binary nucleon-nucleon collisions happening in a single nucleus-nucleus (A-A) collision. If an A-A collision is a simple superposition of many nucleon-nucleon (or pp) collisions, then $R_{\mathrm{AA}} = 1$ (no nuclear effect). However, $R_{\mathrm{AA}} < 1$ shows suppression in the yield. Figure 1.7 reports the transverse momentum dependence of R_{AA} for various particles in Au–Au collisions $\sqrt{s_{\mathrm{NN}}} = 200$ GeV from the PHENIX experiment [32]. From the figure, it is clear that there is no suppression in the case of direct photon yield since photons do not interact via strong force. However, a strong suppression in the

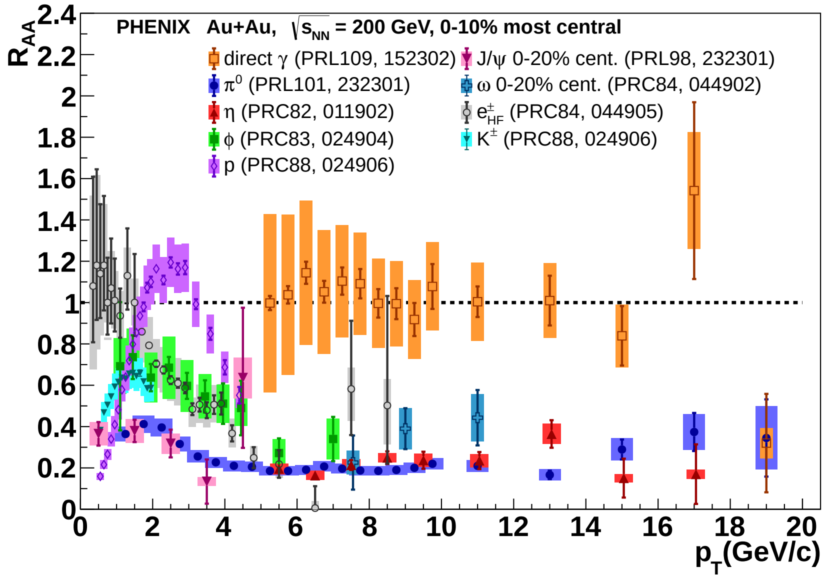

Figure 1.7: Transverse momentum dependence of nuclear modification factor for various particles in Au–Au collisions $\sqrt{s_{\mathrm{NN}}}$ = 200 GeV from the PHENIX experiment [32].

yield of high-p_{T} hadrons is observed, which is due to the jet quenching effects in the presence of QGP medium in heavy-ion collisions at RHIC. Similar results are also reported at the LHC [33, 34].

1.6.4 Quarkonia suppression

Quarkonium refers to the bound state of heavy quark and antiquark pair, mainly charmonium ($c\bar{c}$) and bottomonium ($b\bar{b}$). Long ago, the suppression of quarkonia was proposed as the signature of QGP [35]. In QGP, due to the presence of deconfined partons, the color charges screen the effective interaction between the heavy quark pairs. This makes the formation of a bound state of heavy quarks difficult as the interaction strength between Q and $\bar{Q}$ weakens. This is known as color screening or Debye screening in QCD. Additionally, the high temperature of the medium facilitates dynamic dissociation quarkonia. Together, these effects suppress the quarkonia yield in A-A collisions.

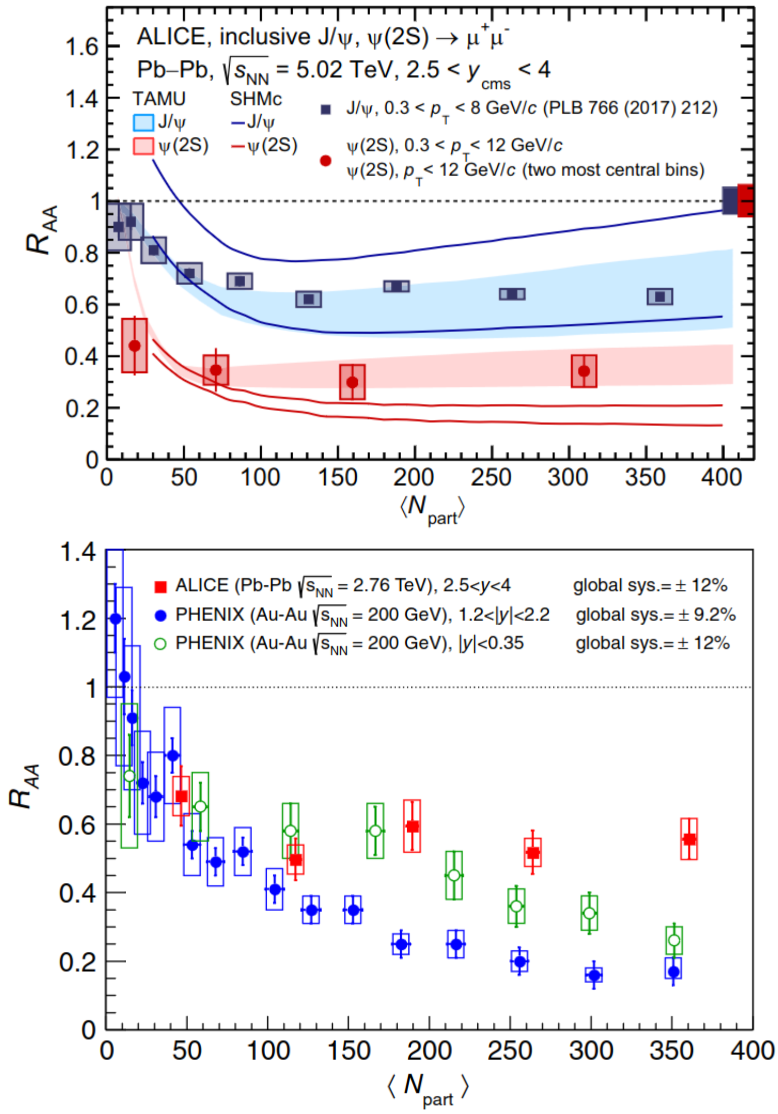

Figure 1.8: Top: The nuclear modification factor ($R_{\rm AA}$) showing the suppression of J/ψ and $\psi(2S)$ at the LHC [36]. Bottom: Inclusive J/ψ $R_{\rm AA}$ at the LHC compared to RHIC [39].

The top plot in Figure 1.8 shows the $R_{\rm AA}$ of J/ψ and $\psi(2S)$ as a function of average number of participants $\langle N_{\rm part}\rangle$[5] in Pb–Pb collisions at $\sqrt{s_{\rm NN}} = 5.02$ TeV at the LHC [36]. The result shows a clear suppression of J/ψ and $\psi(2S)$ owing to

[5] $\langle N_{\rm part}\rangle$ serves as a proxy to the centrality or multiplicity of the collisions.

the formation of QGP at the LHC. However, at the LHC, the availability of higher energy also results in a greater abundance of heavy quarks in the plasma. Thus, a slight enhancement in R_{AA} for both J/ψ and $\psi(2S)$ can be observed towards the most central collisions (higher $\langle N_{part} \rangle$). This is due to the regeneration of charmonia owing to the higher density of charm quarks in the phase space. Such regeneration effects are minimal at the RHIC energies [37, 38]. This can be seen in the bottom plot of Fig. 1.8, where the R_{AA} of inclusive J/ψ at the LHC is compared to RHIC [39]. This plot clearly shows a greater suppression of J/ψ at RHIC. Again, $\psi(2S)$ is more suppressed than J/ψ. This is due to the fact that being a radially excited state of $c\bar{c}$, $\psi(2S)$ is weakly bound as compared to J/ψ. Thus, in the presence of a hotter medium like QGP, a further decrease in its binding energy leads to a greater suppression as shown in Fig. 1.8 [31, 36].

1.7 High-multiplicity pp collisions

As discussed so far, studies related to QGP and heavy-ion physics provide an excellent opportunity to test the theory of strong interaction in both perturbative and nonperturbative domains of QCD. However, baseline measurements in small collision systems such as pp and p+A collisions are also crucial, in which the production of QGP medium is usually not anticipated. Hence, the medium effects on different physical observables can be studied by comparing the results from heavy-ion collisions with pp collisions. In the absence of QGP, particle production in pp collisions can be very different from heavy-ion collisions. However, some of the recent measurements of heavy-ion-like behavior in high-multiplicity pp collisions at the LHC have drawn the attention of the heavy-ion physics community [40–42]. Mainly, the strangeness enhancement [24] and appearance of ridge-like structures [43] add to these speculations. Additionally, from the measurement of kinetic freezeout temperature (T_{kin}) and mean radial flow velocity ($\langle \beta_T \rangle$) using Boltzmann-Gibbs Blast-wave (BGBW) fit to the identified particle

p_{T} spectra, it has been observed that (T_{kin}, $\langle\beta_{\mathrm{T}}\rangle$) correlation in high-multiplicity pp collisions approaches a similar value compared to the heavy-ion collisions [23].

Some of the theoretical understanding of these heavy-ion-like effects in high-multiplicity pp collisions come from the Underlying Event (UE) features, which have major contributions from multi-parton interactions (MPI) including color reconnection [44]. Since high-multiplicity pp events at the LHC have a dominant contribution from UE, it becomes necessary to look for other observables that can, in fact, segregate events based on the amount of UE activity in such high-multiplicity events. Recently, one such event classifier has been introduced at the LHC, which is known as transverse spherocity [45–48]. This event shape observable can decouple the jet-dominated events from the events with spherical soft emission of particles. The first kind of events are called the jetty type, and the latter is called the isotropic type. Jetty events result from enhanced contributions of pQCD processes; however, the isotropic events are UE-dominated and arise due to several soft QCD processes, such as MPI. Since the experimental analysis presented in this thesis deals with the study of charmonia production in high-multiplicity pp collisions at the LHC using transverse spherocity-based event selection, therefore, more details on this subject are presented later in Chapter 3.

1.8 Organization of the thesis

This thesis consists of six chapters. The organization of the chapters in the thesis is presented below.

- **Chapter 1** gives a brief introduction to the Standard Model of particle physics, followed by a discussion on the theory of strong interaction – quantum chromodynamics (QCD). Two important aspects of QCD, *i.e.*, confinement and asymptotic freedom are emphasized. This chapter also includes a discussion on the primordial matter, quark-gluon plasma, the time evolution picture of QGP, and its various signatures. The need of studying high-multiplicity pp collisions at the LHC using event-shape observable is also mentioned.

- **Chapter 2** deals with the experimental setup. This includes an introduction to the Large Hadron Collider (LHC) followed by a description of A Large Ion Collider Experiment (ALICE). The detector systems playing a crucial role in the event-shape analysis of J/ψ have been emphasized. This also includes a note on the various dimuon triggers and the data acquisition system of ALICE.

- **Chapter 3** presents the main experimental analysis of event-topology dependence of J/ψ production in pp collisions at $\sqrt{s} = 13$ TeV with ALICE. This includes the detailed analysis methodology, estimation of spherocity, and various quality checks. Finally, the invariant mass distribution, signal extraction, evaluation of systematic uncertainty, and the yield of J/ψ in different event classes have been reported. This Chapter is based on the following analysis note.

  – *"Study of J/ψ production as a function of transverse spherocity in pp collisions at $\sqrt{s}$ = 13 TeV"*, **Neelkamal Mallick** and Raghunath Sahoo. https://alice-notes.web.cern.ch/node/1491 [ALICE Collaboration Internal Link] ID Number: ANA-1491.

- **Chapter 4** presents the phenomenological study of event-shape dependence of elliptic flow in Pb–Pb collisions at $\sqrt{s_{\rm NN}} = 5.02$ TeV. This covers a brief introduction to a multiphase transport model (AMPT) and the pQCD-based event generator, PYTHIA, for the Monte Carlo simulation of heavy-ion collisions. The detailed analysis methodology, including the estimation of spherocity and the two-particle correlation technique for flow estimation, is discussed. The results include the transverse momentum and event shape dependence of the two-particle azimuthal correlation function, elliptic flow for all charged particles, and identified light-flavor particles and their constituent quark number scaling. This Chapter is based on the following two publications.

- *"Study of Transverse Spherocity and Azimuthal Anisotropy in Pb-Pb collisions at* $\sqrt{s_{\rm NN}} = 5.02$ *TeV using A Multi-Phase Transport Model"*, **Neelkamal Mallick**, Raghunath Sahoo, Sushanta Tripathy, and Antonio Ortiz, J.Phys.G **48**, 045104 (2021).
- *"Event topology and constituent-quark scaling of elliptic flow in heavy-ion collisions at the Large Hadron Collider using a multiphase transport model"*, **Neelkamal Mallick**, Sushanta Tripathy, and Raghunath Sahoo, Eur. Phys. J. C **82**, 524 (2022).

• In **Chapter 5**, we propose a deep learning-based estimator for elliptic flow in heavy-ion collisions. A detailed description of the working of deep neural networks, event generation using AMPT, model architecture, input/output, model training, quality assurance, and evaluation of systematic uncertainty are presented. The results include the prediction of centrality and transverse momentum dependence of elliptic flow for charged particles, as well as identified light-flavor hadrons at RHIC and LHC energies. The predictions for the constituent quark number scaling, evolution of $p_{\rm T}$ crossing point, and effect of transverse-momentum-dependent training on the estimator are reported. This Chapter is based on the following two publications.

- *"Estimating Elliptic Flow Coefficient in Heavy Ion Collisions using Deep Learning"*, **Neelkamal Mallick**, Suraj Prasad, Aditya Nath Mishra, Raghunath Sahoo, and Gergely Gábor Barnaföldi, Phys.Rev.D **105**, 114022 (2022).
- *"Deep learning predicted elliptic flow of identified particles in heavy-*

ion collisions at the RHIC and LHC energies", **Neelkamal Mallick**, Suraj Prasad, Aditya Nath Mishra, Raghunath Sahoo, and Gergely Gábor Barnaföldi, Phys.Rev.D **107**, 094001 (2023).

- Finally, the conclusions drawn from the current studies are presented in **chapter 6**.

Chapter 2

Experimental setup

Research in any field of science appears deficient if the theoretical predictions are not confronted with the experimental findings. Following Einstein's famous mass-energy equivalence relation ($E = mc^2$), for the creation of a particle, one needs to pump an equivalent amount of energy into the system. This is achieved by colliding hadrons or nuclei with one another or with a fixed target at velocities close to the speed of light ($v \simeq 0.9999c$). To explore the realm of particles and the forces responsible for their interaction, experiments mainly focus on the creation and detection of a few final-state particles that are relatively stable. Further, the unstable particles can then be reconstructed from their decay products. The collider experiments, in which two counter-circulating beams of hadrons or heavy-ions collide with each other, have an advantage over the fixed target experiments, where a beam of particles collides with a stationary target. In collider experiments, the center-of-mass energy of a symmetric collision with a crossing angle of $\theta = 180°$ is given as the sum of the beam energies, *i.e.*, $E_{\rm cm} = E_{\rm beam1} + E_{\rm beam2}$. In contrast, in fixed target experiments, it is given as $E_{\rm cm} \propto \sqrt{E_{\rm beam}}$. It means collider experiments have more energy available for particle production than the fixed target experiments. Since larger center-of-mass energy favors more particle production, collider experiments are preferred. Additionally, the size of an accelerator also plays an important role since, in collider experiments, the energy of the beam obtained from the accelerator is proportional to the radius of the machine and the strength of the RF electric fields. This justifies the need for large accelerators. Further, the accelerator beams are manipulated using electromagnetic force. Thus, the need for stable charged particles such as electrons, protons, and some stable nuclei to be practically used as the accelerator beam particles is evident.

Before going to the experimental analysis presented in the next chapter, we dedicate this chapter to introducing the experimental setup. We briefly describe the Large Hadron Collider (LHC), CERN, Switzerland, and introduce A Large Ion Collider Experiment (ALICE) at the LHC. It also includes a description of the ALICE sub-detector systems used in the present analysis, followed by short notes on the trigger and data acquisition framework.

2.1 The Large Hadron Collider

The Large Hadron Collider at CERN, Switzerland, is a technological marvel dedicated to the experimental high-energy particle physics community for the study of hadronic and nuclear collisions at ultra-relativistic speeds [49]. This is truly a world-class laboratory bringing together nearly 12000 participants from 70 countries. It houses the world's most powerful particle accelerator, having a 27 km circumference, and is placed underground at a level of $50-150$ m beneath the Earth surface. Building the accelerator underground is economical, and it also provides active radiation shielding to the surface wildlife and vegetation. The machine is designed to deliver proton beams of energy up to 7 TeV[1] and Pb–ion beams of energy up to 2.76 TeV per nucleon[2]. Additionally, for bending and focus-

[1] Recently, in Run 3, the delivered energy per proton beam is 6.8 TeV, earlier it was 6.5 TeV.

[2] Only protons can be accelerated and neutrons are free riders, so, the energy per nucleon delivered by the machine for Pb ions is given by, $E_{\mathrm{Pb}} = Z/A \times E_p = 82/208 \times 7$ TeV $\simeq 2.76$ TeV.

ing the beams, the accelerator uses around 1200 super-conducting dipole magnets and delivers a peak magnetic dipole field of 8.3 T. This ensures the bending of the 7 TeV beams around the 27 km circumference with desired accuracy. To achieve such a high magnetic field, the main dipoles use niobium-titanium (NbTi) cables, which operate at a temperature around 10 K (or -263.2°C), making them super-conducting.

The two beam pipes of the LHC cross each other at four interaction points, where four particle detectors contributing to the four major experiments at CERN are situated. A Toroidal LHC Apparatus (ATLAS) and Compact Muon Solenoid (CMS) experiments focus on New Physics searches, including but not limited to the study of Higgs boson(s), Dark Matter, and Supersymmetry candidates [50, 51]. The Large Hadron Collider beauty (LHCb) experiment is dedicated to the study of CP violation in the decay of heavy-flavor hadrons, mainly using the B meson decay channel [52]. These studies attempt to solve the Matter-Antimatter Asymmetry puzzle in our Universe. Finally, A Large Ion Collider Experiment (ALICE) is a heavy-ion collision detector dedicated to the study of quark-gluon plasma, the primordial matter that was believed to be present right after the Big Bang at the very beginning of our Universe [53]. ALICE also explores the possibilities of having heavy-ion-like features in high-multiplicity pp collisions. This thesis presents the experimental analysis of J/ψ production in pp collisions at $\sqrt{s} = 13$ TeV recorded using the ALICE detector during the Run 2 operations in 2016.

Figure 2.1 shows the schematic representation of the CERN accelerator complex. The four major experiments (ATLAS, CMS, LHCb, and ALICE) are also displayed. The accelerators at the CERN complex work in succession to increase the beam energy by increasing the dimension of the accelerator rings. To obtain a beam of protons, hydrogen gas is first ionized using an electric field, which also accelerates the protons up to 750 keV. The protons are then fed to LINAC 2, which accelerates them further to 50 MeV. The proton beams then pass sequen-

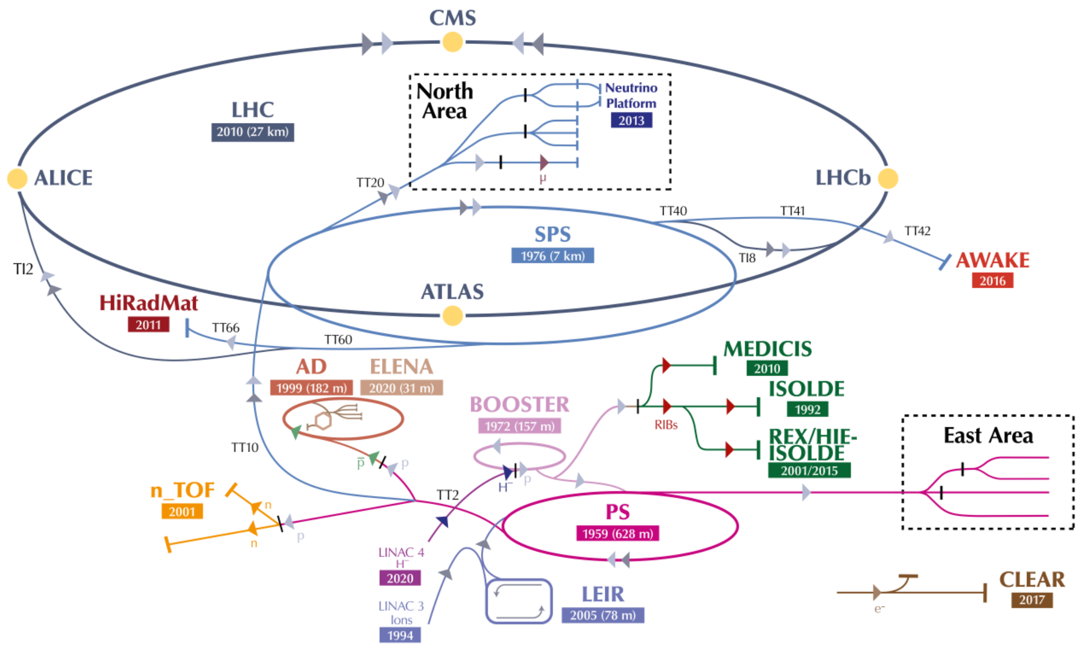

Figure 2.1: CERN accelerator complex showing the four major LHC experiments (ATLAS, ALICE, CMS, and LHCb). The Proton Synchrotron Booster (PSB), Proton Synchrotron (PS), and Super Proton Synchrotron (SPS) rings are also shown [54].

tially through the Proton Synchrotron Booster (PSB), Proton Synchrotron (PS), and Super Proton Synchrotron (SPS) to achieve an energy of 450 GeV at the end. Finally, it is injected into the LHC, which ramps up the beam energy from 450 GeV to 6.5 TeV. This process in the LHC takes just 20 minutes under nominal conditions. Similarly, Pb ions are provided by LINAC 3 and pass through the Low Energy Ion Ring (LEIR), which accelerates them up to 72 MeV. After that, the same sequential acceleration chain is performed through PS and SPS before injecting the ion beams to the LHC, where they accelerate further to reach the beam energy of 2.76 TeV per nucleon.

2.2 A Large Ion Collider Experiment

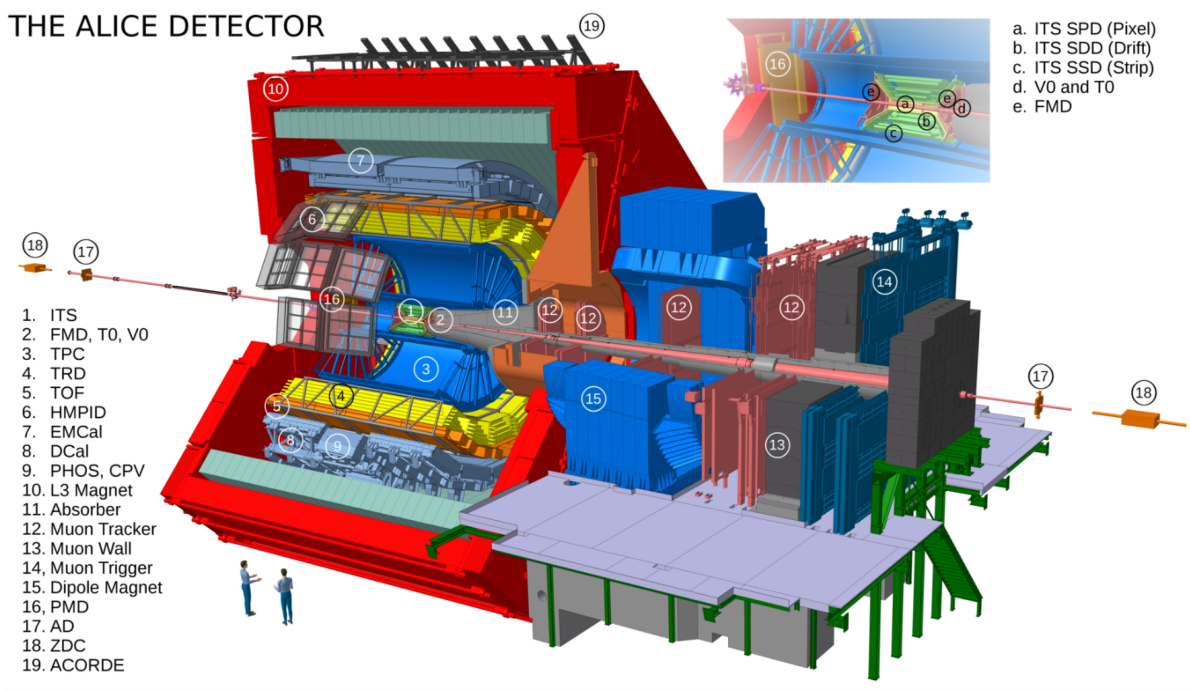

Figure 2.2: Schematics of the ALICE apparatus at the LHC (Run 2 configuration) [55].

A Large Ion Collider Experiment (ALICE) at the LHC is specifically designed to study heavy-ion collisions with an emphasis on Quantum Chromodynamics (QCD), the theory of strong interaction. ALICE studies the physics of strongly interacting matter known as quark-gluon plasma. ALICE achieves this through excellent particle identification (PID) capabilities with high momentum resolution. This also requires precision measurements in a high-charged particle density environment, which is usually anticipated in heavy-ion collisions ($dN_{\mathrm{ch}}/d\eta \simeq 2500$). In addition, baseline measurements consisting of pp and p+Pb collisions are also recorded with ALICE. The entire ALICE apparatus has an overall dimension of $16 \times 16 \times 26$ m^3 and a combined weight of $\sim$ 10,000 tons. It groups a total of 18 different detector systems (Run 2 configuration) designed for specific scientific goals. These detector systems are grouped into two major parts, *i.e.*, the central barrel detectors and the forward detectors, which are mentioned below and also shown in Fig. 2.2.

- **Central barrel detectors** are placed at midrapidity surrounding the interaction point with full azimuthal coverage. From inside out, the detectors which belong to the central barrel part are the Inner Tracking System (ITS), the Time-Projection Chamber (TPC), the Time-of-Flight (TOF), the High Momentum Particle Identification detector (HMPID), the Transition Radiation Detector (TRD), and two electromagnetic calorimeters (PHOS and EMCal). These detectors are designed to measure hadrons, electrons, and photons. All these central barrel detectors are placed inside the large solenoid magnet reused from the L3 experiment at LEP, which provides a magnetic field strength of 0.5 T.

- **Forward detectors** consist of the Zero Degree Calorimeter (ZDC), T0, V0 detectors and a dedicated muon spectrometer. They are responsible for the event plane estimation, event characterization, triggering, and muon measurements.

Presently, we proceed to emphasize only the ITS, V0, and muon spectrometer, as they play significant roles in the analysis detailed in this thesis.

2.2.1 Inner Tracking System

The Inner Tracking System (ITS) is the innermost detector of ALICE [56]. It is the closest detector to the beam pipe and the interaction point. It has a full azimuthal coverage at midrapidity, $|\eta| < 0.9$. The cylinder-shaped ALICE beam pipe is made up of beryllium with 800 μm-thickness having a 6 cm outer diameter and is placed coaxially to the ITS. Further, the ITS is divided into three subsystems with a total of six layers, namely, the Silicon Pixel Detector (SPD),

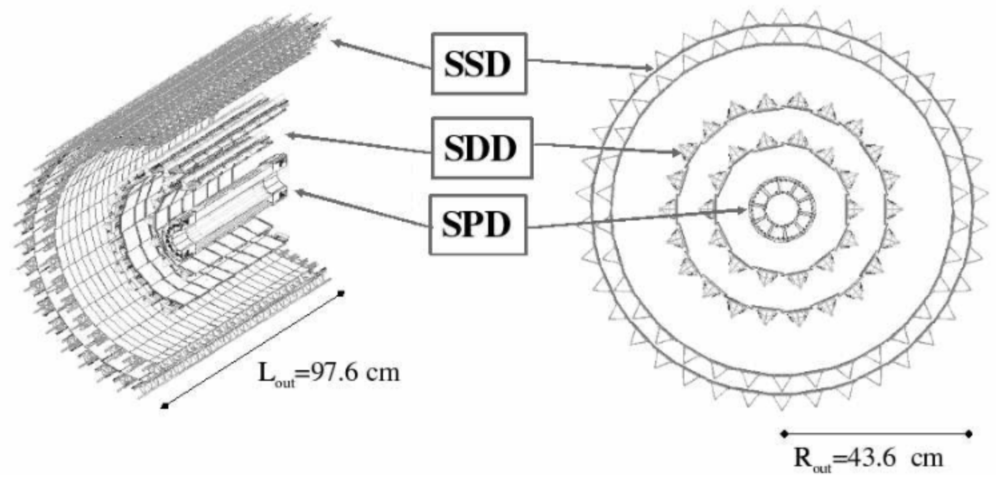

Figure 2.3: Schematics of the Inner Tracking System [53].

Silicon Drift Detector (SDD), and Silicon Strip Detector (SSD). The schematics of the ITS are shown in Fig. 2.3. Each of these subsystems has two layers. The minimum radius of the ITS is chosen so that it is placed as close as possible to the beam pipe, and the maximum radius of the ITS is optimized to provide ITS–TPC track matching. The ITS performs several important tasks, mainly the localization of the primary vertex and reconstruction of secondary vertices from strange hadron and heavy-flavour hadron decays. The four outer layers of the ITS have an analog read-out. Thus, it can track and identify low momentum particles (up to $p_{\mathrm{T}} \simeq 200$ MeV/c) through dE/dx measurements. For this reason, the ITS also works as a low-p_{T} particle spectrometer.

SPD constitutes the two innermost (first and second) layers of the ITS. The radii of the first and second layers are 3.9 cm and 7.6 cm, respectively. The first layer has an extended pseudorapidity coverage ($|\eta| < 1.98$). It provides excellent vertexing and tracking capability. In addition, it helps determine the impact parameter of secondary tracks originating from hyperon, beauty, and charm hadron decays that have smaller decay lengths. It also helps in estimating the charged particle multiplicity in midrapidity. Being close to the interaction point, it is also designed to withstand the high particle density and high radiation levels. SPD follows two different algorithms to estimate the primary vertex. The *Vertexer-SPD3D* algorithm estimates the x, y, z coordinates of the primary vertex. The algorithm selects *tracklet* candidates by connecting the two reconstructed hit points on the two layers of the SPD and uses the cut-based distance of closest approach (DCA) method to assign tracklets to the interaction point. The *VertexerSPDz* reconstructs only the z-coordinate of the SPD vertex if the *VertexerSPD3D* fails due to lesser particles than a threshold. This usually happens in pp collisions. A detailed description of these algorithms can be found in Refs. [57, 58]. Finally, SPD also helps in tagging the pile-up events when multiple vertices are found in the same event reconstruction.

2.2.2 V0 detector

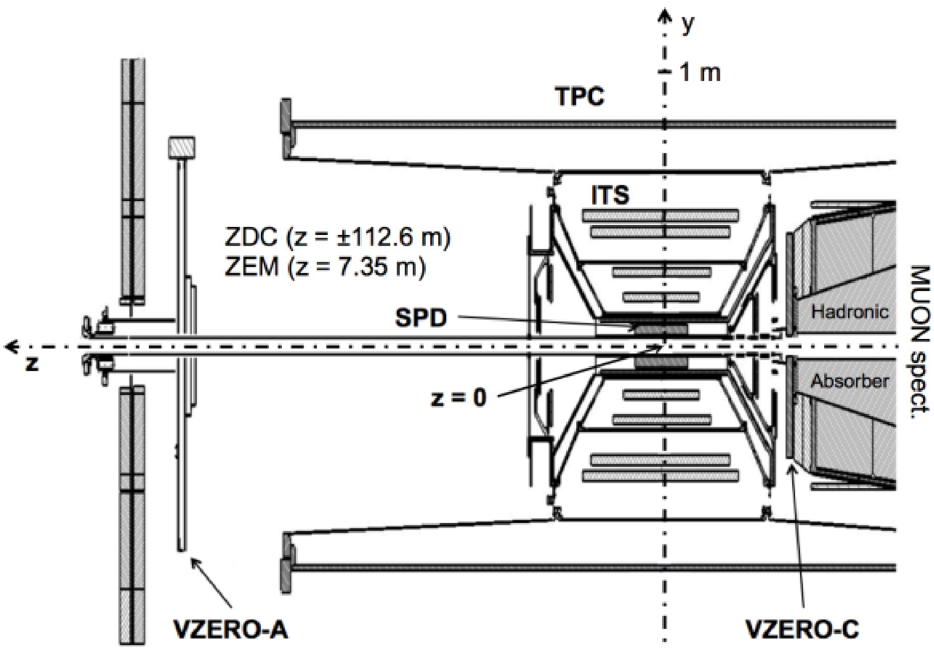

Figure 2.4: Placement of ALICE V0 detectors on either side of the interaction point [60].

The V0 detector consists of two arrays of scintillator counters located asymmetrically on either side of the ALICE interaction point [59, 60]. The placement of V0 detectors is shown in Fig. 2.4. The detector on the A-side (ATLAS-side), called V0A, is placed at $z = +340$ cm and covers the rapidity window of $2.8 < \eta < 5.1$. The detector on the C-side (CMS-side), called V0C, is situated at $z = -90$ cm and covers the rapidity window of $-3.7 < \eta < -1.7$. The V0 detector provides minimum bias triggers to ALICE central barrel detectors and also the forward muon spectrometer by segregating beam-beam interactions from beam-gas-induced background events. V0 also provides particle multiplicity (known as V0M) in the forward rapidity and can perform event characterization necessary for flow and correlation measurements. In pp collisions, V0 detectors are also used to provide an estimate of the luminosity.

2.2.3 Muon spectrometer

ALICE has a dedicated apparatus for forward rapidity detection of muons. This is known as the muon spectrometer. It can measure the complete spectrum of heavy-quark vector-mesons and their resonances, *i.e.*, J/ψ, $\psi(2S)$, $\Upsilon(1S)$, $\Upsilon(2S)$, $\Upsilon(3S)$ along with ρ, ω, and ϕ mesons in the dimuon ($\mu^+\mu^-$) decay channel [53, 61]. In addition, the unlike-sign dimuon continuum can also be measured up to masses 10 GeV/c^2. This is important as the dimuon continuum is populated via semi-leptonic decay of open charm and open beauty hadrons at the LHC energies. The design considerations include the measurement of dimuon candidates down to zero p_{T}. This is essential as the direct production of J/ψ, known as the prompt production, is dominant at low-p_{T}. At higher p_{T}, the contribution from b-hadron decays to J/ψ becomes significant, which is known as the nonprompt production. In heavy-ion collisions at the LHC energies, the high particle flux requires a large material absorber to filter out the hadrons and only allow the muons. However, the usage of a thick absorber also penalizes the low momentum muons as it does not allow muons with $p_{\mathrm{T}} < 4.0$ GeV/c to be detected. Thus, the measurement of low-p_{T} charmonia is only possible at small angles (*i.e.*, at large rapidity) at the LHC energies. Indeed, the muon spectrometer can detect muons in the pseudorapidity interval of $-4.0 < \eta < -2.5$, which corresponds to polar angle $171^{\circ} - 178^{\circ}$.

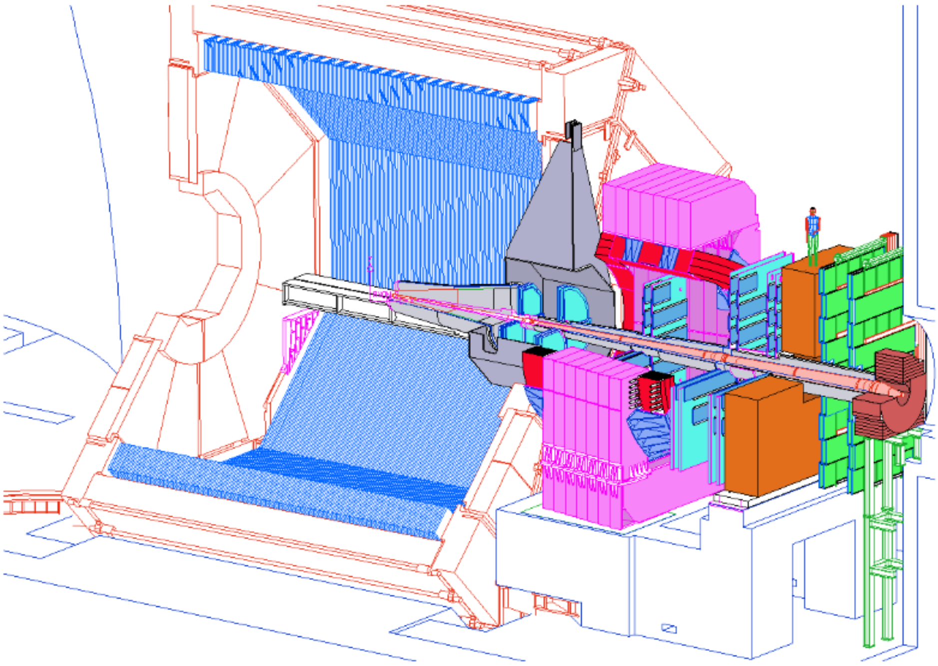

Figure 2.5: Location of the muon spectrometer and its major components in ALICE [53].

Figure 2.5 shows the location of the muon spectrometer and its major components in ALICE. The same can also be seen in Fig. 2.2. Starting from the interaction point, the muon spectrometer consists of a front absorber to filter out hadrons and photons, which is followed by a high-granularity tracking system. The tracking chamber consists of five trackers with a total of 10 detection planes. The third tracker array is housed inside a large dipole magnet. This is followed by a passive muon-filter wall made up of iron. The muon trigger system comes next in the sequence. The trigger system consists of four detection planes. It is also

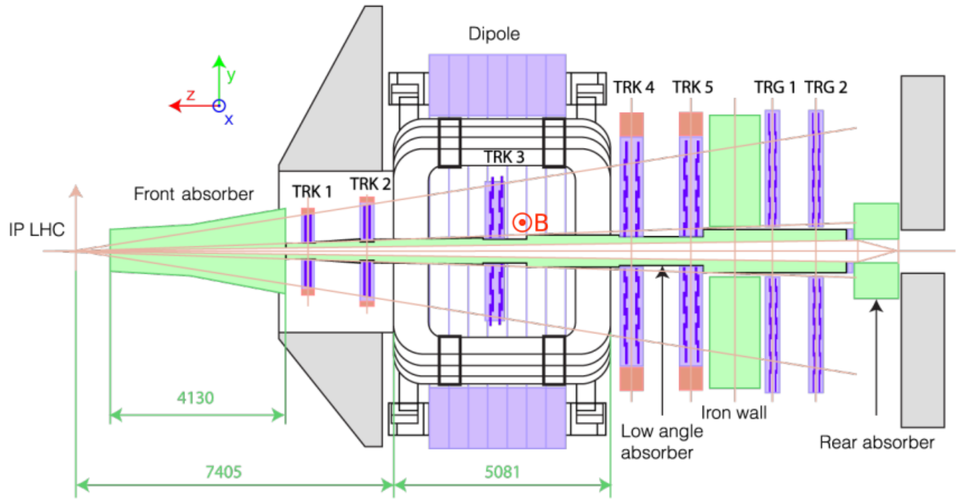

Figure 2.6: Schematics of the muon spectrometer with the layout of the front absorber, the tracking chamber, the dipole magnet, the trigger chamber, and the rear absorber [61].

protected from the back side with a rear absorber. All these major components are highlighted in Fig. 2.6. The V0 detector serves as a fast interaction trigger for the muon spectrometer. A brief description of the three main components of the muon spectrometer, *i.e.* absorbers, tracking chamber, and trigger chamber, are mentioned below.

- **Absorbers and shielding:** The muon spectrometer consists of a front and rear absorber. The front absorber is made of a conical shape that wraps the beam pipe. It is situated inside the L3 magnet at a distance $\sim$ 90 cm from the interaction point. It helps in filtering the hadron and photon flux along with muons from the decay of kaons and pions. It is also designed to block the secondary particles that are produced inside the absorber and not related to the actual beam-beam interactions. The beam pipe passing through the entire muon spectrometer is shielded with a conical tube made out of W, Pb, and stainless steel. This shielding provides necessary background reduction from particles produced at low angles due to the interaction with the beam pipe itself. The trigger station needs additional protection. Thus, it is separated from the tracking chamber by a thick iron wall of width $\sim$ 1.2 m. Finally, the rear absorber, also made out of iron, protects the trigger station from the background generated by beam-gas interactions.

- **Tracking chamber:** The tracking chamber consists of five stations of trackers, two placed just after the front absorber, one inside the dipole magnet, and two outside just before the muon filter. Each station is made out of two chamber planes. Each chamber plane consists of two cathode planes to estimate the (x, y) coordinates of the hit points. In total, the tracking chamber covers a surface area of $\sim$ 100 m^2. The first two stations are made in a quadrant structure, while the rest of the stations are made in slat architecture. The detection area of the trackers grows with increasing the distance from the IP.

- **Trigger chamber:** The need of the trigger system is to separate the unnecessary events, having only low-p_T muons, which comes mainly from the decay of kaons and pions, from the desired events having muons from the decay of heavy quarkonia (or in the semi-leptonic decay of open charm and beauty). The trigger chambers are equipped with four planes of Resistive Plate Chambers (RPCs), which are placed one meter away from each other and are situated just after the muon filter. The RPCs provide both (x, y) coordinates of the hit points and are operated in streamer mode. The total active area of the trigger chambers is $\sim$ 140 m^2. The muon trigger system provides six types of triggers to the ALICE Central Trigger Processor (CTP) based on the criteria mentioned below.

    1. At least one muon track reconstructed with p_T over low- or high-p_T threshold (0MSL/0MSH)

2. At least two unlike-sign muon tracks each reconstructed with p_{T} over low- or high-p_{T} threshold (0MUL)

3. At least two like-sign muon tracks each reconstructed with p_{T} over low- or high-p_{T} threshold (0MLL)

2.3 Trigger and data acquisition

Specific detectors are usually grouped together to form a cluster. Detectors in the same cluster contribute to simultaneous read-out. Different detectors have different responses and read-out times. But, the read out from one cluster is not affected by other detectors in other clusters. This is particularly important for fast detectors, such as SPD, MCH, and MTR. Also, the same detector can be grouped in different clusters at the same time. In ALICE, clusters define the read-out detectors, and classes define the trigger detectors. The input triggers and output clusters used in muon measurements are described below.

- CMUL7-B-NOPF-MUFAST: This dimuon trigger is fired by a coincidence of signals in both V0A and V0C detectors with a pair of unlike-sign muons satisfying the low-p_{T} threshold in the muon spectrometer.

- CMSL7-B-NOPF-MUFAST: This single muon low-p_{T} trigger is fired by a coincidence of signals coming from both V0A and V0C detectors with at least one muon satisfying the low-p_{T} threshold in the muon spectrometer.

- CMSH7-B-NOPF-MUFAST: This single muon high-p_{T} trigger is fired when a coincidence of signals coming from both V0A and V0C detectors occurs along with at least one muon satisfying the high-p_{T} threshold in the muon spectrometer.

- CMLL7-B-NOPF-MUFAST: This like-sign dimuon trigger is fired by the coincidence of signals in V0A and V0C detectors along with a pair of like-sign muons satisfying the low-p_{T} threshold in the muon spectrometer.

As already described, these trigger classes and detector clusters are used to characterize certain events of interest. Once such triggers are issued, the job of the ALICE data acquisition system (DAQ) is to process the data flow from the detector read-out units to the permanent mass storage. Once the detectors receive the trigger signals and the associated information from the CTP, the data produced in the detectors are injected into the Detector Data Links (DDLs). DDLs use high-speed and small latency optical fibers and can transmit data with a sustained bandwidth of 200 MB/s. These DDLs are interfaced with the Front-End Read-Out (FERO) electronics of the detectors. On the read-out side of the DAQ, the Local Data Concentrators (LDCs) then collect data from the DDLs. These sub-events (event fragments) from the LDCs are then transferred to a farm of machines known as the Global Data Collectors (GDCs), where the entire events are built from all the sub-events pertaining to the same trigger. Once the event building is successful, the GDCs transfer the events to the Transient Data Storage (TDS) before migrating them to the Permanent Data Storage (PDS) [53, 62, 63].

2.4 Summary

In summary, the working of the LHC machine and the ALICE detector are discussed briefly. Special attention is given to the ITS, V0, and the muon spectrometer as they hold significant importance for the data acquired for the analysis addressed in this thesis. In general, for this analysis, the ITS is used to provide information on primary vertex and tracklet distribution, V0 is used for the trigger and multiplicity estimation, and finally, the muon spectrometer is used for the measurement of muons for the reconstruction of charmonia. The ALICE trigger and data acquisition system are also covered.

Chapter 3

Event shape dependence of J/ψ production in pp collisions at $\sqrt{s} = 13$ TeV

3.1 Motivation

In particle physics, quarkonium refers to the bound state of a pair of heavy-quark and anti-quark, mainly charmonium ($c\bar{c}$) and bottomonium ($b\bar{b}$)[1]. Heavy quarks are excellent probes for studying the properties of quark-gluon plasma (QGP) as they are produced from the initial hard partonic interactions in the early stages of the collision; thus, they interact with the medium throughout its evolution. In proton+proton (pp) collisions, the production of heavy quarks serves as a baseline measurement and is explained by QCD-based production models. The initial creation of the charm pairs is described by perturbative-QCD (pQCD), whereas the evolution to a bound state is based on non-pQCD processes. Therefore, studies related to quarkonia ($Q\bar{Q}$) can help us probe both perturbative and non-perturbative regimes of QCD. Again, just like the hydrogen

[1] *Top* quarks are relatively much heavier, so they decay quickly before an –onium ($t\bar{t}$) forms.

atom, which is a proton-electron bound state governed by electrostatic Coulomb force, the interaction between the heavy-quark-antiquark pair in charmonium and bottomonium is governed by the strong interaction. Therefore, just like hydrogen atoms, charmonium and bottomonium are expected to contain a spectrum of resonances corresponding to various excited states of the $c\bar{c}$ and $b\bar{b}$ bound state.

Traditionally, the formation of QGP is not anticipated in small collision systems such as pp collisions. Thus, studies made in pp collisions provide baseline measurements in the absence of any medium effects. However, some of the recent measurements of heavy-ion-like behavior in high-multiplicity pp collisions at the LHC have drawn the attention of the heavy-ion physics community. Mainly, the appearance of strangeness enhancement [23, 24] and ridge-like structures [43] add to these speculations. These signatures are considered as unique features of QGP and are already observed in heavy-ion collisions. Additionally, some theoretical calculations also suggest that small collision systems producing a final-state charged particle multiplicity of $dN_{\rm ch}/d\eta \gtrsim 10^2$ can survive long enough to achieve an approximate chemical equilibrium [64]. This further explains the degree of strangeness enhancement observed experimentally in small collision systems. Increased production of strange hadrons can only be explained via the formation of a strongly interacting medium [27], which is at local thermal and chemical equilibrium. Thus, to investigate the origin of strangeness enhancement in small collision systems, events are usually characterized based on the average charged-particle multiplicity, $\langle dN_{\rm ch}/d\eta\rangle$ [23, 24], although the final-state multiplicity is an outcome of the effective energy of the collision. The saturation of strangeness enhancement after a certain $\langle dN_{\rm ch}/d\eta\rangle$ indicates that it is independent of the collision system and center-of-mass energy of collision [23, 24]. To further narrow down the origin of strangeness enhancement in small collision systems, studies have focused only on high-multiplicity events with topological event selection. This is done by segregating the events dominated by one or more hard scatterings from the events dominated by multiple softer interactions. For such analysis, topological event selection based on a relatively new observable known as the transverse spherocity has been recently implemented at the LHC [45–48, 65–68].

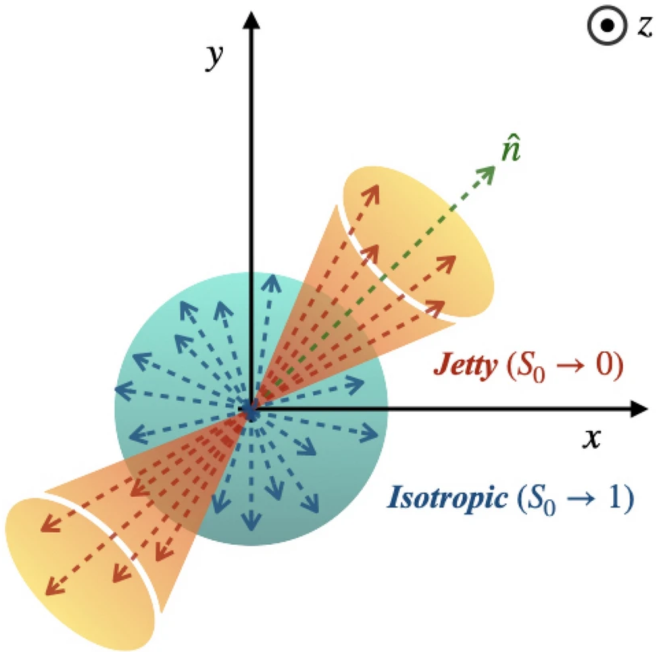

Figure 3.1: Pictorial representation of particle production in jetty and isotropic events in single pp collision on the transverse plane [69].

Transverse spherocity, being an event shape observable, can decouple the jet-dominated events from the events with spherical soft emission of particles. The first kind of event is called the jetty type, and the latter is called the isotropic type. Jetty events result from enhanced contributions of pQCD processes with hard partonic scatterings, leading to the appearance of final-state back-to-back jet structures. In contrast, events with several soft QCD processes lead to the appearance of an isotropic particle distribution at the final state. Figure 3.1 shows the azimuthal topology of the two extreme event types in a single pp collision. By construction, transverse spherocity depends on the azimuthal distribution of particles, and it is co-linear and infrared safe [66]. Transverse spherocity (S_0) is defined as follows,

$$S_0^{(p_{\rm T}=1)} = \frac{\pi^2}{4} \min_{\hat{n}} \left(\frac{\sum_{i=1}^{N_{\rm trks}} |\hat{p}_{{\rm T},i}|_{p_{\rm T}=1} \times \hat{n}}{N_{\rm trks}} \right)^2. \tag{3.1}$$

Here, $\hat{n}$ is a unit vector chosen such that the term inside the bracket is minimized. Sometimes it is also referred to as the spherocity axis. The index, "i", runs over all the tracks in an event. In general, it is found that the $\hat{n}$ unit vector aligns with one of the particle's momentum vectors [70, 71]. The normalization constant $\pi^2/4$ ensures that $S_0 \in [0, 1]$. For the jetty events, $S_0 \to 0$, and for the isotropic events, $S_0 \to 1$. Isotropic events are dominated by Underlying Event (UE) features such as multi-parton interaction (MPI). It has been hypothesized that in high-multiplicity pp collisions, heavy-ion-like effects such as strangeness enhancement and radial flow are manifested in the isotropic events, which are mostly UE dominated [45, 46]. Thus, transverse spherocity can not only separate events based on azimuthal topology but also control heavy-ion-like effects in high-multiplicity pp collisions.

One of the recent measurements in high-multiplicity pp collisions at $\sqrt{s}$ = 13 TeV with ALICE emphasizes the usage of transverse spherocity-based event selection to look for the enhanced production of strange and multi-strange hadrons [72]. By studying the production of strange hadrons in the two extreme event types using transverse spherocity, it is found that the production rates of strange particles are slightly higher for soft isotropic events and highly suppressed in hard jetty events [72]. Further, to explain these aspects of strange hadron production in pp collisions, pQCD-based models such as PYTHIA have incorporated additional phenomenological final-state pre-hadronization mechanisms, such as string percolation, color ropes, and color reconnection [73–76]. A similar study of strange hadron production with topological event selection can also be performed for the case of charm hadrons. Due to their higher mass, charm quarks are produced mainly in the initial hard partonic interactions, while a small fraction of charm quarks can also be produced at a later stage from the weak decays of beauty hadrons. The first kind is known as prompt production, while the latter is called nonprompt production. Therefore, studies involving charm hadrons with different topological event selections can help us understand its production mechanism and constrain various phenomenological models.

With this motivation, this analysis measures the p_{T}-differential yield of inclusive J/ψ as a function of transverse spherocity in high-multiplicity pp collisions at $\sqrt{s}$ = 13 TeV with ALICE. For this analysis, the reconstruction of J/ψ is performed through the electromagnetic decay channel, $J/\psi \rightarrow \mu^{+}\mu^{-}$, B.R. = $(5.961 \pm 0.033)\%$ in forward rapidity, $2.5 < y < 4.0$, using the forward muon spectrometer. For the estimation of transverse spherocity, midrapidity tracklets ($|\eta| < 0.8$) are reconstructed using the Silicon Pixel Detector (SPD), which is the innermost central barrel detector in ALICE. The V0 scintillator detectors with a pseudorapidity coverage of $2.8 < \eta < 5.1$ (V0A) and $-3.7 < \eta < -1.7$ (V0C) have been used for the estimation of event multiplicity. This analysis uses the Run 2 data collected with ALICE during 2016. We report the detailed analysis methodology, including the estimation of spherocity, dimuon invariant mass distribution, signal extraction, evaluation of systematic uncertainty, and the p_{T}-differential yield of J/ψ in different event classes. Some limitations and challenges arising in the measurement of spherocity in this analysis from the Run 2 configuration have also been reported.

3.2 Analysis details

3.2.1 Dataset selection

For this analysis, the data collected in the Run 2 data-taking period with ALICE during 2016 are used. The rootfiles `"pass1/AOD*/AliAOD.root"` for the run periods `LHC16h, LHC16j, LHC16k, LHC16o, LHC16p` are analysed. Since this analysis uses central barrel detectors such as the SPD and V0, and the forward muon spectrometer, good run numbers are obtained following the data preparation group (DPG) tags for these detectors considering the muon quality and physics selection status to be “Good” from the Run Condition Table. The final list of run numbers used in this analysis is provided in Appendix 3.6.1.

3.2.2 Event cuts

For this analysis, events are selected with at least one pair of opposite sign muons, both satisfying the low-p_{T} threshold and triggered in the muon spectrometer acceptance. This trigger is called `CMUL7-B-NOPF-MUFAST` and details of this is already given in Section 2.3. This is associated with the physics selection criteria `kMuonUnlikeLowPt7`. The selected events are further passed through various event selection cuts using the task `AddTaskPhysicsSelection (kFALSE,kTRUE,0,kFALSE)`. The first tag in the argument refers to data (`kFALSE`) or MC (`kTRUE`), and the second argument refers to the option for removing the pile-up events; hence, it is kept `kTRUE`. The primary vertex is obtained from the SPD using the `AliVEvent::GetPrimaryVertexSPD()` method, and additional vertex selection cuts are imposed on the events. These are as follows.

- Events are required to have a reconstructed SPD vertex
- The reconstructed SPD vertex should have at least one primary vertex contributor
- The primary vertex z-position, $|v_{\mathrm{z}}^{\mathrm{SPD}}|$ is required to be within $|v_{\mathrm{z}}^{\mathrm{SPD}}| <$ 10.0 cm
- The SPD vertex resolution, $\sigma_{\mathrm{z}}^{\mathrm{SPD}} < 0.25$ cm

3.2.3 Track cuts

After the event selection, standard cuts are applied on the opposite sign dimuons and single muon tracks. These are listed below.

- The radial transverse position cuts (R_{abs}) for the muon tracks for the front absorber, $17.6 < R_{\text{abs}} < 89.5$ cm to remove tracks crossing through the thicker part of the absorber

- The single muon rapidity cut in the dimuon, $-4.0 < \eta_{\mu} < -2.5$, related to spectrometer acceptance

- The dimuon rapidity cut, $-4.0 < y_{\mu\mu} < -2.5$, related to the spectrometer acceptance

- Both the muon tracks should match the low p_{T} trigger that defines the CMUL conditions (muon pairs with opposite sign)

3.2.4 Multiplicity selection

This analysis is performed with high-multiplicity pp events. For the multiplicity estimation, signals from the two V0 scintillator detectors are used, which cover the forward rapidity, $2.8 < \eta < 5.1$ and $-3.7 < \eta < -1.7$. The charge deposition in the detectors is referred to as the V0M amplitude, and events are distributed in different multiplicity percentile bins based on their V0M amplitudes. The multiplicity estimation is performed using the task `AliMultSelection::GetMultiplicityPercentile("V0M")`, which has to run before the main analysis task to give an estimate of the V0M multiplicity percentile. In this analysis, the measurement of the inclusive J/ψ yield has been performed only in the highest 10% V0 multiplicity class, *i.e.*, $(0-10)\%$ V0M.

3.2.5 Estimation of spherocity

The definition of transverse spherocity is given in Eq. 3.1. This new p_{T}-unweighted definition is chosen for two reasons. Firstly, previous studies on light-flavour particle production as a function of transverse spherocity have shown that this new p_{T}-unweighted definition helps in reducing the experimental bias introduced for the neutral particles that previously appeared while using the conventional definition of transverse spherocity [77]. Secondly, as the current analysis uses the forward rapidity reconstruction of J/ψ using the muon spectrometer, the dimuon-triggered events do not include the full central barrel charged particle track information, which is a Run 2 limitation. Instead, only the information on midrapidity tracklets is available from the SPD. As the SPD is used for tracking and vertex finding, it does not provide the transverse momenta (p_{T}) for the tracklets. However, the azimuthal angle (ϕ) and rapidity (η) of the tracklets are available. Therefore, it becomes important to use this new p_{T}-unweighted definition of transverse spherocity for this analysis. For the sake of simplicity, transverse spherocity is called spherocity for the rest of the texts in this chapter.

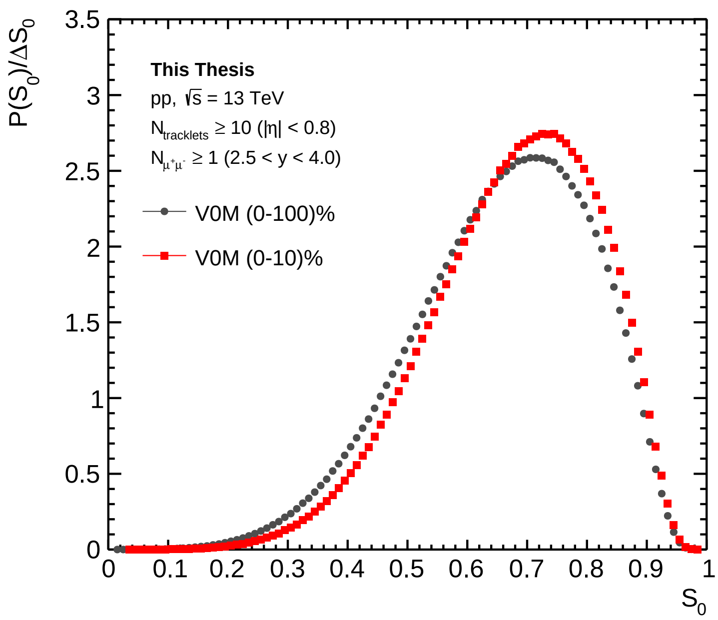

Figure 3.2: Normalized spherocity distribution measured with SPD tracklets in dimuon triggered events for V0M $(0-100)\%$ (black) and $(0-10)\%$ (red) multiplicity classes in pp collisions at $\sqrt{s} = 13$ TeV.

Figure 3.2 shows the normalized spherocity distribution measured with SPD tracklets in opposite sign dimuon triggered events for V0M $(0-100)\%$ (black) and $(0-10)\%$ (red) multiplicity classes in pp collisions at $\sqrt{s} = 13$ TeV. Spherocity is estimated with charged tracklets detected in the SPD at midrapidity. The tracks are selected in the full azimuthal coverage, $\phi \in [0, 2\pi]$, and the events with $N_{\text{tracklets}} \geq 10$ ($|\eta| < 0.8$) are selected to make a more meaningful case for the use of event classifiers. The lowest and highest 25% events in the spherocity distribution are tagged as the jetty and isotropic events, respectively. Events without any spherocity selection are called the S_0-integrated events. By comparing the two spherocity distributions in Fig. 3.2, it is clear that for the highest multiplicity class, which is V0M $(0-10)\%$, the spherocity distribution shifts towards the isotropic limit ($S_0 \to 1$). This is an essential feature of spherocity since high-

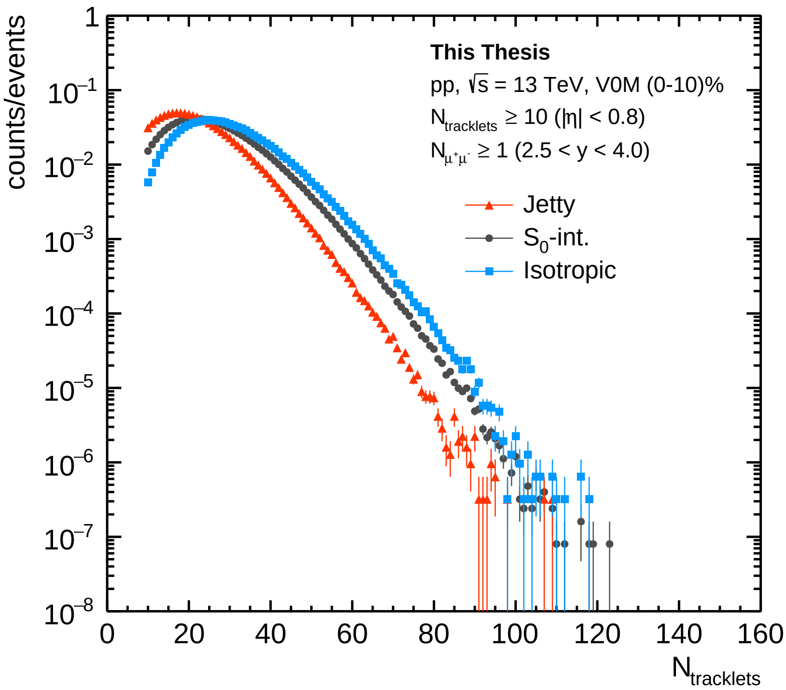

Figure 3.3: SPD tracklets distribution in jetty (red), S_0-int. (black), and isotropic (blue) events in pp collisions at $\sqrt{s} = 13$ TeV in V0M $(0-10)\%$ centrality class.

multiplicity events tend to produce more soft particles than producing fewer hard particles. Increased production of softer particles is a consequence of the UE features and is modeled through MPI-based production dynamics, which increases the yield of low-p_{T} particles. This isotropization in high-multiplicity events leads to the shift of spherocity distribution towards one. The cuts on the spherocity distribution for the selection of jetty and isotropic events are mentioned in Tab. 3.1.

Table 3.1: The lowest (jetty) and highest (isotropic) 25% cuts on the spherocity distribution in pp collisions at $\sqrt{s}$ = 13 TeV with opposite sign dimuon trigger.

V0M	**Jetty**	**Isotropic**
(0–10)%	0.0–0.58645	0.78465–1.0

Figure 3.3 shows the SPD tracklets distribution in jetty (red), S_0-int. (black), and isotropic (blue) events in pp collisions at $\sqrt{s}$ = 13 TeV in V0M $(0-10)$% centrality class. It can be seen that spherocity can successfully decouple the jetty and isotropic events from the S_0-integrated events. The jetty events seem to produce fewer particles than the isotropic events; therefore, the distribution shifts towards a higher number of tracklets by moving from jetty to isotropic type. This also ensures the spherocity selection is working. These observations also support the conclusion drawn from Fig. 3.2.

3.3 Signal extraction

In this analysis, we use the invariant mass technique to extract the inclusive J/ψ signal in the dimuon decay channel. For each of the selected opposite sign dimuons, we estimate the invariant mass, given as,

$$M_{\mu^+\mu^-} = \sqrt{(E_1 + E_2)^2 - |\vec{p_1} + \vec{p_2}|^2}. \tag{3.2}$$

Here, E_1, E_2 and $\vec{p_1}$, $\vec{p_2}$ correspond to the energy and momenta of the decay muons. $M_{\mu^+\mu^-}$ is the invariant mass of dimuon. When this dimuon invariant mass is plotted as a histogram, a signal peak should appear on the continuum around the mass of J/ψ, which is, $m_{J/\psi} = 3096.900 \pm 0.006$ MeV. Similarly, another signal peak should appear around $\psi(2S)$ mass pole which is close to J/ψ, *i.e.*, $m_{\psi(2S)} = 3686.093 \pm 0.034$ MeV. The dimuon continuum consists of the uncorrelated opposite sign dimuons mostly originating from the decay of light-flavor hadrons (π or K) or open heavy-flavor decay (c or b-hadrons). This serves as the background. The signal peak for J/ψ is much larger than that of $\psi(2S)$. This is due to the fact that $\psi(2S)$ is the resonance of J/ψ, and it has a higher probability of decaying into a J/ψ than anything else, *i.e.*, $\psi(2S) \to J/\psi + \text{anything}$, B.R. $= (59.5 \pm 0.8)\%$, which then decays to a pair of muons. All these values of mass and branching ratio are taken from the Particle Data Group [8].

From the invariant mass distribution, the raw yield of J/ψ can then be extracted. This is done by fitting the invariant mass spectrum with a sum of signal and background functions. These functions are chosen empirically, which includes multiple parts for describing the signal and the long continuum on both sides of the signal peak, which we call the *tail*. For the signal, the extended double Crystal Ball function (CB2) is used, which consists of a Gaussian core with power-law tails added on either side of the mean of the peak. Since $\psi(2S)$ mass peak is in close proximity to J/ψ, two separated CB2 functions, each for J/ψ and $\psi(2S)$, are used in the fitting. This also takes care of the fact that the high mass tail of J/ψ can be affected by the low mass tail of $\psi(2S)$. The important aspect of this fitting is that both the particles are fitted to the same type of signal function. It turns out that the parameters of the signal functions for these two particles are also closely related. For the fitting, the mass ($m_{\psi(2S)}$) and width ($\sigma_{\psi(2S)}$) of $\psi(2S)$ signal relate to the mass ($m^{\text{fit}}_{J/\psi}$) and width ($\sigma^{\text{fit}}_{J/\psi}$) of J/ψ signal obtained from the fitting as follows.

$$m_{\psi(2S)} = m_{J/\psi}^{\text{fit}} + \left(m_{\psi(2S)}^{\text{PDG}} - m_{J/\psi}^{\text{PDG}}\right) \tag{3.3}$$

$$\sigma_{\psi(2S)} = \sigma_{J/\psi}^{\text{fit}} \times \frac{\sigma_{\psi(2S)}^{\text{MC}}}{\sigma_{J/\psi}^{\text{MC}}} \tag{3.4}$$

The mass difference between the two particles is taken from the PDG [8], while the ratio of their widths is extracted from a CB2 function fitting to the Monte Carlo data, which is found to be $\sigma_{\psi(2S)}^{\text{MC}}/\sigma_{J/\psi}^{\text{MC}} \sim 1.03$, following a previous analysis based on the same data sample [78]. Two separate ad hoc functions are used for the background function. These are the Variable Width Gaussian (VWG) and Double Exponential (DoubleExp) functions. The goal is to fit the background with a minimum number of free parameters. The signal and background functions are explicitly mentioned in Appendix 3.6.2.

3.3.1 Tail parameter extraction

For the signal extraction, two combinations of the signal and background fit functions are considered. The first one is the sum of two CB2 functions for the signal and VWG for the background. Similarly, the second one is the sum of two CB2 functions for the signal and DoubleExp for the background. Additionally, two different fit ranges are considered for the fitting of the signal+background functions, which are $2.0 < M_{\mu^+\mu^-} < 5.0$ GeV/c^2 and $2.2 < M_{\mu^+\mu^-} < 4.8$ GeV/c^2. The background function is fitted first to the invariant mass spectrum excluding the signal mass region, $2.5 < M_{\mu^+\mu^-} < 4.0$ GeV/c^2 and the parameters for the background function are extracted. Then, for the signal+background fitting, the background function parameters are kept fixed. The next crucial task is to obtain the tail parameters of the signal function. Each CB2 function has four tail parameters, α_L, n_L, α_R, and n_R. There are different ways to extract the tail parameters. In this analysis, the tail parameters are obtained from data by fitting the p_{T}, y and S_0 integrated dimuon invariant mass spectrum in pp collisions at $\sqrt{s}$ = 13 TeV in V0M $(0-100)\%$ centrality class. The dimuon invariant mass spectrum is reconstructed with dimuons having $p_{\mathrm{T}} < 30.0$ GeV/c in $2.5 < y < 4.0$.

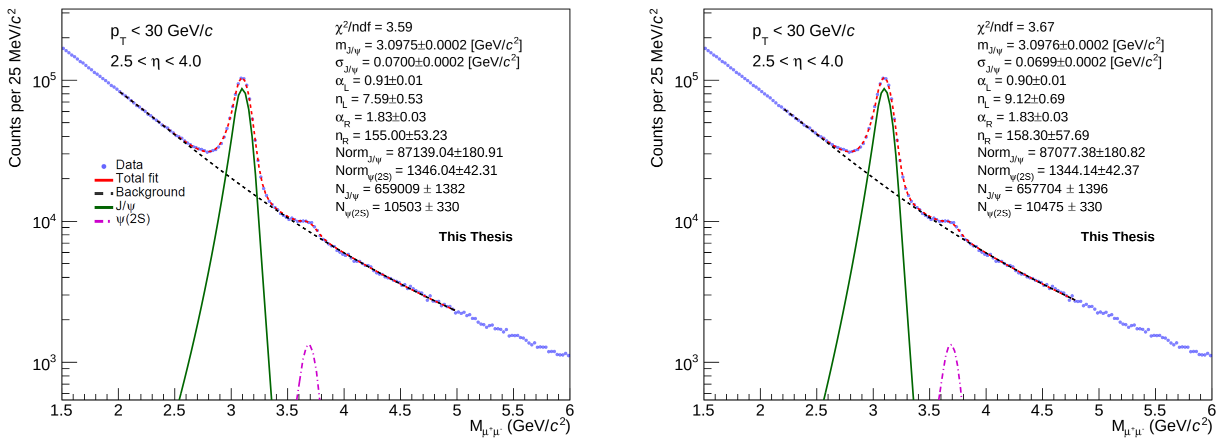

Figure 3.4: Tail parameter extraction using CB2+CB2+VWG function fitting to the p_{T}, y and S_0 integrated dimuon invariant mass spectrum in pp collisions at $\sqrt{s} = 13$ TeV in V0M $(0-100)\%$ centrality class. Fit ranges are $2.0 < M_{\mu^+\mu^-} < 5.0$ GeV/c^2 (left) and $2.2 < M_{\mu^+\mu^-} < 4.8$ GeV/c^2 (right).

Figure 3.4 shows the extraction of tail parameters for the signal function by fitting the CB2+CB2+VWG function to the p_{T}, y and S_0 integrated dimuon invariant mass spectrum in pp collisions at $\sqrt{s}$ = 13 TeV in V0M $(0-100)\%$ centrality class in the fit range of $2.0 < M_{\mu^+\mu^-} < 5.0$ GeV/c^2 (left) and $2.2 < M_{\mu^+\mu^-} < 4.8$ GeV/c^2 (right). Similarly, Fig. 3.5 represents the tail parameter extraction using the CB2+CB2+DoubleExp function. The obtained tail parameters are listed in Tab. 3.2. These tail parameters are then kept fixed for their respective fit functions and fit ranges when fitting the p_{T}-differential dimuon invariant mass spectrum for different S_0 event classes in V0M $(0-10)\%$ centrality class.

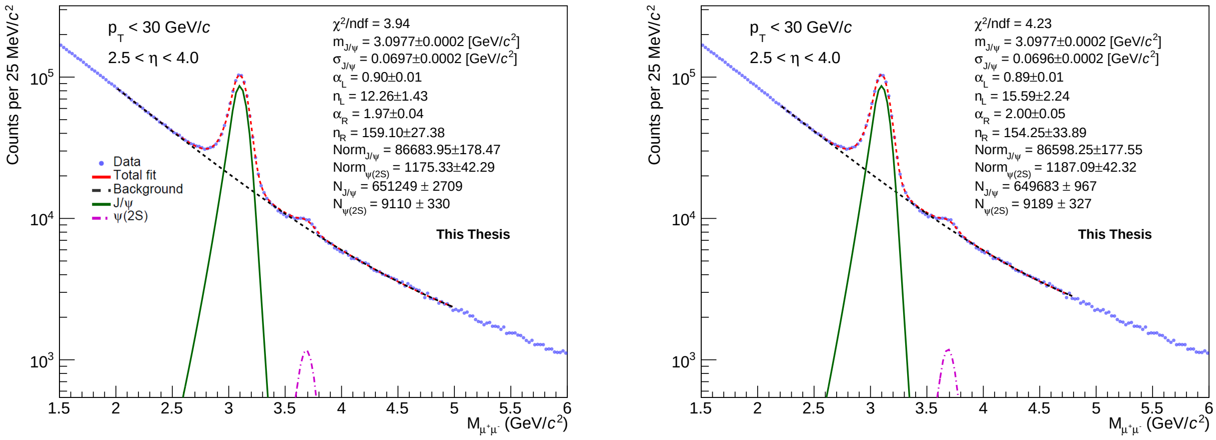

Figure 3.5: Tail parameter extraction using CB2+CB2+DoubleExp function fitting to the p_{T}, y and S_0 integrated dimuon invariant mass spectrum in pp collisions at $\sqrt{s}$ = 13 TeV in V0M $(0-100)\%$ centrality class. Fit ranges are $2.0 < M_{\mu^+\mu^-} < 5.0$ GeV/c^2 (left) and $2.2 < M_{\mu^+\mu^-} < 4.8$ GeV/c^2 (right).

Table 3.2: List of extracted tail parameters for the CB2 function.

Fit range	CB2+CB2+VWG			
	α_L	n_L	α_R	n_R
$2.0 < M_{\mu^+\mu^-} < 5.0$ GeV/c^2	0.913168	7.58798	1.82707	155.0
$2.2 < M_{\mu^+\mu^-} < 4.8$ GeV/c^2	0.903257	9.12091	1.83383	158.3

Fit range	CB2+CB2+DoubleExp			
	α_L	n_L	α_R	n_R
$2.0 < M_{\mu^+\mu^-} < 5.0$ GeV/c^2	0.899613	12.2566	1.97342	159.1
$2.2 < M_{\mu^+\mu^-} < 4.8$ GeV/c^2	0.89243	15.5921	1.99612	154.25

3.3.2 Systematic uncertainty

The p_{T}-differential yield of J/ψ is extracted from the dimuon invariant mass spectrum in seven bins of p_{T} in the range $0.0 < p_{\mathrm{T}} < 10.0$ GeV/c. Events are tagged as jetty or isotropic based on the spherocity cuts mentioned in Tab. 3.1. Only the highest multiplicity class V0M $(0-10)\%$ events are considered for this exercise. For the estimation of systematic uncertainty associated with the yield extraction, two different fit functions, and two different fit ranges are implemented making a total of four tests for each spherocity class. Thus, a total of **84** invariant mass fittings (= 7 p_{T}–bins $\times$ 2 fit functions $\times$ 2 fit ranges $\times$ 3 event classes) have been performed. From all these tests, the average yield of J/ψ ($\langle x \rangle$), the statistical ($\sigma^{\mathrm{stat.}}_{\langle x \rangle}$) and systematic uncertainty ($\sigma^{\mathrm{sys.}}_{\langle x \rangle}$) are estimated using the following expressions.

$$\langle x \rangle = \sum_{i=1}^{N_{\mathrm{tests}}} x_i \tag{3.5}$$

$$\sigma^{\mathrm{stat.}}_{\langle x \rangle} = \frac{1}{N_{\mathrm{tests}}} \sum_{i=1}^{N_{\mathrm{tests}}} \sigma_{x_i} \tag{3.6}$$

$$\sigma^{\mathrm{sys.}}_{\langle x \rangle} = \sqrt{\frac{\sum_{i=1}^{N_{\mathrm{tests}}} (x_i - \langle x \rangle)^2}{N_{\mathrm{tests}}}} \tag{3.7}$$

Here, x_i and σ_{x_i} are the yield and its statistical uncertainty for the i^{th} test. The fitting plots of the p_{T}-differential dimuon invariant mass distribution for the jetty, S_0-integrated, and isotropic event classes are presented in Appendix 3.6.3. For the fitting, standard `TMinuit` `ROOT` library is used with binned log-likelihood method, which usually works well for the binned data in counting experiments. The fitting process is terminated when the fitting parameters achieve a minimum χ^2/NDF with the status of the fitting being converged. The raw yield of J/ψ in each p_{T}–bin is then extracted by integrating the signal function over $[-3\sigma^{\mathrm{fit}}_{J/\psi}, 3\sigma^{\mathrm{fit}}_{J/\psi}]$ interval around the obtained mass pole of J/ψ from the fitting ($m^{\mathrm{fit}}_{J/\psi}$).

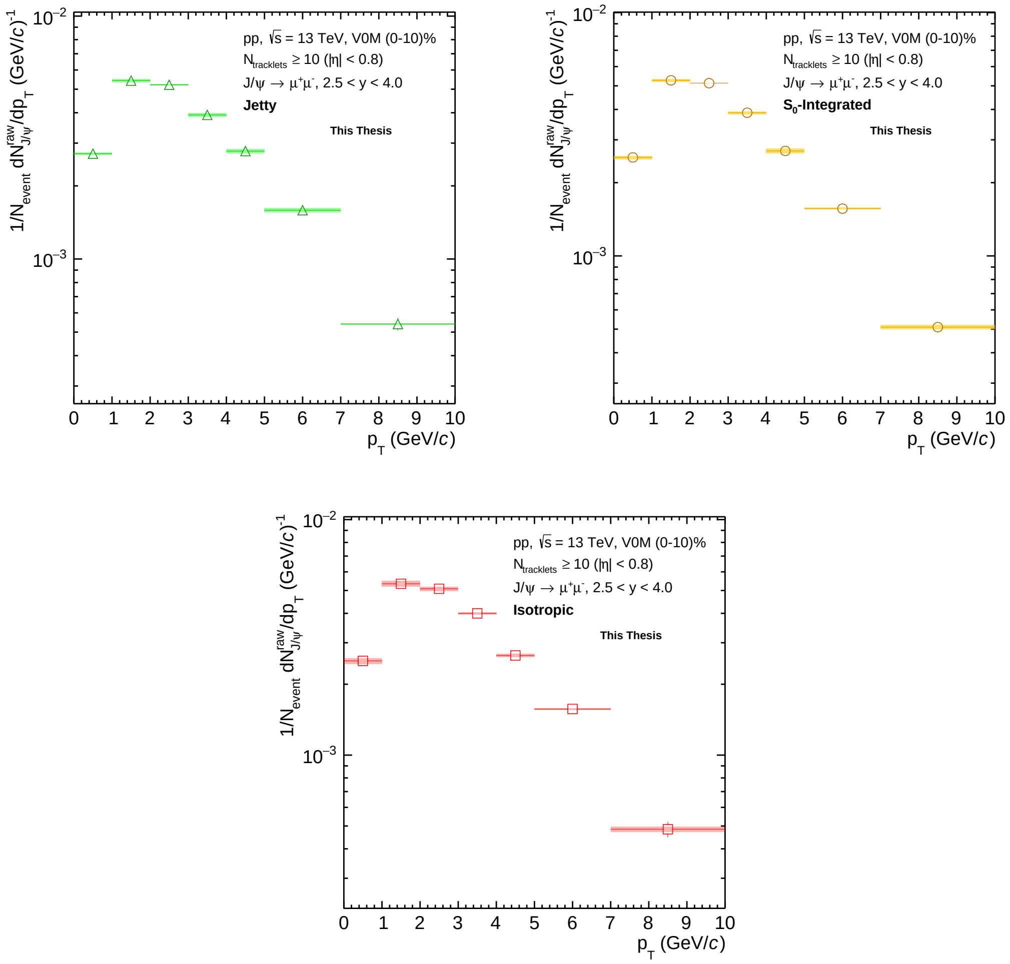

Figure 3.6: Event normalized raw p_{T} spectra of inclusive J/ψ integrated over $2.5 < y < 4.0$ for the jetty, S_0-integrated, and isotropic events in pp collisions at $\sqrt{s} = 13$ TeV in V0M $(0-10)\%$ centrality class.

3.4 Results

The p_{T}-differential yield of J/ψ with statistical and systematic uncertainty for the jetty, S_0-integrated, and isotropic event classes in pp collisions at $\sqrt{s} = 13$ TeV in V0M $(0-10)\%$ centrality class are listed in Tab. 3.3, 3.4, and 3.5, respectively. Figure 3.6 shows the event normalized raw p_{T} spectra for J/ψ integrated over $2.5 < y < 4.0$ for jetty, S_0-integrated, and isotropic events in pp collisions at at

$\sqrt{s} = 13$ TeV in V0M $(0-10)\%$ centrality class. The total number of selected events for the S_0-integrated case is 12497069. For the jetty and isotropic case, these numbers are 3122014 and 3128999, respectively. From Fig. 3.6, it is difficult to understand the contribution of jetty and isotropic events in the production of inclusive J/ψ. Therefore, the yield of J/ψ in these event classes should be compared with the S_0-integrated case. For this, it is sufficient to take the p_{T}-bin-wise yield ratio of jetty to S_0-integrated and isotropic to S_0-integrated events. The relative contributions from these two extreme types of event classes in the production of inclusive J/ψ can then be studied.

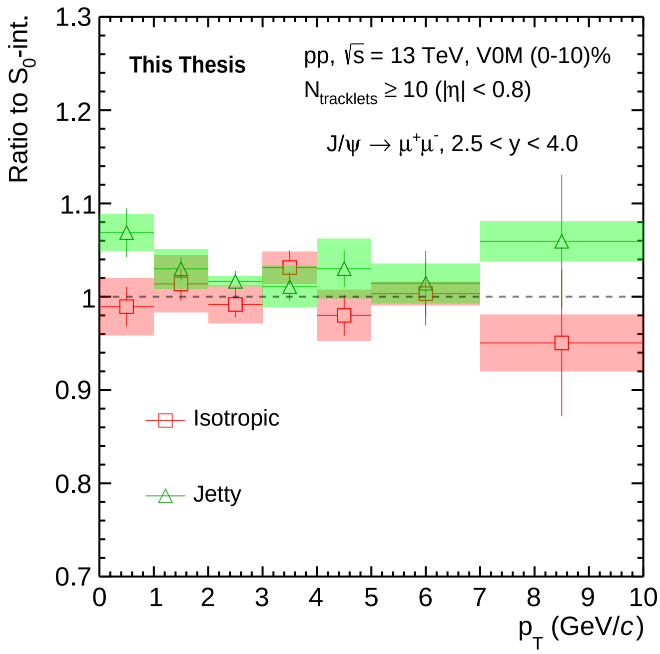

Figure 3.7: p_{T}-differential yield ratio of inclusive J/ψ in jetty to S_0-integrated events (green) and isotropic to S_0-integrated events (red), integrated over $2.5 < y < 4.0$ in pp collisions at $\sqrt{s} = 13$ TeV in V0M $(0-10)\%$ centrality class.

Figure 3.7 shows the p_{T}-differential yield ratio of inclusive J/ψ in jetty to S_0-integrated events (green) and isotropic to S_0-integrated events (red), integrated over $2.5 < y < 4.0$ in pp collisions at $\sqrt{s} = 13$ TeV in V0M $(0-10)\%$ centrality class. With the current statistics and spherocity resolution, it appears that the inclusive J/ψ production in pp collisions is enhanced in events that are jet-dominated. The jetty to S_0-integrated yield ratio is further enhanced at higher p_T. This may be due to the increased production of nonprompt J/ψ at high p_T in jetty events. Nonprompt J/ψ's are produced from flavor-changing weak decays of beauty hadrons.

On the other hand, inclusive J/ψ yield seems to have reduced in isotropic events at low and high p_T; however, a slight enhancement is observed for the intermediate p_T. This reduction in the production yield of inclusive J/ψ in isotropic events further hints towards the fact that isotropic events in high-multiplicity pp collisions show heavy-ion-like effects. Due to the high-multiplicity environment, it might happen that J/ψ yield is suppressed due to color screening, as it happens in heavy-ion collisions. Isotropic events have shown signs of heavy-ion-like signatures in previous studies, such as strangeness enhancement, which is discussed in the motivation section. Thus, these results open up new questions to ponder whether there is J/ψ suppression in high-multiplicity pp collisions. Overall, the trend of inclusive yield of J/ψ appears to show a reverse trend as compared to the light-flavor hadrons and strange hadrons production in pp collisions. For a solid conclusion, increased statistics and improved spherocity resolution are both necessary for such analysis, which can be further addressed in the Run 3 data taking with ALICE at the LHC.

3.5 Limitations and challenges

In this section, we present some of the limitations and challenges regarding the estimation of spherocity using the SPD tracklets. Since, with the forward dimuon trigger, the midrapidity global charged particle tracks are not available, this analysis uses the available midrapidity SPD tracklets for the estimation of spherocity. This is clearly a Run 2 data-taking limitation. We perform a Monte Carlo (MC) closure test using the generated tracks, reconstructed global tracks, and reconstructed SPD tracklets to check the resolution and accuracy of spherocity, which is presented here. We use a data sample from the MC production `LHC17f5` anchored to the `LHC16h` run period. This is a general-purpose MC production simulated using the PYTHIA event generator for pp collisions at $\sqrt{s} = 13$ TeV.

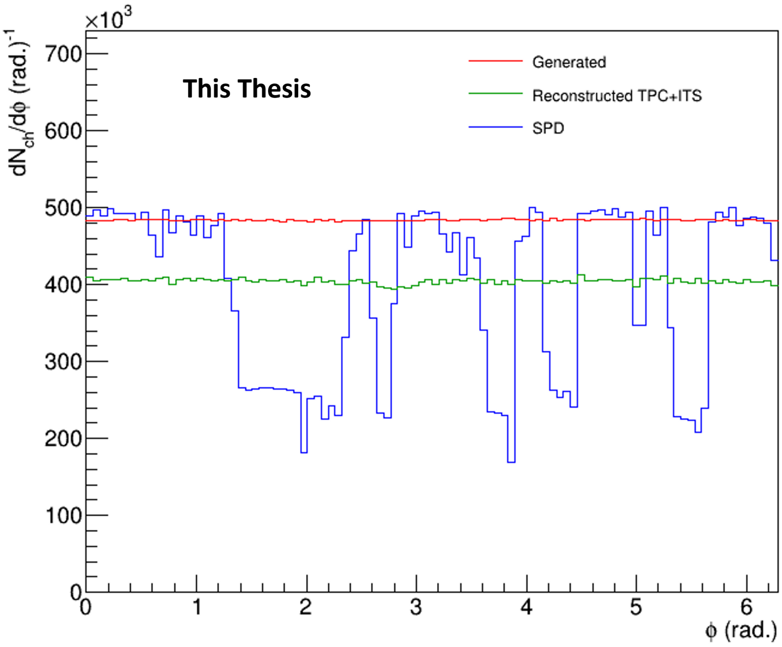

Figure 3.8: The azimuthal angle (ϕ) distribution of the generated tracks (red), reconstructed tracks with ITS+TPC matching (green), and the tracklets from the SPD (blue) for the MC production `LHC17f5` anchored to `LHC16h`.

Figure 3.8 shows the azimuthal angle (ϕ) distribution of the generated tracks, reconstructed tracks with ITS+TPC matching (global tracks), and reconstructed tracklets from the SPD. For the case of generated and reconstructed tracks with ITS+TPC matching, the obtained ϕ distributions are almost uniform (or flat). This is expected from a detector with a complete azimuthal acceptance. However, for the case of SPD tracklets, the obtained ϕ distribution is not uniform. This is clearly due to the nonuniform azimuthal acceptance of the SPD. During the data-taking operations, some of the inner and outer staves of the SPD were not operating optimally, which affected the measured azimuthal distribution of the tracklets. For the estimation of spherocity, we need the full azimuthal coverage, *i.e.*, $\phi \in [0, 2\pi]$. Thus, the nonuniform acceptance of SPD affects the spherocity distribution. Therefore, it becomes necessary to check the effects of this nonuniform acceptance on the estimation of spherocity and, thus, the performance of the event selection based on azimuthal topology, which is the primary goal of this analysis.

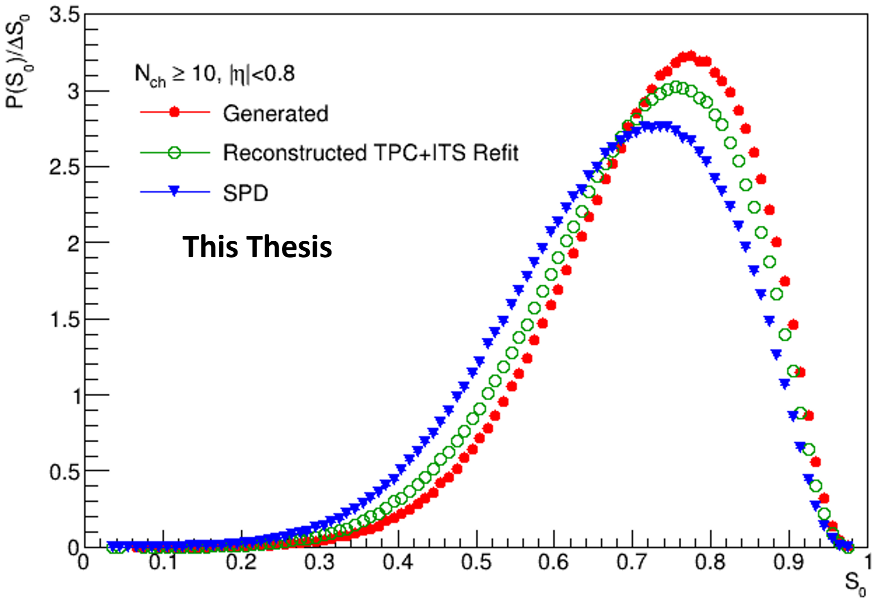

Figure 3.9: The spherocity distribution obtained using the generated (red), reconstructed tracks with ITS+TPS refit (green), and the SPD tracklets (blue) with $N_{\rm ch} \geq 10$ in $|\eta| < 0.8$ for the V0M $(0-10\%)$ multiplicity class.

Figure 3.9 shows the spherocity distribution obtained using the generated tracks, reconstructed tracks with ITS+TPS refit, and reconstructed SPD tracklets with $N_{\rm ch} \geq 10$ in $|\eta| < 0.8$ for the V0M $(0-10\%)$ multiplicity class. It is observed that due to various detector effects and acceptance, the entire S_0 distribution estimated using the reconstructed ITS+TPC tracks shifts slightly to the left

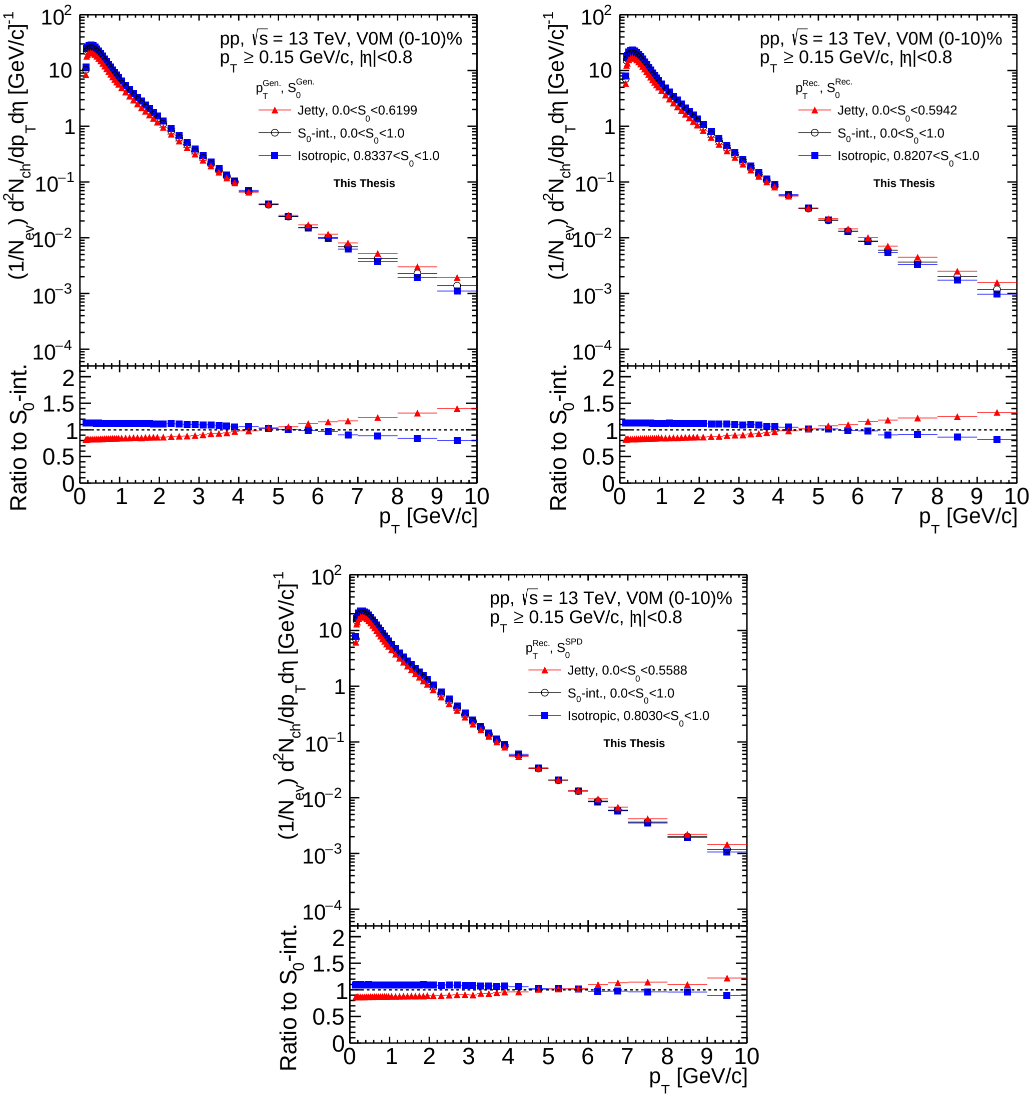

Figure 3.10: Transverse momentum (p_{T}) spectra of the global charged particles for jetty (red), S_0-integrated (black), and isotropic (blue) events for the generated, reconstructed with ITS+TPC refit, and SPD are shown. The bottom panels show the ratio of jetty and isotropic spectra to the respective S_0-integrated spectra.

side as compared to the generated spherocity (true) distribution. However, this effect seems to be significant for the S_0 distribution obtained using the SPD tracklets. This deviation of the reconstructed spherocity distribution from the true distribution can be attributed to the limited azimuthal acceptance of the

SPD. Now, we would like to evaluate its effect on the event selection. To do so, it will be wise to look into the transverse momentum spectra of global charged particles in midrapidity in different event classes. The event selection will be based on these three spherocity distributions independently.

Figure 3.10 shows the $p_{\rm T}$ spectra of the global charged particles in midrapidity for the jetty (red), S_0-integrated (black), and isotropic (blue) events in simulated pp collisions at $\sqrt{s}$ = 13 TeV in V0M $(0-10)\%$ centrality class. The event selection is done using the spherocity distributions obtained from the generated tracks, reconstructed global tracks, and SPD tracklets. The bottom panels show the ratio of $p_{\rm T}$ spectra of the jetty and isotropic events to their respective S_0-integrated events. Corresponding S_0 selection cuts are also mentioned in the legends. For the case of generated and reconstructed global tracks presented in the upper two plots, the event selection gives a meaningful result. This can be observed by looking into their bottom ratio plots, where the isotropic events have a clear dominance over jetty events at low $p_{\rm T}$; however, at high-$p_{\rm T}$, the trend reverses with jetty events taking over isotropic events. This trend is prominently visible for the top two plots, which use the spherocity estimated with generated and reconstructed global tracks as spherocity can successfully disentangle both event types. However, this is slightly different for the case of spherocity estimated using the SPD tracklets. As it can be seen, at low-$p_{\rm T}$, the trend of isotropic events dominating over jetty events is still visible, but at high-$p_{\rm T}$, the distinction between jetty and isotropic events is not as clear as the other two cases. This shape of the $p_{\rm T}$ spectra for the isotropic events does not seem to change much, but for the case of jetty events, the shape of the $p_{\rm T}$ spectra seems to have changed. This effect seems to be $p_{\rm T}$ dependent as at high-$p_{\rm T}$ this difference of much clear. Now, to understand the effects induced by this event selection, one can take the ratio of reconstructed to generated $p_{\rm T}$ spectra. If there is no bias in the estimation of spherocity, the ratio of reconstructed to generated $p_{\rm T}$ spectra should be close to unity. Any deviation from unity would reflect an estimation bias in the spherocity.

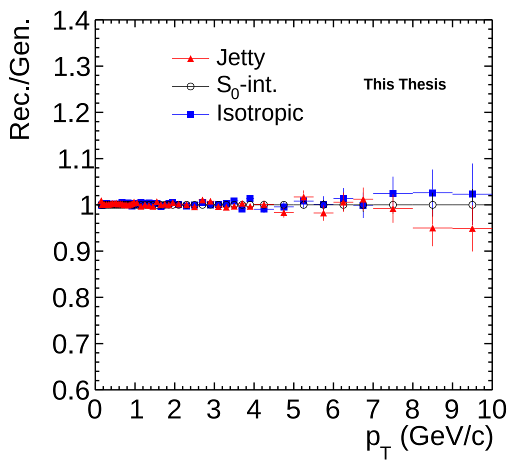

Figure 3.11: Ratio of reconstructed to generated p_{T} spectra for jetty (red), S_0-integrated (black), and isotropic (blue) events. The event selection is performed based on the estimated S_0 using the reconstructed ITS+TPC tracks and SPD tracklets, on the left and right plots, respectively.

Figure 3.11 shows the ratio of reconstructed to generated p_{T} spectra for jetty (red), S_0-integrated (black), and isotropic (blue) events. For the reconstructed spectra case, there are two choices of event selection, one from the global ITS+TPC tracks and one with the SPD. The event selection is performed based on the estimated S_0 using the reconstructed ITS+TPC tracks and SPD tracklets, on the left and right plots, respectively. From the first instance, it is evident that the left plot with the definition of S_0 using the reconstructed ITS+TPC tracks gives a flat ratio, meaning the event selection is almost identical to the generated spectra, showing no bias to the estimation of spherocity. However, the right plot shows a little variation of spectra with respect to the generated case when the event selection is applied for S_0 estimated with the SPD. The variation ranges from $(0-5)\%$ at low-p_{T} to $(10-12)\%$ at high-p_{T} for the jetty and isotropic events. This modification in the ratio is a direct consequence of the SPD nonuniform azimuthal acceptance.

Since this analysis uses the SPD tracklets for the estimation of spherocity, this estimation bias can still propagate to the results presented in this analysis. It is clearly due to the limitation of the Run 2 SPD configuration and also data-taking criteria (the dimuon trigger gives no access to the central barrel global tracks). Hence, this issue of the estimation of bias on spherocity can only be resolved in the new Run 3 pp collision data, which is being recorded now during the time of writing this thesis.

3.6 Appendix

3.6.1 List of good run numbers

LHC16h (72 Runs)

255467, 255466, 255465, 255463, 255447, 255442, 255440, 255415, 255402, 255398, 255352, 255351, 255350, 255283, 255280, 255276, 255275, 255256, 255255, 255253, 255252, 255251, 255249, 255248, 255247, 255242, 255240, 255182, 255180, 255177, 255176, 255173, 255171, 255167, 255162, 255159, 255154, 255111, 255091, 255086, 255085, 255082, 255079, 255076, 255075, 255074, 255073, 255071, 255068, 255042, 255010, 255009, 255008, 254984, 254983, 254654, 254653, 254652, 254651, 254649, 254648, 254646, 254644, 254640, 254632, 254630, 254629, 254621, 254608, 254606, 254604, 254419

LHC16j (49 Runs)

256420, 256418, 256417, 256415, 256373, 256372, 256371, 256368, 256366, 256365, 256364, 256363, 256362, 256361, 256356, 256311, 256307, 256302, 256298, 256297, 256295, 256292, 256290, 256289, 256287, 256284, 256283, 256282, 256281, 256231, 256228, 256227, 256223, 256222, 256219, 256215, 256213, 256212, 256210, 256169, 256204, 256161, 256158, 256157, 256156, 256149, 256148, 256147, 256146

LHC16k (171 Runs)

258537, 258499, 258498, 258477, 258456, 258454, 258452, 258426, 258393, 258391, 258388, 258387, 258359, 258336, 258332, 258307, 258306, 258303, 258302, 258301, 258299, 258280, 258278, 258274, 258273, 258271, 258270, 258258, 258257, 258256, 258204, 258203, 258202, 258197, 258178, 258117, 258114, 258113, 258109, 258108, 258107, 258063, 258062, 258060, 258059, 258049, 258048, 258045, 258042, 258041, 258039, 258019, 258017, 258014, 258012, 258008, 257989, 257986, 257979, 257963, 257960, 257958, 257957, 257939, 257937, 257936, 257932, 257912, 257901, 257893, 257892, 257737, 257735, 257734, 257733, 257727, 257725, 257724, 257697, 257694, 257688, 257687, 257685, 257684, 257682, 257644, 257642, 257636, 257635, 257632, 257630, 257606, 257605, 257604, 257601, 257595, 257594, 257592, 257590, 257588, 257587, 257566, 257565, 257564, 257563, 257562, 257561, 257560, 257541, 257540, 257531, 257530, 257492, 257491, 257490, 257488, 257487, 257474, 257468, 257457, 257433, 257364, 257358, 257330, 257322, 257320, 257318, 257260, 257224, 257095, 257092, 257086, 257084, 257083, 257082, 257080, 257077, 257071, 257026, 257021, 257012, 257011, 256944, 256942, 256941, 256697, 256695, 256694, 256691, 256684, 256681, 256677, 256676, 256658, 256620, 256619, 256591, 256567, 256565, 256564, 256561, 256560, 256557, 256556, 256554, 256552, 256512, 256510, 256506, 256504, 258399

LHC16o (101 Runs)

264035, 264033, 263985, 263984, 263981, 263979, 263978, 263977, 263923, 263920, 263917, 263916, 263905, 263866, 263863, 263861, 263830, 263829, 263824, 263823, 263813, 263810, 263803, 263793, 263792, 263790, 263787, 263786, 263785, 263784, 263744, 263743, 263741, 263739, 263738, 263737, 263691, 263690, 263689, 263682, 263662, 263657, 263654, 263653, 263652, 263647, 263529, 263497, 263496, 263490, 263487, 263332, 262858, 262855, 262853, 262849, 262847, 262844, 262842, 262841, 262778, 262777, 262776, 262768, 262760, 262727, 262725, 262723, 262719, 262717, 262713, 262705, 262635, 262632, 262628, 262594, 262593, 262583, 262578, 262574, 262572, 262571, 262570, 262569, 262568, 262567, 262563, 262537, 262533, 262532, 262528, 262492, 262487, 262451, 262430, 262428, 262424, 262423, 262422, 262419, 262418

LHC16p (39 Runs)

264347, 264346, 264345, 264341, 264336, 264312, 264306, 264305, 264281, 264279, 264277, 264273, 264267, 264266, 264265, 264264, 264262, 264261, 264260, 264259, 264238, 264233, 264232, 264198, 264197, 264194, 264188, 264168, 264164, 264138, 264137, 264129, 264110, 264109, 264086, 264085, 264082, 264078, 264076

3.6.2 Signal and Background fitting functions

3.6.2.1 Extended Crystal Ball (CB2)

$$f(x;\mu,\sigma,\alpha_L,n_L,\alpha_R,n_R,N) = N \times \begin{cases} \exp(-0.5v^2), & \text{if } v > -\alpha_L \ \&\ v < \alpha_R \\ A \times (B-v)^{-n_L}, & \text{if } v \leq -\alpha_L \\ C \times (D+v)^{-n_R}, & \text{if } v \geq \alpha_R \end{cases} \tag{3.8}$$

where,

$$\begin{aligned} v &= (x-\mu)/\sigma \\ A &= \left(\frac{n_L}{|\alpha_L|}\right)^{n_L} \times \exp(-0.5\alpha_L^2) \\ B &= \frac{n_L}{|\alpha_L|} - |\alpha_L| \\ C &= \left(\frac{n_R}{|\alpha_R|}\right)^{n_R} \times \exp(-0.5\alpha_R^2) \\ D &= \frac{n_R}{|\alpha_R|} - |\alpha_R| \end{aligned}$$

3.6.2.2 Variable Width Gaussian (VWG)

$$f(x;\mu,A,B,N) = N \times \left(\exp\left[-0.5 \times \left(\frac{x-\mu}{\sigma_{\text{VWG}}}\right)^2\right]\right) \tag{3.9}$$

where,

$$\sigma_{\mathrm{VWG}} = A + B \times \left(\frac{x-\mu}{\mu}\right)$$

3.6.2.3 Double Exponential (DoubleExp)

$$f(x; a, b, c, d) = \exp(a + bx) + \exp(c + dx) \tag{3.10}$$

3.6.3 p_{T}-differential yield extraction

Table 3.3: The p_{T}-differential yield of J/ψ with statistical and systematic uncertainty for the jetty events in pp collisions at $\sqrt{s}$ = 13 TeV in V0M $(0-10)\%$ centrality class.

p_{T} (GeV/c)	$\langle N_{J/\psi}\rangle \pm$ stat. $\pm$ sys.
0.0–1.0	8473.23 ± 196.942 ± 92.7005
1.0–2.0	16938.3 ± 172.404 ± 279.063
2.0–3.0	16274.6 ± 160.362 ± 86.2778
3.0–4.0	12232.5 ± 172.1 ± 221.779
4.0–5.0	8685.65 ± 139.842 ± 183.943
5.0–7.0	9909.79 ± 145.011 ± 94.996
7.0–10.0	5055.66 ± 101.006 ± 11.7813

Table 3.4: The p_{T}-differential yield of J/ψ with statistical and systematic uncertainty for the S_0-integrated events in pp collisions at $\sqrt{s}$ = 13 TeV in V0M $(0-10)\%$ centrality class.

p_{T} (GeV/c)	$\langle N_{J/\psi} \rangle \pm$ stat. $\pm$ sys.
0.0–1.0	31737.3 ± 243.989 ± 471.445
1.0–2.0	65834.3 ± 439.99 ± 812.506
2.0–3.0	64095.4 ± 318.414 ± 23.3642
3.0–4.0	48445 ± 263.508 ± 610.83
4.0–5.0	33754.1 ± 339.534 ± 762.9
5.0–7.0	39103.3 ± 349.963 ± 173.134
7.0–10.0	19103.5 ± 195.563 ± 122.292

Table 3.5: The p_{T}-differential yield of J/ψ with statistical and systematic uncertainty for the isotropic events in pp collisions at $\sqrt{s} = 13$ TeV in V0M $(0-10)\%$ centrality class.

p_{T} (GeV/c)	$\langle N_{J/\psi} \rangle \pm$ stat. $\pm$ sys.
0.0–1.0	7861.62 ± 158.116 ± 215.187
1.0–2.0	16710.3 ± 270.104 ± 462.382
2.0–3.0	15914.2 ± 207.957 ± 324.681
3.0–4.0	12508.5 ± 212.883 ± 139.741
4.0–5.0	8282.3 ± 166.597 ± 137.555
5.0–7.0	9823.04 ± 141.437 ± 45.2408
7.0–10.0	4546.13 ± 116.247 ± 38.8111

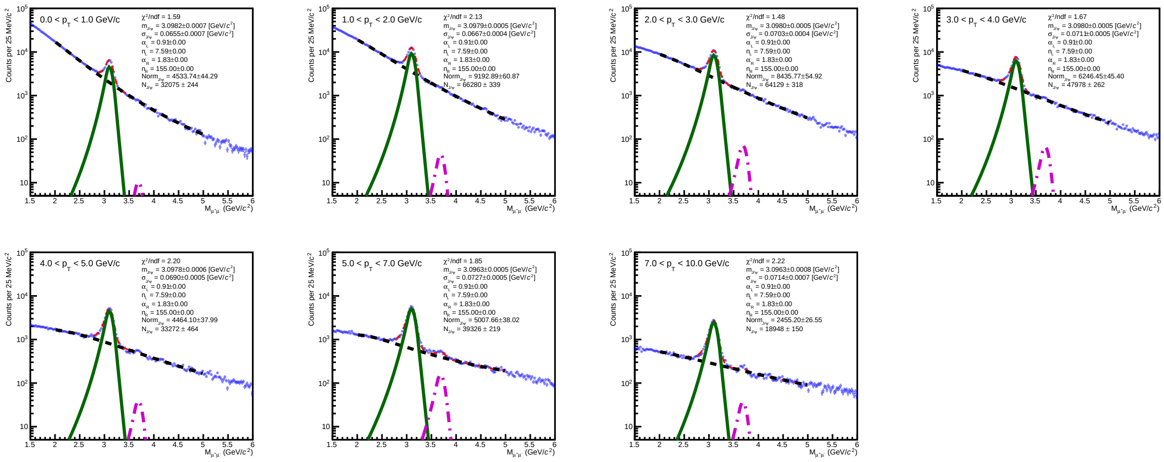

Figure 3.12: Yield extraction using CB2+CB2+VWG fit function in fit range $2.0 < M_{\mu^+\mu^-} < 5.0$ GeV/c^2 for S_0-integrated events.

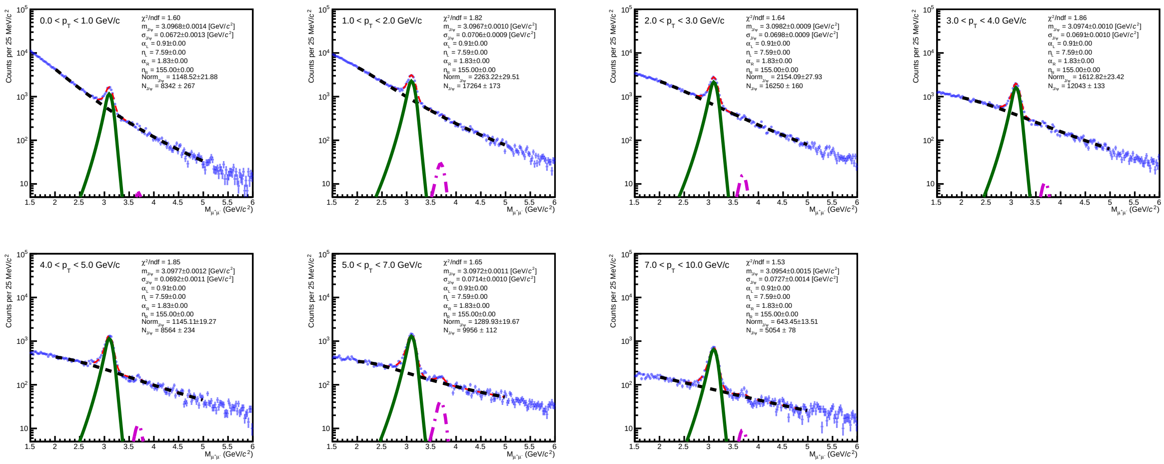

Figure 3.13: Yield extraction using CB2+CB2+VWG fit function in fit range $2.0 < M_{\mu^+\mu^-} < 5.0$ GeV/c^2 for jetty events.

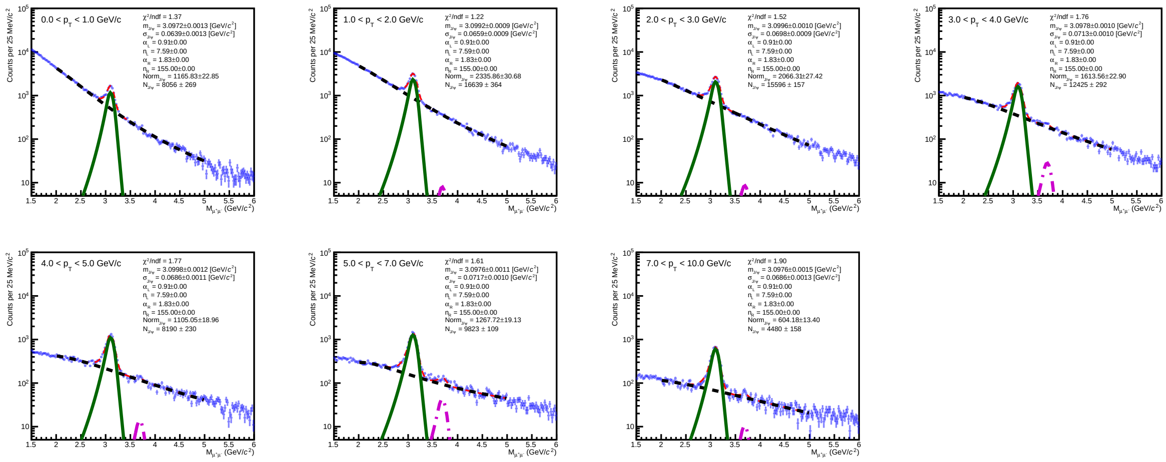

Figure 3.14: Yield extraction using CB2+CB2+VWG fit function in fit range $2.0 < M_{\mu^+\mu^-} < 5.0$ GeV/c^2 for isotropic events.

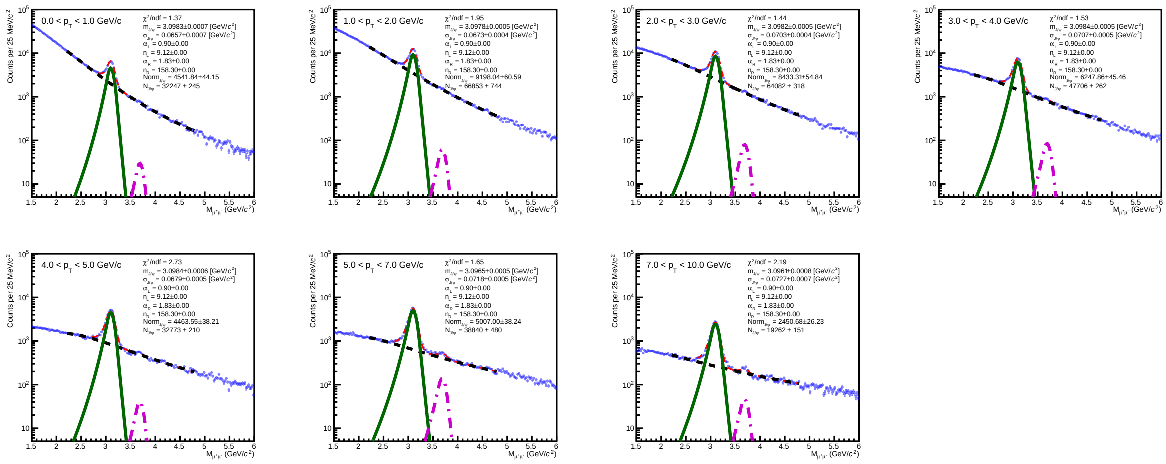

Figure 3.15: Yield extraction using CB2+CB2+VWG fit function in fit range $2.2 < M_{\mu^+\mu^-} < 4.8$ GeV/c^2 for S_0-integrated events.

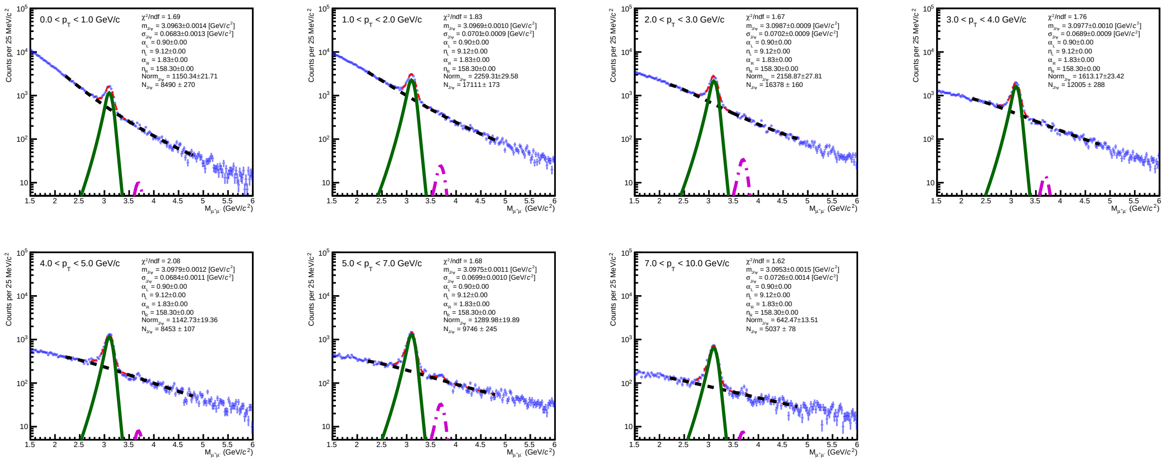

Figure 3.16: Yield extraction using CB2+CB2+VWG fit function in fit range $2.2 < M_{\mu^+\mu^-} < 4.8$ GeV/c^2 for jetty events.

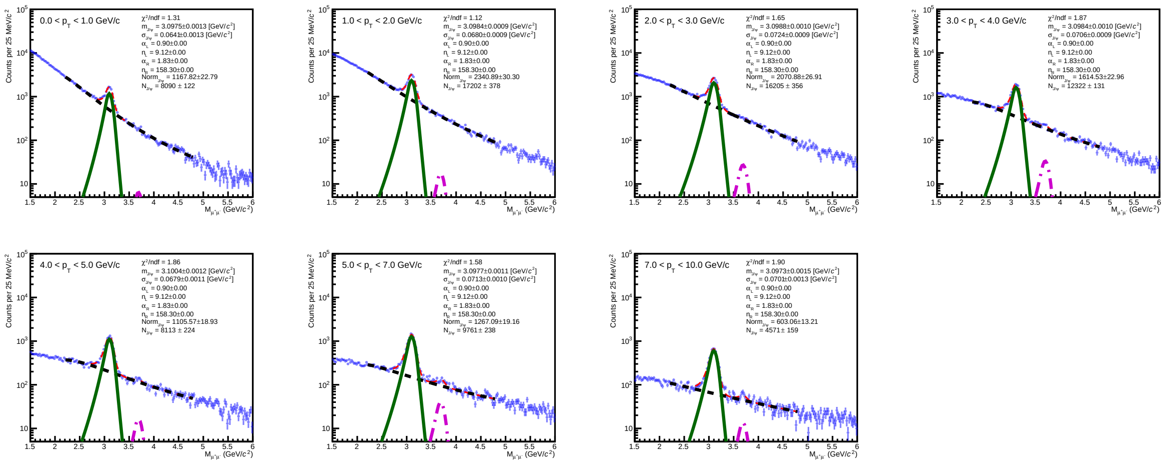

Figure 3.17: Yield extraction using CB2+CB2+VWG fit function in fit range $2.2 < M_{\mu^+\mu^-} < 4.8$ GeV/c^2 for isotropic events.

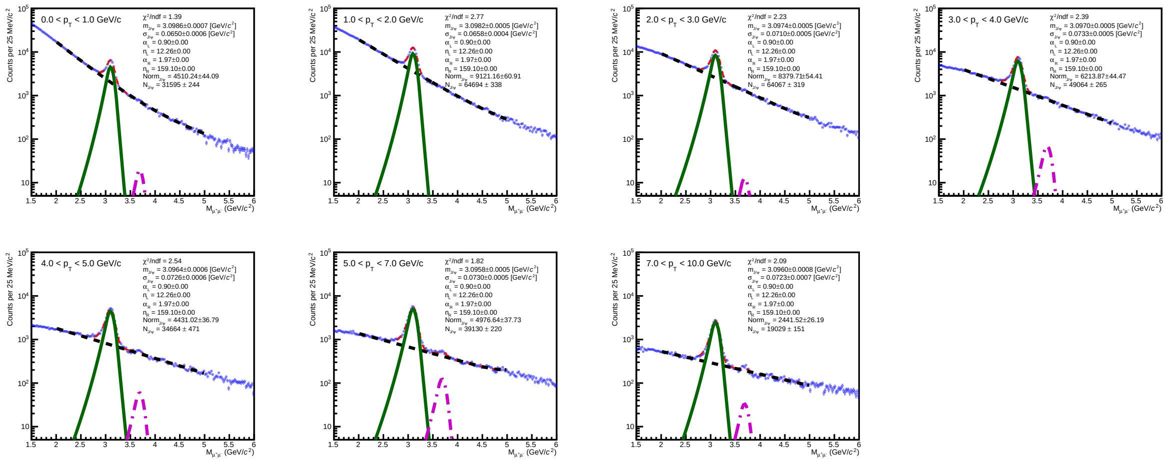

Figure 3.18: Yield extraction using CB2+CB2+DoubleExp fit function in fit range $2.0 < M_{\mu^+\mu^-} < 5.0$ GeV/c^2 for S_0-integrated events.

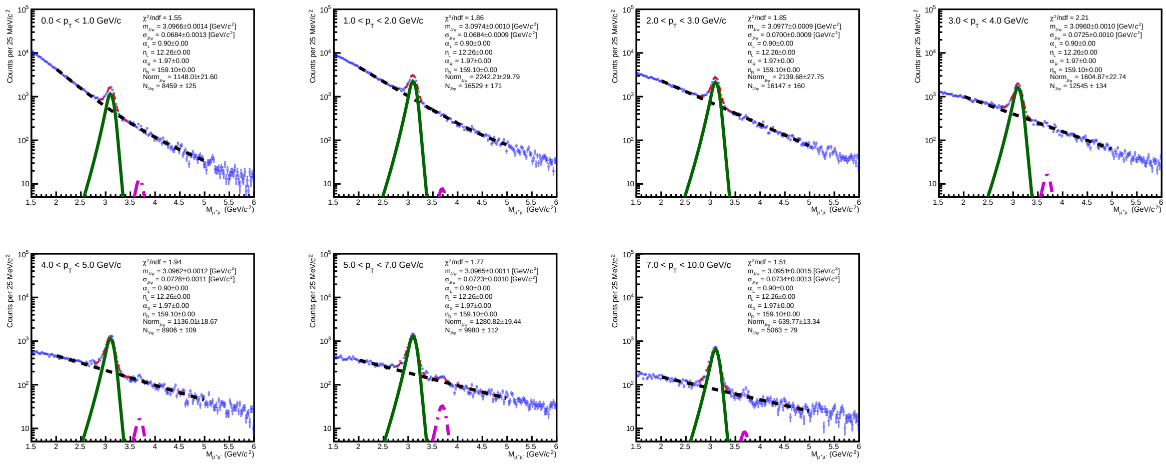

Figure 3.19: Yield extraction using CB2+CB2+DoubleExp fit function in fit range $2.0 < M_{\mu^+\mu^-} < 5.0$ GeV/c^2 for jetty events.

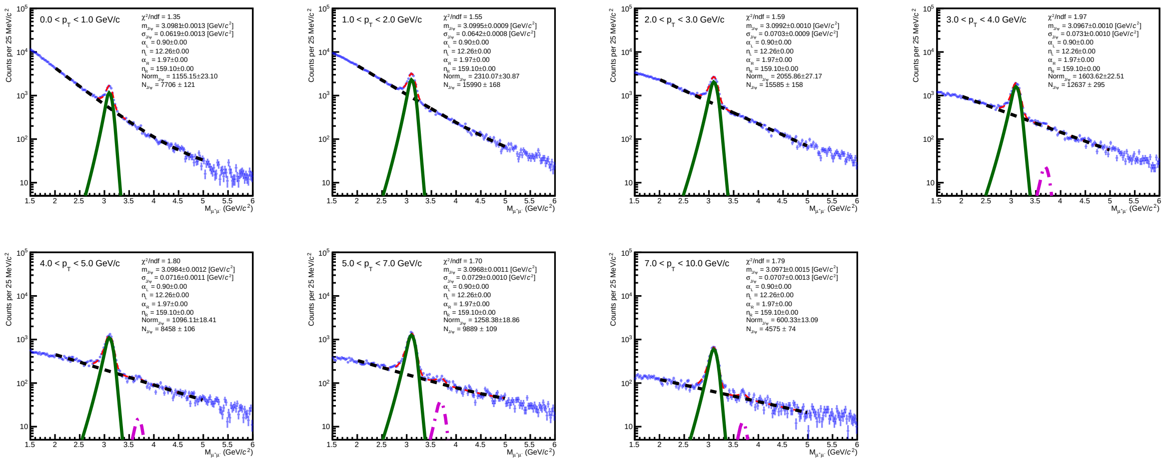

Figure 3.20: Yield extraction using CB2+CB2+DoubleExp fit function in fit range $2.0 < M_{\mu^+\mu^-} < 5.0$ GeV/c^2 for isotropic events.

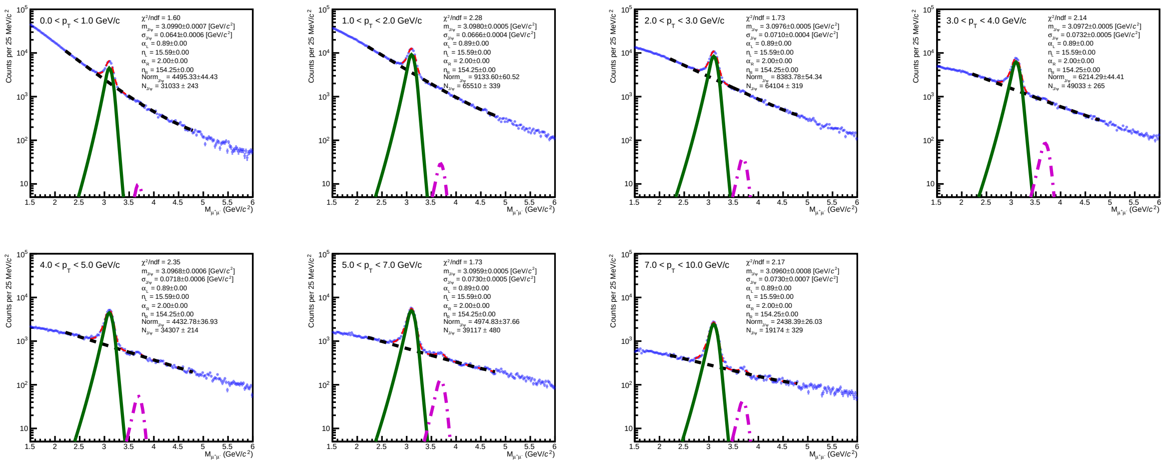

Figure 3.21: Yield extraction using CB2+CB2+DoubleExp fit function in fit range $2.2 < M_{\mu^+\mu^-} < 4.8$ GeV/c^2 for S_0-integrated events.

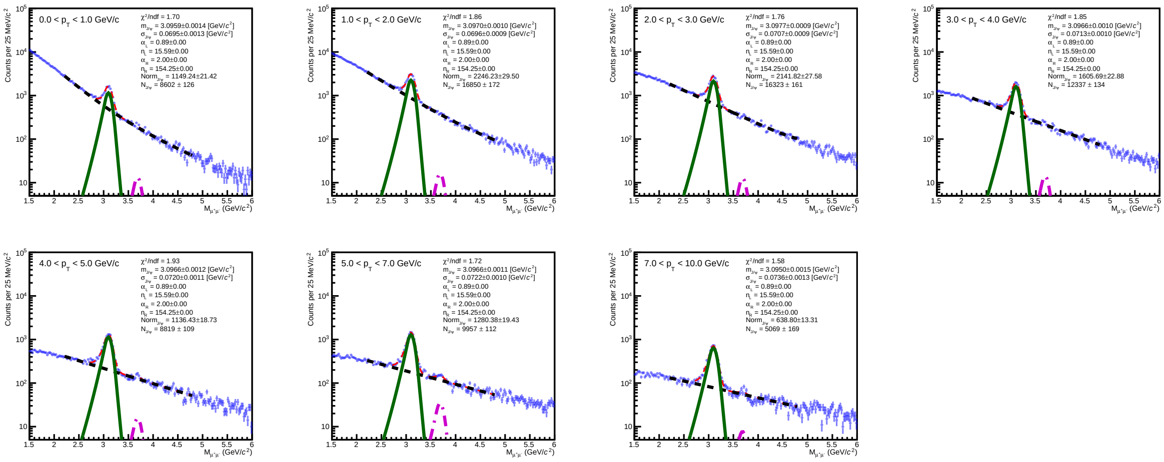

Figure 3.22: Yield extraction using CB2+CB2+DoubleExp fit function in fit range $2.2 < M_{\mu^+\mu^-} < 4.8$ GeV/c^2 for jetty events.

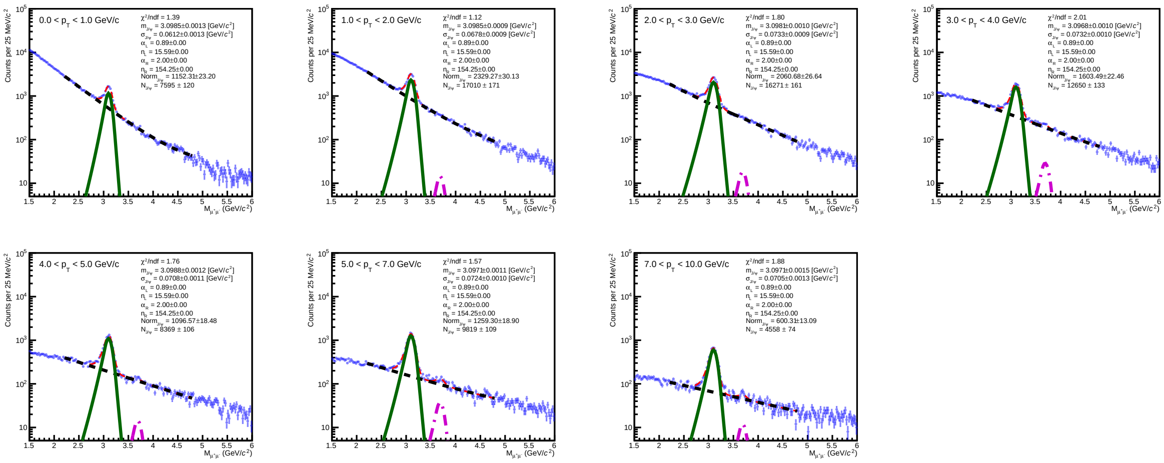

Figure 3.23: Yield extraction using CB2+CB2+DoubleExp fit function in fit range $2.2 < M_{\mu^+\mu^-} < 4.8$ GeV/c^2 for isotropic events.

Chapter 4

Study of elliptic flow as a function of transverse spherocity in heavy-ion collisions

4.1 Motivation

Studies related to heavy-ion collisions at the most powerful particle accelerators in the world, the Large Hadron Collider (LHC) at CERN, Switzerland, and Relativistic Heavy Ion Collider (RHIC) at BNL, USA, have primarily focused on the creation and properties of quark-gluon plasma (QGP), a primordial matter consisting quarks and gluons. Due to the properties of strong interaction, the medium formed in such violent and energetic collisions remains far from any direct laboratory measurements. Experimentalists only have access to the debris, the by-products of such collisions, effectively measured through various state-of-the-art detectors. Any information regarding the QGP and the theory of strong interaction can be inferred from these produced particles as signals reconstructed via detectors. While theory suggests the bare minimum requirements for the formation of QGP, experiments rely on studying several indirect signatures that strongly hint towards forming such a deconfined medium in relativistic heavy-ion collisions. The appearance of strong collective flow [29, 79], strangeness enhancement [24], jet quenching effects [30], and suppression of quarkonia [35] are the most studied QGP signatures for the past decades. These measurements have established rightfully the presence of QGP in heavy-ion collisions at RHIC and LHC energies. One of the many successes achieved in the field of heavy-ion collisions is to show that the QGP is the most perfect fluid found in nature whose specific shear viscosity (η/s) is close to the lower bound estimate of $1/4\pi$ from the AdS/CFT calculations and a temperature-dependent specific bulk viscosity ($\zeta/s(T)$) is preferred by the QGP medium [80]. This is possible by comparing the QGP medium evolution to the second-order viscous hydrodynamics simulation and extracting the transport coefficients using Bayesian parameter estimation techniques [81].

To precisely quantify the medium effects on the final state observables, one also needs a system where the production of QGP is not anticipated. Traditionally, proton+proton collisions are considered to be one such system without QGP. Thus, studies made in proton+proton collisions are treated as the baseline measurements to understand the QGP medium formation and its characterization in heavy-ion collisions [14]. In the absence of any medium, particle production in proton+proton collisions, being devoid of multi-nucleon participants, can be very different from that of heavy-ion collisions. However, some of the recent measurements of heavy-ion-like behavior in proton+proton collisions at the LHC have concerned the heavy-ion physics community. Mainly, the appearance of ridge-like structures [43] and strangeness enhancement [24] add to these speculations. To investigate these hints of possible medium formation in proton+proton collisions, a relatively new event shape classifier has been introduced at the LHC, known as the transverse spherocity (S_0) [45–48, 65–68]. This event shape observable is capable of decoupling the jet dominated events from the events with spherical soft emission of particles. The first kind is called the jetty, and the latter is called the isotropic events. Jetty events result from enhanced contributions from pQCD processes; however, the isotropic events are due to the interplay among many underlying events.

For the first time, this study implements a transverse spherocity-based event shape classifier in heavy-ion collisions, where the production of QGP medium has already been established. This study with transverse spherocity as the event shape classifier will complement the current event shape approach based on flow vectors in heavy-ion collisions [82, 83]. In this work, we report an extensive study of transverse spherocity dependence of elliptic flow of charged particles in Pb–Pb collisions at $\sqrt{s_{\rm NN}}$ = 5.02 TeV using a multiphase transport model (AMPT). The elliptic flow for identified light-flavor hadrons and their number-of-constituent-quark scaling are also investigated in different event classes using transverse spherocity at RHIC and LHC energies. This study implements the two-particle correlation method to extract the transverse momentum differential elliptic flow coefficients. The results from the AMPT model [84] are also compared with the PYTHIA8 (ANGANTYR) model [85] to cross-validate the estimation method and proper removal of nonflow effects.

This chapter is organized as follows. We begin with a brief motivation for the study in Section 4.1, followed by a description of the event generation with AMPT and PYTHIA8 models, and the detailed analysis methodology in Section 4.2. The results are described in Section 4.3, and we conclude with a summary in Section 4.4.

4.2 Event generation and analysis methodology

In this section, we briefly introduce the phenomenological models used for the simulation of heavy-ion collisions, followed by the definition of transverse spherocity and elliptic flow. Finally, we present a detailed description of the two-particle correlation technique used in this work for the extraction of elliptic flow coefficients.

4.2.1 AMPT model

To simulate proton-nucleus (p–A) and nucleus-nucleus (A–A) type collisions from RHIC to LHC energies and investigate the properties of the hot and dense nuclear matter, a multiphase transport model (AMPT) has been used extensively [84]. AMPT has dedicated modules (or phases) that mimic different evolution stages of a heavy-ion collision. The four main phases in AMPT are the initialization of collision, the parton transport, the hadronization, and the hadron cascade phase. These principal components are described below.

- **Initialization:** For the initialization of collision, the spatial and momentum distributions of the hard minijet partons and soft string excitations are obtained from the HIJING generator [86]. To calculate and convert the cross-section of the produced minijets in pp collisions to heavy-ion collisions, an in-built Glauber model is used.

- **Parton transport:** After the initialization, the produced partons are evolved through Zhang's Parton Cascade (ZPC) [87] model, which includes partonic interactions via two-body elastic parton scatterings. The scattering cross sections are obtained from perturbative QCD with screening masses.

- **Hadronization:** After the parton transport, the next phase in the evolution process is the hadronization, meaning the conversion of the partonic medium to a system of hadrons. AMPT has two different models for hadronization. Firstly, in the default model, which recombines the transported partons with their parent strings via the Lund string fragmentation model and then converts the strings into hadrons. Secondly, in the string fragmentation model, the transported partons' hadronization occurs via quark coalescence mechanism [88, 89].

- **Hadron transport:** Finally, the produced hadrons undergo the hadronic interactions, which are simulated using a relativistic transport model [90, 91]. These hadronic interactions include meson-meson, meson-baryon, and baryon-baryon-level interactions.

The default model can well describe the rapidity distribution and transverse momentum spectra for the identified particles in heavy-ion collisions at both SPS and RHIC. However, it significantly underestimates the elliptic flow at RHIC. As the default model involves only the minijet partons from HIJING in the parton cascade, the initial parton density is relatively lower to produce the necessary medium effects. However, in the string melting model, all the excited strings are also converted into partons and are combined with the minijet partons before the parton cascade phase. This enhances the parton density necessary to sustain the medium effects, which in turn results in a good description of the elliptic flow and particle p_{T} spectra in the intermediate p_{T} [92–94]. Thus, for this study involving elliptic flow measurements, we use AMPT string melting mode (AMPT version 2.26t9b) for the event generation. The settings used in this work are the same as reported in Ref. [95]. For the definition of centrality in Pb–Pb and Au–Au collisions, the impact parameter cuts are taken from Ref. [96]. To precisely match the AMPT results with the experimental data, one needs to tune various input parameters within AMPT, which is out of the scope of the current study.

4.2.2 PYTHIA8 model

PYTHIA8 [97] is a general purpose Monte Carlo event generator for simulating high-energy hadronic (pp or $p\bar{p}$), leptonic (e^+e^-) and ion-ion[1] collisions based on perturbative-QCD calculations with an emphasis on the theory of strong interaction. It includes several physics models to describe the evolution from a few-body

[1]for $A > 16$, non-deformed, and well described via Woods-Saxon density profile

hard-scattering process to the production of multiple particles in the final state. PYTHIA8 serves as a testing ground for various theoretical models, hypothesis testing, and tuning a wealth of phenomenological model parameters to experimental data. PYTHIA8 includes hard and soft interactions (*e.g.* 2– and 3– parton processes, electroweak processes, heavy-quark, and Higgs production), initial and final-state parton showers, multiparton interactions, string fragmentation, color reconnection, and resonance decays.

In PYTHIA8, the heavy-ion collisions are simulated using the ANGANTYR model [85]. This is built on top of the old non-perturbative FRITIOF program [98] in which the final state particles are produced via string fragmentation. In the ANGANTYR model, all possible nucleon–nucleon (NN) subcollisions can be assigned to their respective interaction types with an improved Glauber formalism. Further, these NN interactions are modeled through the typical pp minimum-bias framework in PYTHIA8. The current formalism generally relies on the production mechanisms involved in small systems. Thus, there is no consideration of a hot thermalized medium. Hence, it can be used to describe heavy-ion collisions as a baseline without any collective effects. In this study, the ANGANTYR model provides the necessary non-collective background, which can be used to check and compare the sensitivity of the flow extraction technique. We have used the default settings in the ANGANTYR model available in PYTHIA version 8.235 [85] to simulate heavy-ion collisions.

4.2.3 Transverse spherocity

Transverse spherocity (S_0) is an event shape observable, meaning it can disentangle events based on their geometrical shapes. Different particle production processes can produce different geometrical distributions at the final state. For example, a pure dijet event will produce two back-to-back jets of particles, which appear to be a pencil-like or cone-shaped distribution in the azimuthal space.

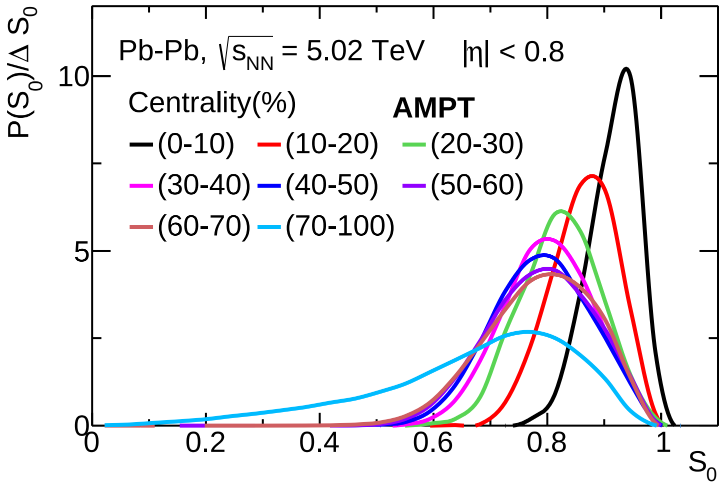

Figure 4.1: Centrality wise transverse spherocity (S_0) distribution in Pb–Pb collisions at $\sqrt{s_{\rm NN}} = 5.02$ TeV from AMPT model [100].

However, an event with spherical soft emission of particles will be distributed evenly in all directions. The role of transverse spherocity is to discriminate between these two extreme types of events. Transverse spherocity is thus an event attribute and is defined as follows.

$$S_0 = \frac{\pi^2}{4}\left(\frac{\Sigma_i\ |\vec{p}_{T_i} \times \hat{n}|}{\Sigma_i\ p_{T_i}}\right)^2. \tag{4.1}$$

Here, the unit vector, $\hat{n}(n_{\rm T}, 0)$ is chosen to minimize the term within the bracket [45, 65]. The summation runs over all the charged particles in a defined kinematic range. This definition involves the transverse momentum ($p_{\rm T}$) as well as the azimuthal angle (ϕ) of the particles. The normalization constant $\pi^2/4$ ensures the extreme limits, *i.e.*, $S_0 \in (0, 1)$. These extreme limits of S_0 correspond to different geometrical configurations. In proton+proton collisions [99], $S_0 \to 0$ means a jetty event with a back-to-back spray of particles, while $S_0 \to 1$ is an isotropic event with particles distributed in all possible angles in the azimuth. The jetty events are usually the hard events originating from pQCD processes, while the isotropic events originate from soft QCD processes. Here onwards, for the sake of simplicity, we refer transverse spherocity simply as spherocity.

Table 4.1: Centrality wise lowest and highest 20% cuts on spherocity distribution in Pb–Pb collisions at $\sqrt{s_{\mathrm{NN}}} = 5.02$ TeV from AMPT model [100].

Centrality(%)	Low-S_0 cuts	High-S_0 cuts
0–10	0.0–0.880	0.953–1.0
10–20	0.0–0.813	0.914–1.0
20–30	0.0–0.760	0.882–1.0
30–40	0.0–0.735	0.869–1.0
40–50	0.0–0.716	0.865–1.0
50–60	0.0–0.710	0.870–1.0
60–70	0.0–0.707	0.873–1.0
70–100	0.0–0.535	0.822–1.0

To estimate spherocity, events with at least five charged particles in mid-pseudorapidity, $|\eta| < 0.8$, with $p_{\mathrm{T}} > 0.15$ GeV/c are selected. This constraint is chosen to resemble the kinematic selections in the ALICE experiment at the LHC. The centrality-wise spherocity distributions in Pb–Pb collisions at $\sqrt{s_{\mathrm{NN}}} = 5.02$ TeV from AMPT are shown in Fig. 4.1. We observe that spherocity has a strong centrality dependence [100]. The peak of the distributions tends to shift towards the isotropic limit, moving from peripheral to central collisions. This effect can be attributed to the increasing number of charged particles, forming progressively denser medium as one moves from peripheral to central collisions. In central collisions, the presence of a denser medium plays a pivotal role in producing isotropic emission of particles. If jets are produced in central collisions, they evolve and interact with the medium. This medium interaction makes them lose energy, resulting in more soft particle production in the final state, which shifts the peak of the S_0 distribution towards one. For a given centrality class, events in the lowest(highest) 20% of the S_0 distribution are considered low-S_0(high-S_0) events. Events without any spherocity selection are called the S_0-integrated events. In heavy-ion collisions, events that are initially jet-dominated may evolve to a different shape at the final state due to the jet-medium interaction and the presence of a higher charged particle density. Therefore, we restrict ourselves from naming them jetty and isotropic events and instead stick to a relaxed definition of low-S_0 and high-S_0 events, respectively. The list of cuts on spherocity for this event selection in Pb–Pb collisions at $\sqrt{s_{\rm NN}} = 5.02$ TeV from AMPT is given in Tab. 4.1.

4.2.4 Elliptic flow

In non-central heavy-ion collisions, the nuclear overlap region has finite spatial anisotropy in the transverse plane due to its almond-shaped ellipsoidal geometry. As the medium expands, radial flow begins to build up, pushing the medium symmetrically in the radially outward direction. However, this initial spatial anisotropy already creates a strong differential pressure gradient inside the medium. Thus, the initial spatial anisotropy gets converted into the final state momentum anisotropy during the medium evolution process and is reflected in the azimuthal momentum distribution of the charged particles [29]. Medium evolution is usually studied in the framework of relativistic viscous hydrodynamics with dissipative effects, which is termed the collectivity of the medium. The observed effect of azimuthal anisotropy can be numerically computed via Fourier series expansion of the particle azimuthal momentum distribution [79, 101, 102]. It is given by,

$$E\frac{d^3N}{dp^3} = \frac{d^2N}{2\pi p_{\rm T}dp_{\rm T}dy}\left(1 + 2\sum_{n=1}^{\infty} v_n \cos[n(\phi - \psi_n)]\right). \tag{4.2}$$

Here, ϕ is the azimuthal angle in the transverse plane and ψ_n is the $n^{\rm th}$ harmonic event plane angle [103]. Azimuthal anisotropy has contributions from the initial geometry of the collision and fluctuations in the initial entropy and energy density. These initial state effects get embedded in the final-state multiparticle correlations through the collective expansion of the medium and are often termed as the medium response [79, 101, 102]. Thus, azimuthal anisotropy also depends on the bulk properties of the medium, such as the equation of state and transport coefficients [80, 81]. The second order coefficient in the Fourier expansion given in Eq. 4.2 is known as the elliptic flow coefficient or simply v_2. It can be obtained from Eq. 4.2 using the orthogonality relations given as,

$$v_2 = \langle \cos[2(\phi - \psi_2)] \rangle. \tag{4.3}$$

Azimuthal anisotropy has a greater contribution from v_2 in non-central collisions than other coefficients such as v_1 (directed flow) and v_3 (triangular flow). Elliptic flow is driven mainly by the initial spatial anisotropy, which is elliptical in shape in non-central collisions. Thus, v_2 has stronger centrality dependence.

Studies related to hydrodynamic calculations suggest that the collective flow is built up in the early deconfined partonic phase of the medium evolution. This partonic collectivity is then transferred to the hadrons as the partons combine to form hadrons through the quark recombination mechanism of hadronization and described via the quark coalescence model [104]. This behavior is studied as the number-of-constituent-quark (NCQ) scaling, and it leads to the observation of a higher flow of baryons than mesons in the intermediate p_{T} [105–107]. The NCQ-scaling is found to be valid in Au–Au collisions at $\sqrt{s_{\mathrm{NN}}}$ = 200 GeV at RHIC [108, 109], however, at the LHC energies in Pb–Pb collisions, this scaling is only approximate [110–112], meaning, the deviation from scaling is from 20% to 30%. Similar scaling behavior is observed using the AMPT string melting model, where the scaling is found to be valid at the top RHIC energies in Au–Au collisions [113] but violated at the LHC energies in Pb–Pb collisions. Meanwhile, the breaking of NCQ-scaling at the LHC energy in Pb–Pb collisions is attributed to the increase in the partonic phase space density [112]. The appearance of scaling in a smaller collision system, such as Si–Si collisions at the same LHC energies, leads to this conclusion [113]. Further studies with a varying magnitude of parton-parton cross sections and hadron cascade time reveal that the breaking of scaling in AMPT string melting mode is independent of these two factors [113]. In this work, the NCQ-scaling is studied in different event classes using spherocity in Au–Au collisions at $\sqrt{s_{\rm NN}}$ = 200 GeV and Pb–Pb collisions at $\sqrt{s_{\rm NN}}$ = 5.02 TeV using the AMPT string melting model [114]. This will add to understanding NCQ-scaling in different event types based on different production modes and geometrical shapes (events rich in soft particles vs. events dominated by jets).

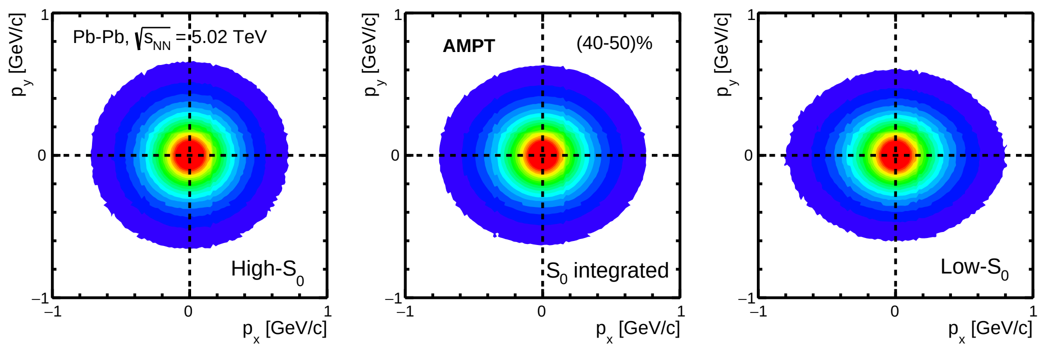

Figure 4.2: Transverse momentum space correlation (p_x vs. p_y) as a function of spherocity for (40–50)% central Pb–Pb collisions at $\sqrt{s_{\rm NN}}$ = 5.02 TeV in AMPT model [100]. Here, z-axis is the beam direction.

As the elliptic flow originates mainly from the initial spatial anisotropy, the presence of finite elliptic flow in the system should be reflected in the final-state momentum space correlation on the transverse plane (xy–plane). Due to the almond-shaped nuclear overlap region in non-central collisions, the pressure along the x–axis is higher than the y–axis, resulting in the higher momentum of particles emerging along the x–axis. This translates to an ellipse with its major axis along p_x in the transverse plane, as $p_x > p_y$. Figure 4.2 shows the transverse momentum space correlation (p_x vs. p_y) as a function of spherocity for (40–50)% central Pb–Pb collisions at $\sqrt{s_{\rm NN}}$ = 5.02 TeV in AMPT model [100]. From the first look, the presence of finite elliptic flow is evident from the S_0-integrated case.

Events with higher spherocity value tend to produce an almost circular correlation compared to the S_0-integrated case, reflecting the presence of a weaker elliptic flow component as seen in the high-S_0 case. However, changing the spherocity values towards the lower side allows us to select the events with a more elliptical correlation than the S_0-integrated case. This hints towards the presence of a higher component of elliptic flow in the low-S_0 events than the rest of the event classes. Therefore, Fig. 4.2 serves as an initial testimony of the applicability of spherocity as an event shape classifier in heavy-ion collisions.

4.2.5 Two-particle correlation method

Theoretically, the flow coefficients can be estimated from Eq. 4.2 using the orthogonality relations shown in Eq. 4.3. This requires the information on the event plane angle, ψ_n, which is generally used as a proxy to the reaction plane angle, ψ_{R}. The reaction plane is defined as the plane containing the impact parameter axis and the beam axis; then, ψ_{R} becomes the angle between the reaction plane and the x-axis. Here, the z-axis is taken as the beam direction, and the xy-plane is the transverse plane. In an ideal case, when the impact parameter axis coincides with the x-axis, xz-plane becomes the reaction plane, and $\psi_{\mathrm{R}} = 0$. In experiments, however, estimating the impact parameter and, thus, the reaction plane is almost impossible. As the impact parameter axis does not necessarily coincide with the x-axis of the detector, the reaction plane may orient in any possible direction. This makes the case challenging for estimating such observables, which require explicit information on the reaction plane angle. One way to deal with this issue is to use the untriggered multiparticle correlations described below.

In this work, we adopt the two-particle correlation method as used in experiments [82, 101, 115, 116] by constructing the untriggered[2] two-particle cor-

[2]The term untriggered correlation refers to the selection of a group of particles in a given

relation function, $C(\Delta\eta, \Delta\phi)$, between two particles in relative pseudorapidity ($\Delta\eta = \eta_a - \eta_b$) and relative azimuthal angle ($\Delta\phi = \phi_a - \phi_b$). Here, the subscripts a and b refer to different groups of charged particles in an event, which are selected in different (or the same) p_{T} intervals. Group a and b are called the trigger and associated group, respectively. The two-particle correlation function can be defined as the ratio of same-event pairs, $S(\Delta\eta, \Delta\phi)$, and mixed-event (background) pairs, $B(\Delta\eta, \Delta\phi)$, which is given as [82, 117],

$$C(\Delta\eta, \Delta\phi) = \frac{S(\Delta\eta, \Delta\phi)}{B(\Delta\eta, \Delta\phi)}. \tag{4.4}$$

Particles are selected in $|\eta| < 2.5$ with $p_{\mathrm{T}} > 0.5$ GeV/c for constructing the pairs. For the same-event pairing, both a and b groups belong to the same event; however, for the mixed-event pairing, group a particles from one event are paired with group b particles from other events. Here, five randomly chosen events from the same centrality and spherocity class are used for the event mixing. This event mixing technique removes the non-physical particle correlations and non-uniformity and improves pair acceptance. The pair azimuthal momentum distribution ($dN_{\mathrm{pairs}}/d\Delta\phi$) which is also equivalent to the one-dimensional correlation function, $C(\Delta\phi)$, can be estimated by integrating Eq. 4.4 in a given relative pseudorapidity ($\Delta\eta$) interval, which is given by [82, 117],

$$C(\Delta\phi) = \frac{dN_{\mathrm{pairs}}}{d\Delta\phi} = A \times \frac{\int S(\Delta\eta, \Delta\phi) d\Delta\eta}{\int B(\Delta\eta, \Delta\phi) d\Delta\eta}. \tag{4.5}$$

Here, $A = N_{\mathrm{pairs}}^{\mathrm{mixed}}/N_{\mathrm{pairs}}^{\mathrm{same}}$ is the normalization constant[3]. This normalization ensures that a similar number of pairs are constructed in the same-event (S) and mixed-event (B) pairing. The proper choice and reasoning of the $\Delta\eta$ interval used here is mentioned later in the text. The pair azimuthal momentum distribution

p_{T} range rather than any single particle as the trigger, *i.e.*, a particle with the highest p_{T} in an event.

[3]The $N_{\mathrm{pairs}}^{\mathrm{mixed}}$ and $N_{\mathrm{pairs}}^{\mathrm{same}}$ are the number of mixed-event pairs and same-event pairs, respectively in a chosen pseudorapidity gap.

can be expanded in $\Delta\phi$ into a Fourier series, given by [82, 117],

$$\frac{dN_{\rm pairs}}{d\Delta\phi} \propto \Big[1 + 2\sum_{n=1}^{\infty} v_{n,n}(p_{\rm T}^a, p_{\rm T}^b)\cos(n\Delta\phi)\Big]. \tag{4.6}$$

Here, $v_{n,n}(p_{\rm T}^a, p_{\rm T}^b)$ is the two-particle pair flow coefficient (similar to the definition in Eq. 4.2). From Eq. 4.5 and Eq. 4.6, it follows,

$$C(\Delta\phi) \propto \Big[1 + \sum_{n} 2v_{n,n}(p_{\rm T}^a, p_{\rm T}^b)\cos(n\Delta\phi)\Big]. \tag{4.7}$$

The term on the left can be easily estimated in experiments and simulations using the final state particle kinematics. Using a discrete Fourier transformation, the coefficients $v_{n,n}$ can be calculated as,

$$\begin{aligned} v_{n,n}(p_{\rm T}^a, p_{\rm T}^b) &= \langle\cos(n\Delta\phi)\rangle \\ &= \frac{\sum_{m=1}^{N}\cos(n\Delta\phi_m) \times C(\Delta\phi_m)}{\sum_{m=1}^{N} C(\Delta\phi_m)}. \end{aligned} \tag{4.8}$$

For this, $C(\Delta\phi)$ is estimated in very fine bins of $\Delta\phi$. Here, $N = 200$ is the total number of bins in $-\pi/2 < \Delta\phi < 3\pi/2$. Since, $v_{n,n}(p_{\rm T}^a, p_{\rm T}^b)$ is symmetric with respect to $p_{\rm T}^a$ and $p_{\rm T}^b$, we can rewrite Eq. 4.6 as follows [82, 117],

$$\frac{dN_{\rm pairs}}{d\Delta\phi} \propto \Big[1 + 2\sum_{n=1}^{\infty} v_n(p_{\rm T}^a)v_n(p_{\rm T}^b)\cos n(\Delta\phi)\Big]. \tag{4.9}$$

In the above expression, the two-particle flow coefficient, $v_{n,n}(p_{\rm T}^a, p_{\rm T}^b)$ is factorized into product two single-particle flow coefficients, as follows [117–119],

$$v_{n,n}(p_{\rm T}^a, p_{\rm T}^b) = v_n(p_{\rm T}^a)v_n(p_{\rm T}^b). \tag{4.10}$$

Here onwards, using this relation, it is straightforward to estimate the single particle flow coefficient, v_n, given by,

$$v_n(p_{\rm T}^a) = v_{n,n}(p_{\rm T}^a, p_{\rm T}^b)/\sqrt{v_{n,n}(p_{\rm T}^b, p_{\rm T}^b)}. \tag{4.11}$$

For $n = 2$, one can obtain the single particle elliptic flow coefficient, $v_2(p_{\rm T}^a)$.

Like any other method in literature, the two-particle correlation method is not an ideal one. It has its advantages and limitations. Some of them are mentioned below.

- This method has the advantage of dealing with the nonflow effect, which are flow-like correlations embedded in the system and have no relation with the initial state effects, fluctuations, or medium response leading to the actual azimuthal anisotropy. The nonflow effect has main contributions from jets and resonance decays, which appear as a jet peak in the short-range two-particle correlation function, $C(\Delta\eta, \Delta\phi)|_{\Delta\eta\to 0}$. Therefore, choosing particle pairs in a suitable pseudorapidity gap can substantially remove the nonflow effect. This is done by integrating Eq. 4.5 using a proper pseudorapidity cut excluding the jet peak region. In our analysis, the interval is found to be $2.0 < |\Delta\eta| < 4.8$. The working of this method[4] in the reduction of nonflow effect is addressed in the description of Fig. 4.3.

- While calculating the relative azimuthal angle, $\Delta\phi$, between any two particles in the event, the n^{th} event plane angle, ψ_n, is cancelled out automatically[5]. Hence, this method does not require the information of ψ_n. By saying so, a special assumption is invoked, which says ψ_n is a global phase angle for all the particles produced in the event, and hence it must be independent of the particles' pseudorapidity. This ensures a null correlation between the pseudorapidity and ψ_n. However, recent studies show pseudorapidity-dependent event plane fluctuations do exist [120, 121].

Figure 4.3 shows the transverse momentum (p_{T}^{a}) and spherocity dependence of two-particle elliptic flow coefficient ($v_{2,2}(p_{\text{T}}^{\text{a}}, p_{\text{T}}^{\text{b}})$) in minimum bias Pb–Pb collisions at $\sqrt{s_{\text{NN}}} = 5.02$ TeV using PYTHIA8 (close markers) and AMPT (open markers) models [100]. Events are selected having $\langle dN_{\text{ch}}/d\eta\rangle > 20$ in mid-rapidity

[4] Although the estimation of elliptic flow in heavy-ion collisions at the LHC energies have a negligible contribution from the nonflow effect, yet, this study based on the event-shape with a focus on jetty-like events may be sensitive to nonflow effect, justifying the usage of two-particle correlation method.

[5] For two particles A and B, $\Delta\phi_{\text{AB}} = (\phi_{\text{A}} - \psi_n) - (\phi_{\text{B}} - \psi_n) \implies \Delta\phi_{\text{AB}} = (\phi_{\text{A}} - \phi_{\text{B}})$, assuming that ψ_n is the global phase angle.

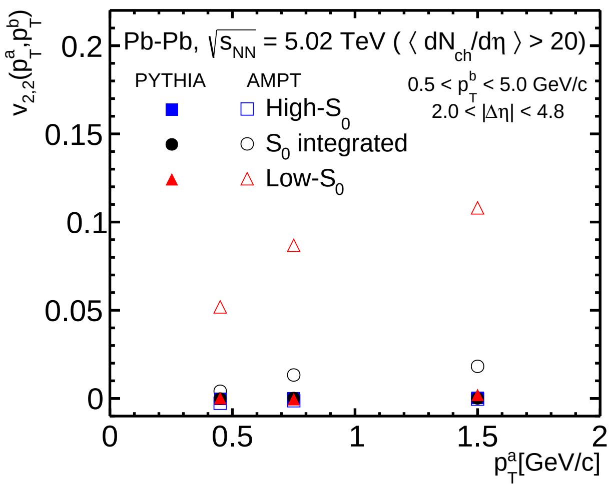

Figure 4.3: Transverse momentum ($p_{\mathrm{T}}^{\mathrm{a}}$) and spherocity dependence of two-particle elliptic flow coefficient ($v_{2,2}(p_{\mathrm{T}}^{\mathrm{a}}, p_{\mathrm{T}}^{\mathrm{b}})$) in minimum bias Pb–Pb collisions at $\sqrt{s_{\mathrm{NN}}}$ = 5.02 TeV using PYTHIA8 (close markers) and AMPT (open markers) models [100]. Events are selected having $\langle dN_{\mathrm{ch}}/d\eta \rangle > 20$ in mid-rapidity ($|\eta| < 0.8$).

($|\eta| < 0.8$). The two-particle elliptic flow coefficient is calculated using Eq. 4.8. The associated particles (group b) are chosen within $0.5 < p_{\mathrm{T}}^{b} < 5.0$ GeV/c, to be consistent with experimental measurements. Since the PYTHIA8 (ANGANTYR) model does not include any collective effects in the absence of hydrodynamics and transport pictures, any finite flow observed in the final state will be purely nonflow. However, the AMPT string melting model includes both the parton and hadron transport, which gives a reasonable estimation of collective flow in heavy-ion collisions. Therefore, a comparison between PYTHIA8 (Angantyr) and AMPT (SM) shall validate the two-particle correlation model in view of the reduction of the nonflow effect. By using the pseudorapidity cut of $2.0 < |\Delta\eta| < 4.8$, the two-particle elliptic flow coefficients from PYTHIA8 are almost zero. This signifies that by using a proper pseudorapidity cut, the remaining nonflow contributions are removed from PYTHIA8. However, the same method used in AMPT reflects finite flow. Due to the absence of collective effects in PYTHIA8 and successful reduction of nonflow, no dependence of elliptic flow on the event shapes is observed. As collective effects are included, an event shape-dependent finite flow pattern is observed for AMPT. Hence, the working of the method in the reduction of the nonflow effect is now validated, and this method can now be used to study the spherocity dependence of elliptic flow in heavy-ion collisions.

Finally, after going through the phenomenological models, event generation, and analysis methodology in detail, we discuss the results in the next section.

4.3 Results

This section presents the spherocity dependence of the two-particle correlation function, two-particle elliptic flow coefficient, and single-particle elliptic flow coefficient estimated for all charged particles. In addition, the elliptic flow for the identified light-flavour hadrons, such as $\pi^+ + \pi^-$, $K^+ + K^-$, and $p + \bar{p}$ and their NCQ scaling at the RHIC and LHC energies are also reported.

4.3.1 Elliptic flow for all charged particles

The first step in the process of elliptic flow extraction using the two-particle correlation method is constructing a one-dimensional azimuthal correlation function, $C(\Delta\phi)$. Figure 4.4 shows the spherocity dependence of two-particle azimuthal correlation function, $C(\Delta\phi)$, of all charged particles in (0–10)%, (40–50)% and (60–70)% central Pb–Pb collisions at $\sqrt{s_{\rm NN}} = 5.02$ TeV from AMPT model [100]. All charged particles in $|\eta| < 2.5$ having $0.5 < p_{\rm T}^a,\ p_{\rm T}^b < 5.0$ GeV/c are considered. The low-S_0, S_0-integrated, and high-S_0 events are represented in red, black, and blue markers, respectively. From the figure, it is evident that the magnitude or the modulation of the correlation function depends strongly on

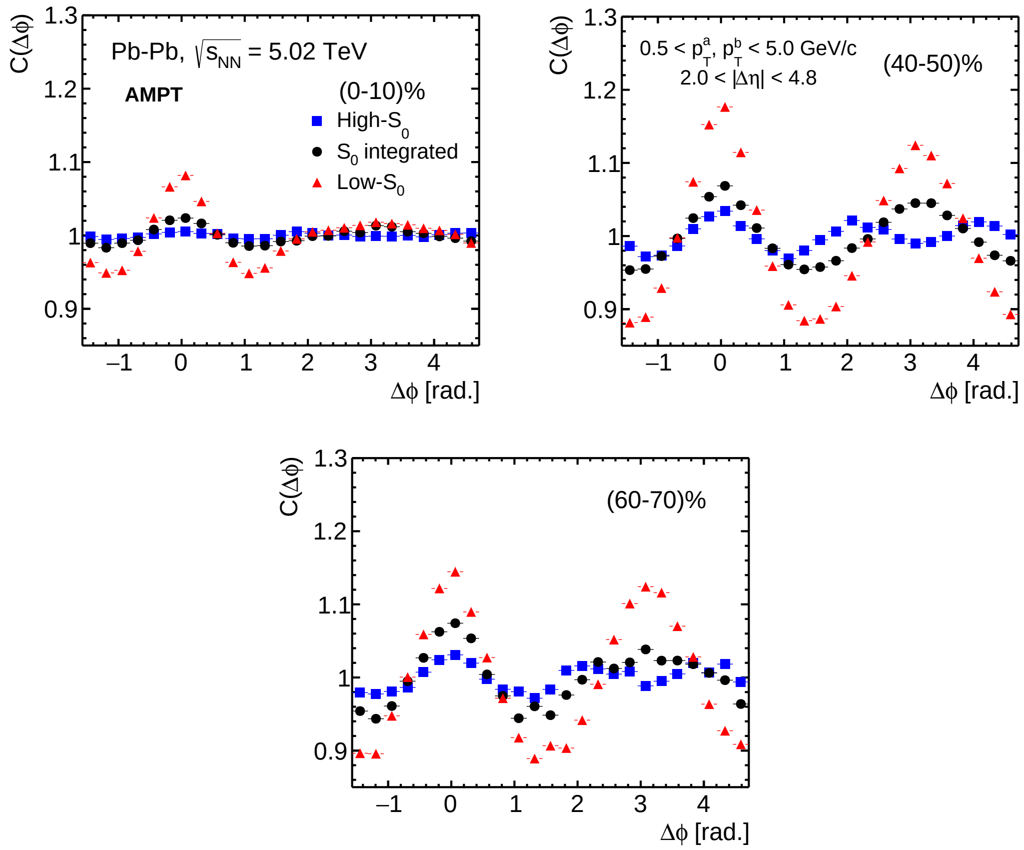

Figure 4.4: Spherocity dependence of two-particle azimuthal correlation function, $C(\Delta\phi)$, of all charged particles in (0–10)%, (40–50)% and (60–70)% central Pb–Pb collisions at $\sqrt{s_{\rm NN}}$ = 5.02 TeV from AMPT model [100].

spherocity selection. This again adds to the understanding that spherocity can be used as an event shape classifier in heavy-ion collisions. The low-S_0 events produce a stronger correlation signal than the S_0-integrated case, while the high-S_0 events have the smallest signal peaks. This hints towards the presence of a higher elliptic flow component in the low-S_0 events than the S_0-integrated events. High-S_0 events seem to contribute the least to the elliptic flow. When studied as a function of centrality, it is observed that the strength of the correlation is stronger in semi-central collisions compared to the peripheral collisions, while the most central collisions produce the weakest correlation. However, moving from central to peripheral collisions, the appearance of double peaks in the away-side ($\Delta\phi \sim \pi$) for the high-S_0 events is observed. The appearance of a prominent double peak in the away-side is usually associated with the finite contribution of the third-order harmonic coefficient in the Fourier series or the triangular flow (v_3) in the system [82]. Similar behavior of the correlation function is also seen previously in heavy-ion collisions using flow vector-based event selections [82]. Hence, in heavy-ion collisions, spherocity can help pre-select events based on the high or low values of elliptic flow as well as triangular flow.

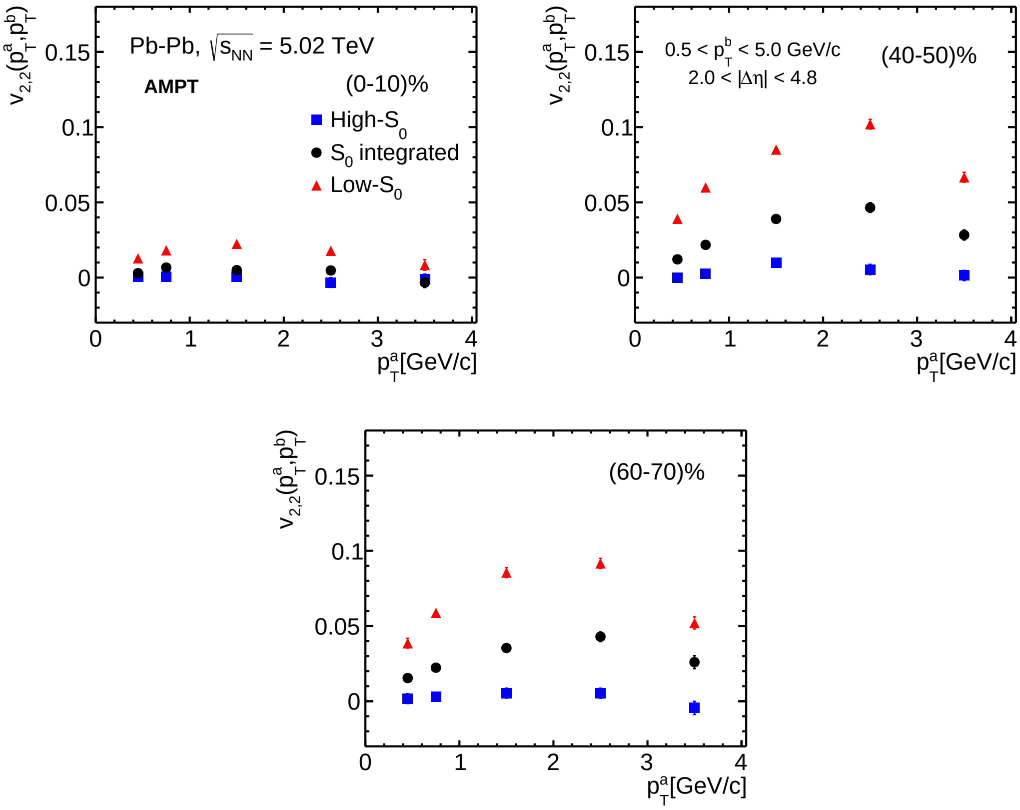

Figure 4.5: Spherocity dependence of two-particle elliptic flow coefficient, $v_{2,2}(p_{\mathrm{T}}^{\mathrm{a}}, p_{\mathrm{T}}^{\mathrm{b}})$, of all charged particles in (0–10)%, (40–50)% and (60–70)% central Pb–Pb collisions at $\sqrt{s_{\mathrm{NN}}} = 5.02$ TeV from AMPT model [100].

In Figure 4.5 and 4.6, we present the spherocity dependent two-particle elliptic flow coefficient, $v_{2,2}(p_{\mathrm{T}}^{\mathrm{a}}, p_{\mathrm{T}}^{\mathrm{b}})$, and single particle elliptic flow coefficient, $v_2(p_{\mathrm{T}}^{\mathrm{a}})$,

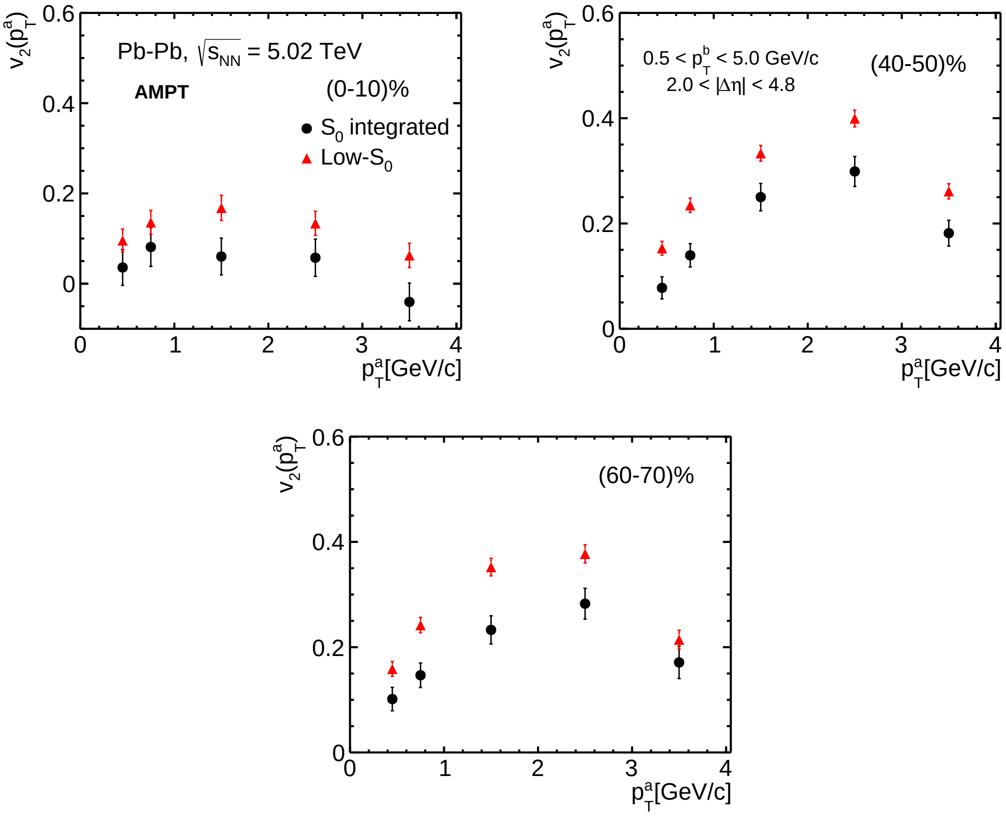

Figure 4.6: Spherocity dependence of single particle elliptic flow coefficient, $v_2(p_{\mathrm{T}}^{\mathrm{a}})$, of all charged particles in (0–10)%, (40–50)% and (60–70)% central Pb–Pb collisions at $\sqrt{s_{\mathrm{NN}}} = 5.02$ TeV from AMPT model [100].

of all charged particles in (0–10)%, (40–50)% and (60–70)% central Pb–Pb collisions at $\sqrt{s_{\mathrm{NN}}} = 5.02$ TeV from AMPT model, respectively [100]. For the measurement of transverse momentum dependence of elliptic flow, $v_2(p_{\mathrm{T}}^a)$, the trigger group (or p_{T}^a) is divided into five different bins in the range 0.5 to 4.0 GeV/c as shown in these figures. The associated group is kept common for all, *i.e.*, $0.5 < p_{\mathrm{T}}^b < 5.0$ GeV/c. As already discussed, for the reduction of nonflow, $2.0 < |\Delta\eta| < 4.8$ cut is imposed. As one moves from (0–10)% to (40–50)% centrality, there is a clear enhancement of two-particle and single-particle elliptic flow coefficient for the S_0-integrated case (black markers). This is understood as the effect of initial spatial anisotropy, which keeps on increasing from central to peripheral collisions. However, if we move further ahead to the (60–70)% case, regardless of being a peripheral system, the values of the elliptic flow coefficients are found to be slightly lesser as compared to the mid-central or (40–50)% case. In the peripheral collisions, the smaller system size and shorter lifetime of the fireball do not help fully transform the initial state effects into the final state azimuthal anisotropy despite having a higher initial geometrical anisotropy.

Now, moving on to the different event classes based on the spherocity selection, from Fig. 4.5 and Fig. 4.6, it is clear that the highest contribution to the elliptic flow comes from the low-S_0 events (red markers). It is also equally interesting to see that the high-S_0 events (blue markers) have almost zero $v_{2,2}(p_{\rm T}^a, p_{\rm T}^b)$ and thus it has a negligible contribution to elliptic flow. For this reason, during the estimation of single particle elliptic flow coefficient, the denominator in Eq. 4.11 becomes zero for the high-S_0 events; therefore, high-S_0 events are excluded in Fig. 4.6. These observations are in very good agreement with the results obtained in Fig. 4.4, where a higher modulation of the correlation function is associated with a higher contribution from the elliptic flow component. These spherocity-dependent elliptic flow trends seem to be universal and independent of the centrality selection. From Fig. 4.5 and Fig. 4.6, we understand that in addition to the initial state spatial anisotropy and medium effects, the shape of the event based on different production modes, also have a decisive role on the final state azimuthal anisotropy. It also signifies that spherocity can be used to help select events with a higher or lower value of elliptic flow and separate events based on their geometrical shapes and dominant production modes in heavy-ion collisions.

4.3.2 Elliptic flow for identified particles

Within the same formalism, we proceed to estimate the elliptic flow for identified light-flavour hadrons such as $\pi^+ + \pi^-$, $K^+ + K^-$, and $p + \bar{p}$ at the RHIC and

LHC energies and study the spherocity dependent NCQ scaling behavior.

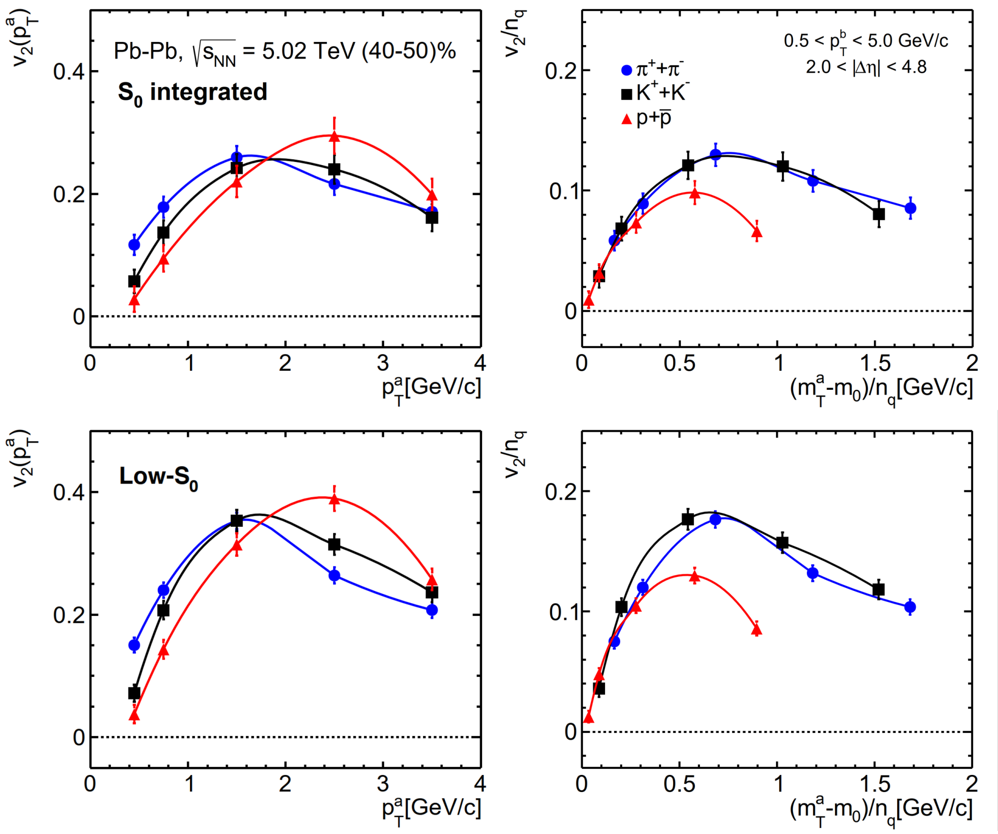

Figure 4.7: Left column shows the transverse momentum dependence of elliptic flow, $v_2(p_T^a)$, for $\pi^+ + \pi^-$, $K^+ + K^-$, and $p + \bar{p}$ in S_0-integrated (top panel) and low-S_0 (bottom panel) events in (40–50)% central Pb–Pb collisions at $\sqrt{s_{NN}}$ = 5.02 TeV from AMPT model [114]. The right column shows the respective NCQ scaling behavior.

In Figure 4.7, the left column shows the transverse momentum dependence of elliptic flow, $v_2(p_T^a)$, for $\pi^+ + \pi^-$ (blue circle), $K^+ + K^-$ (black square), and $p + \bar{p}$ (red triangle) in S_0-integrated (top panel) and low-S_0 (bottom panel) events in (40–50)% central Pb–Pb collisions at $\sqrt{s_{NN}}$ = 5.02 TeV from AMPT model [114]. Similar to the trends observed in Fig. 4.6, the low-S_0 events also have a higher contribution to pion, kaon, and proton elliptic flow as compared to the S_0-integrated events. At first glance, in low-p_T ($p_T^a < 2.0$ GeV/c), both S_0-integrated and low-

S_0 events show a mass dependent $v_2(p_{\rm T}^a)$ behaviour. Being the lightest meson, pion has a higher v_2 compared to kaon, while v_2 for proton is the smallest among them. This mass hierarchy of v_2 in low-$p_{\rm T}$ could arise due to an interplay of radial and elliptic flow. At intermediate-$p_{\rm T}$, a clear separation of baryon-meson elliptic flow is observed for both S_0-integrated and low-S_0 events. This splitting of baryon and meson v_2 into two separate groups arises from the quark coalescence mechanism of hadronization in the AMPT string melting model. This behavior is seen in both the event classes, and a slight enhancement is observed for the low-S_0 case.

On the right column of Fig 4.7, the number-of-constituent-quark scaling for $\pi^+ + \pi^-$, $K^+ + K^-$, and $p + \bar{p}$ in S_0-integrated (top panel) and low-S_0 (bottom panel) events in (40–50)% central Pb–Pb collisions at $\sqrt{s_{\rm NN}}$ = 5.02 TeV from AMPT model have been shown [114]. If the production of hadrons is dominated by the quark recombination mechanism of hadronization, the number-of-constituent-quark scaling is trivial, which states that the flow of hadrons could be expressed in terms of the flow acquired by their constituents (*i.e.*, quarks). Mathematically, this can be written as,

$$v_2^h(p_{\rm T}^a) = n_q \times v_2^q(p_{\rm T}^a/n_q). \tag{4.12}$$

Here, $v_2^h(p_{\rm T}^a)$ is the elliptic flow of hadron, n_q is the number-of-constituent-quarks and $v_2^q(p_{\rm T}^a/n_q)$ is the elliptic flow of the constituent-quarks. The scaling can be expressed as a function of the transverse kinetic energy, which is defined as $E_{\rm T}^{\rm kin.} = m_{\rm T} - m_0$. Here, $m_{\rm T} = \sqrt{p_{\rm T}^2 + m_0^2}$, is the transverse mass and m_0 is the rest mass of the particle. From Fig. 4.7, it is observed that both S_0-integrated and low-S_0 events violate the scaling in the intermediate-$p_{\rm T}$ range at the LHC. This observation is in good agreement with the experimental data of Pb–Pb collisions from the LHC [110–112]. It is also interesting to note that the scaling seems to have a larger deviation for the case of low-S_0 events compared to the S_0-integrated events. From these observations, it is inferred that the quark coalescence model for the hadronization is not the only deciding factor as far as NCQ scaling is concerned. It appears that the production of a larger system with a denser partonic medium at the LHC can somehow violate the scaling. To investigate this behavior, we proceed to study the NCQ scaling in different event classes in a smaller system at a lower collision energy.

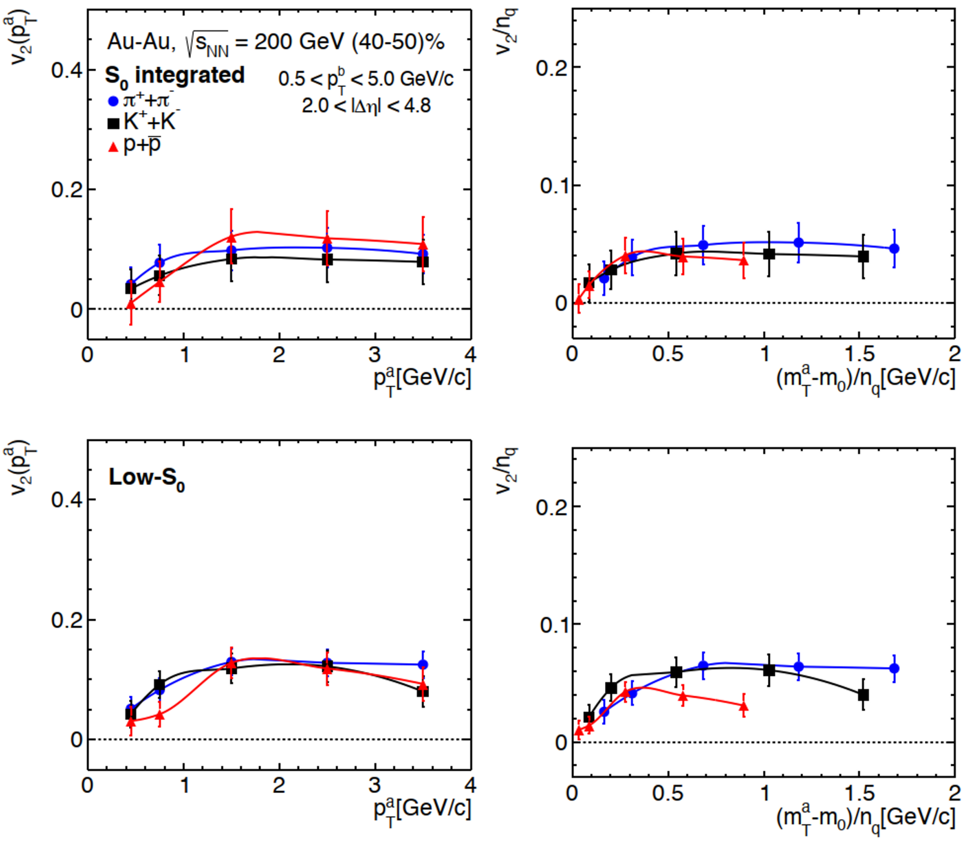

Figure 4.8: Left column shows the transverse momentum dependence of elliptic flow, $v_2(p_{\mathrm{T}}^a)$, for $\pi^+ + \pi^-$, $K^+ + K^-$, and $p + \bar{p}$ in S_0-integrated (top panel) and low-S_0 (bottom panel) events in (40–50)% central Au–Au collisions at $\sqrt{s_{\mathrm{NN}}}$ = 200 GeV from AMPT model [114]. The right column shows the respective NCQ scaling behavior.

Figure 4.8 shows the transverse momentum dependence of elliptic flow, $v_2(p_{\mathrm{T}}^a)$, for $\pi^+ + \pi^-$, $K^+ + K^-$, and $p + \bar{p}$ in S_0-integrated (top panel) and low-S_0 (bottom panel) events in (40–50)% central Au–Au collisions at $\sqrt{s_{\rm NN}}$ = 200 GeV from AMPT model [114]. By comparing Fig. 4.7 and 4.8, one can observe the system size and collision energy dependence of elliptic flow. Although a finite flow is observed at RHIC, the magnitude of elliptic flow is smaller than that of LHC. In addition, a smaller enhancement of v_2 for the low-S_0 events is observed compared to the S_0-integrated events. Now, moving onto the NCQ scaling shown in the right column of Fig. 4.8, it is important to observe that the scaling is valid for the S_0-integrated case in Au–Au collisions at $\sqrt{s_{\rm NN}}$ = 200 GeV while it is seen to be violated for the Pb–Pb collisions at $\sqrt{s_{\rm NN}}$ = 5.02 TeV in AMPT string melting model. This validity of the NCQ scaling is also observed in experiments at RHIC [108, 109, 122–124]. This hints towards the fact that in the presence of a denser initial partonic medium leading to a higher particle multiplicity in the final state can be a deciding factor for the constituent-quark scaling to be violated.

While the NCQ-scaling is still valid for the S_0-integrated events at RHIC, we also observe that it is violated for Au–Au collisions at $\sqrt{s_{\rm NN}}$ = 200 GeV for the low-S_0 events as shown in the bottom right panel in Fig. 4.8. This figure is important as for the first time, the violation of NCQ-scaling at RHIC is reported using this event shape analysis. The low-S_0 events are dominated by particles with relatively higher momentum. At higher momentum, the fragmentation process takes over the recombination picture of hadronization, and this may lead to the breaking of the NCQ scaling in low-S_0 events. These results are still model-dependent, and to draw a solid conclusion, event shape-dependent studies should be performed at the RHIC and LHC experiments.

4.4 Summary

In summary, the first transverse spherocity-dependent elliptic flow analysis measurements are reported in Pb–Pb collisions at $\sqrt{s_{\rm NN}}$ = 5.02 TeV using the AMPT model. This study utilizes the two-particle correlation technique for flow estimation. By using a proper relative pseudorapidity cut between particle pairs, substantial nonflow can be removed from the calculation. The model comparison between AMPT with collectivity and PYTHIA8 (ANGANTYR) with a non-collective background shows that the final measurements are almost free from any nonflow effects. The two-particle correlation function, two-particle elliptic flow coefficient, and single-particle elliptic flow coefficient for all charged particles are studied in low-S_0, S_0-integrated and high-S_0 events. From the results, it is concluded that high-S_0 events have almost zero contribution towards elliptic flow, while the low-S_0 events have the largest contribution to elliptic flow in heavy-ion collisions. Thus, spherocity is seen to be strongly anti-correlated with the elliptic flow in heavy-ion collisions. The appearance of away-side double peaks in the two-particle azimuthal correlation function in the high-S_0 events hints towards the presence of finite triangular flow in high-S_0 events, while this effect seems to be absent in the low-S_0 events. This suggests that triangular flow should be positively correlated with the event spherocity. These observations add to the understanding that spherocity can be used as an event shape classifier in heavy-ion collisions. Thus, spherocity can be used to select events based on different degrees of collectivity in heavy-ion collisions.

Further, we extend the formalism to study the elliptic flow and its NCQ-scaling behavior as a function of spherocity for identified light-flavour hadrons such as $\pi^+ + \pi^-$, $K^+ + K^-$, and $p + \bar{p}$ at the RHIC and LHC energies. The mass-dependent elliptic flow at low-$p_{\rm T}$ and the baryon-meson separation at intermediate-$p_{\rm T}$ is observed in both S_0-integrated and low-S_0 events. However, the splitting of baryon-meson elliptic flow seems to be more prominent for the low-S_0 events at intermediate-$p_{\rm T}$ compared to the S_0-integrated case at the LHC. Using the quark coalescence mechanism of hadronization in the AMPT string melting model, the NCQ-scaling is found to be violated in S_0-integrated events at the LHC; however, the same is found to be valid at RHIC. This suggests that in addition to the quark recombination mechanism, the presence of a larger system with a denser partonic medium at the LHC might also play an important role in the final state NCQ-scaling of the hadrons. Again, the NCQ-scaling is found to be violated for the low-S_0 events at both RHIC and LHC. Although the NCQ-scaling is valid for the S_0-integrated events at RHIC, its violation in low-S_0 events is reported for the first time at RHIC through this study. Initial understanding hints towards the dominance of the fragmentation mechanism of hadronization in low-S_0 events to be the cause of the breaking of this scaling. From this study, it is understood that the spherocity-dependent azimuthal anisotropy behavior is universal; hence, it can be applied to heavy-ion collisions at the RHIC and LHC energies irrespective of the centrality of the collision.

One thing to note here is that the AMPT string melting model can well explain the elliptic flow at RHIC and LHC energies for the S_0-integrated case; therefore, any conclusion derived from the study for the other spherocity classes can be assumed to mimic the experimental data. However, these results can still be model-dependent, and to arrive at a final conclusion, event-shape-dependent studies based on spherocity should be performed at the experiments at RHIC and LHC. Any deviation from the model predictions can also be very interesting and can help tune various aspects of the model. Further studies on the correlation of spherocity on higher-order harmonics of azimuthal anisotropy can also reveal more information on probing the initial state effects through the final state observables in heavy-ion collisions and the characterization of the medium effects.

Chapter 5

Deep learning based estimator for elliptic flow in heavy-ion collisions

5.1 Motivation

Ultra-relativistic heavy-ion collisions have witnessed remarkable developments over the past few decades both in experiments as well as in theory for the exploration of the rich physics of hot and dense nuclear matter, *i.e.*, quark-gluon plasma (QGP). The formation of such a transient deconfined medium of strongly interacting partons has already been concluded in such collisions [125]. In several studies related to QGP, particular emphasis is always given to the presence of finite transverse collective expansion (also known as collective flow) for the characterization of the medium formed in heavy-ion collisions [29, 79]. Moreover, this collective expansion of the medium is anisotropic, leading to the anisotropic emission of particles in the momentum space. Thus, the particles' azimuthal momentum distribution can be expressed via Fourier series expansion as given in Eq. 4.2, such that the coefficients of the expansion, v_n, quantify the n^{th} order anisotropic flow coefficients [102]. Experimental measurements of these finite (or nonzero) anisotropic flow coefficients in heavy-ion collisions agree with the hydrodynamic evolution picture of the QGP [108, 110, 126, 127]. Thus, the presence of finite azimuthal anisotropy, mainly the second-order flow coefficient, v_2 (or elliptic flow), is considered to be one of the signatures of QGP, and it strongly hints towards the medium thermalization in the early stages of the collision.

Over the years, special attention has been given to the theoretical understanding of elliptic flow by modeling the medium evolution through relativistic hydrodynamics. Although these models based on relativistic hydrodynamics with dissipative effects could explain some of the low-$p_{\rm T}$ phenomena, they failed to predict the complete $p_{\rm T}$ dependence of the experimentally observed elliptic flow [128, 129]. The low-$p_{\rm T}$ sector is believed to have influence from the radial flow and resonance decays, whereas jet quenching and path length dependent effects such as in-medium parton energy loss might play a pivotal role in the intermediate to high-$p_{\rm T}$ sector. Thus, simple hydro models lacking these features fail to explain the data [129, 130]. This issue is resolved to a great extent via hybrid models, *e.g.*, hydro+transport, that apply hydrodynamics to the dense QGP phase and kinetic transport models to the microscopic hadron cascade phase [131–134]. A recent study implements hydro freezeout at low-$p_{\rm T}$, quark coalescence at intermediate-$p_{\rm T}$ and fragmentation picture at high-$p_{\rm T}$ in a coupled linear Boltzmann transport-hydro model. This could simultaneously explain the complete $p_{\rm T}$ dependence of nuclear modification factor ($R_{\rm AA}$) and v_2 in high-energy heavy-ion collisions [135].

From the experimental side, there are challenges in estimating the elliptic flow coefficient. From Eq. 4.3, it is understood that the estimation of v_2 requires the information of the reaction plane angle on an event-by-event basis. However, the estimation of the impact parameter, hence the reaction plane angle, is nontrivial in experiments [101]. Several methods are explored in the literature to effectively measure the flow coefficients from experimental data. Mainly, the standard event plane method or the complex reaction plane identification method [83], the multi-particle correlation and cumulant method [136, 137], and the Lee-Yang zeroes method [138] are emphasized. In addition to that, attempts are also made to use unsupervised machine learning (ML) methods such as the principal component analysis for the flow estimation [139–143].

For the first time, we report a deep learning-based machine learning method for the estimation of elliptic flow in heavy-ion collisions [144, 145]. The motivation of this study is to implement a feed-forward deep neural network in heavy-ion collisions to estimate the elliptic flow coefficient from the final state particle kinematics. The flow coefficients are embedded in the final state multi-particle correlations; hence, a deep neural network can be trained on simulated data to learn these correlations and efficiently measure the flow coefficients. The machine learning model is trained on simulated minimum bias Pb–Pb collisions at $\sqrt{s_{\rm NN}}$ = 5.02 TeV using the AMPT string melting model. After successful training, the same ML model is applied across several collision systems at RHIC and LHC energies. Since elliptic flow has several dependencies, such as centrality, transverse momentum, particle species (or mass), and collision energy, it is interesting to explore the prediction capability of the ML model in these sectors. The model predictions for the elliptic flow of light-flavor hadrons and the number-of-constituent-quark (NCQ) scaling depicting the partonic level collectivity are also covered. These results from the ML model are compared to both experimental findings and traditional measurements from standalone simulation[1] using the AMPT model, wherever possible.

This chapter is organized as follows. We begin with a brief motivation for the study in Section 5.1, followed by a short description of the event generation and target observable in Section 5.2. In Section 5.3, we describe the working principles of the deep learning estimator with model building and training. It also

[1]Here, the term "standalone simulation" refers to the event simulation without any detector effects.

reports the quality assurance figures and estimation of systematic uncertainty. The results are presented in Section 5.4, and the key findings are summarized in Section 5.5.

5.2 Event generation and target observable

For the training of the deep learning model, necessary heavy-ion collisions are simulated using the AMPT string melting model [84]. The AMPT model and its main components are already discussed in Section 4.2.1. We have specifically used the AMPT version 2.26t9b with similar settings for Pb–Pb collisions at $\sqrt{s_{\rm NN}}$ = 2.76 and 5.02 TeV, Xe–Xe collisions at $\sqrt{s_{\rm NN}}$ = 5.44 TeV and Au–Au collisions at $\sqrt{s_{\rm NN}}$ = 200 GeV as already reported in Refs. [95, 100, 114]. For the centrality selection, we have used impact parameter slicing, and these cuts are taken from Ref. [96].

In a much simpler context, a machine learning model maps one or many input variables to one or many output variables. These input-output correlations are shown to the machine during its training in the form of example data. In the supervised learning case, the output of the model can be a class, a label (discrete value), or a real number (continuous value). The former type is called a classification problem, whereas the latter one is a regression problem. In this work, the goal is to map the final state particle kinematics to the elliptic flow on an event-by-event basis. This suits a machine learning-based regression problem. Sometimes, the output variables are also termed as the target observable, and in our case, this is the elliptic flow. The estimation of elliptic flow for the training and testing dataset is done following the standard event plane method as given in Eq. 4.3 and described in Ref. [83]. In AMPT simulation, one can turn off the random orientation of the reaction plane and set it along the x-axis; this effectively makes the reaction plane angle $\psi_{\rm R} = 0$. Then, the expression for elliptic flow simplifies to $v_2(p_{\rm T}, y) = \langle\cos[n\phi_i]\rangle$. Here, the average is taken over all the particles in a given p_{T} and y bin, and ϕ_i is the azimuthal angle of the i^{th}-particle.

5.3 Deep learning estimator

In this section, first, we present a brief description of the working principles of deep neural networks. The detailed analysis steps, including the input features, the model architecture, training, and quality assurance, are discussed next. The estimation of systematic uncertainty is also covered.

5.3.1 Deep neural network

Artificial neural networks have become ubiquitous in contemporary machine learning. Despite originating alongside early digital computers in the 1950s, their widespread adoption has surged more recently, thanks to technological advancements such as miniaturized central processing units (CPUs), powerful graphical processing units (GPUs), accelerated and extensive internet connectivity, and the internet of things (IoT) enabling the collection and processing of big data sets. While computers can still outperform humans on numerical calculations, they face significant difficulty in tasks such as natural language processing, pattern recognition, and anomaly detection, to name a few. Inspired by the biological nervous system, the artificial neural network processes several inputs to provide a task-specific output. This is similar to animals reacting to external stimuli.

An artificial neural network has several components. One such artificial neural network in its simplest form is shown in Fig. 5.1 with one input layer, one intermediate (hidden) layer, and one output layer. In this example, the input layer takes three fixed numerical input values, which are then mapped through the intermediate layer to produce an output. Each layer has several active computational elements known as the neurons or nodes, shown as bubbles in the

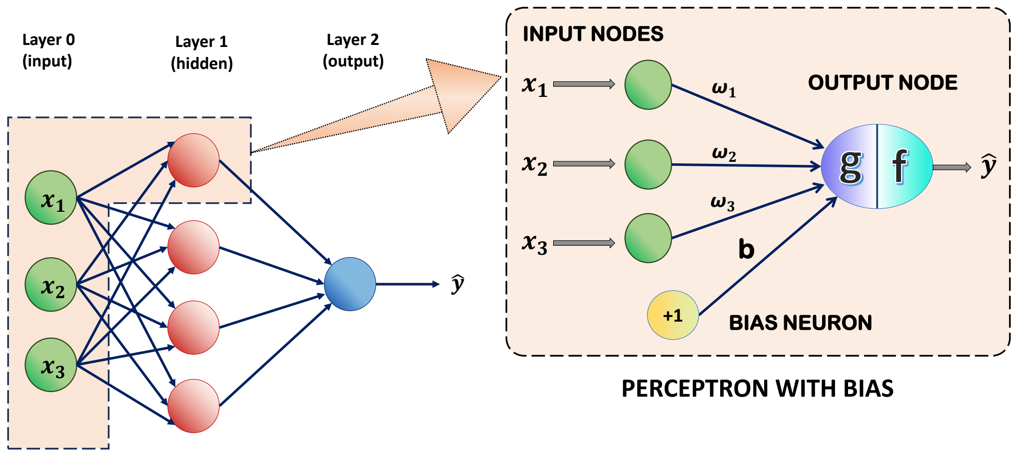

Figure 5.1: Schematics of an artificial neural network with the structure of a perceptron.

diagram. The nodes at the input layer do not perform any mathematical operation on their own; they simply pass the input vector to the next layer in the network. For this passing of information from one layer to the other, the nodes between two consecutive layers are interconnected (shown as forward arrows), forming many perceptrons. Therefore, artificial neural networks are sometimes referred to as multi-layer perceptrons (MLPs). The original idea and working of perceptrons were demonstrated by McCulloch-Pitts Neuron (1943), followed by Rosenblatt's Perceptron (1957). If all the nodes of two consecutive layers are fully interconnected, then the layers are termed dense layers. Artificial neural networks with more than one hidden layer are usually preferred and are called deep neural networks (DNNs).

On the right-hand side of Fig. 5.1, the working of a single perceptron has been highlighted. Here, the three input nodes are connected to the first node of the hidden layer, which forms a perceptron. Each perceptron performs two operations: first, it aggregates the values from the nodes of the previous layer, and second, it transforms the aggregated value based on certain criteria given in the form of an activation function. For each node-to-node connection, the perceptron assigns its own weights. In the diagram, the weights are given as $\mathbf{W} = \{w_1, w_2, w_3\}$ which connect the input $\mathbf{X} = \{x_1, x_2, x_3\}$, respectively. Additionally, one extra node with a constant value 1 with the weight parameter b is connected to the perceptron, which is called the bias node. The aggregator (g) then computes the following expression,

$$g(\mathbf{X}; \mathbf{W}, b) = \mathbf{W}.\mathbf{X}^{\mathrm{T}} + b = \sum_{i=1}^{d=3} w_i.x_i + b \tag{5.1}$$

The aggregated value, also known as *pre-activation*, is then transformed through a suitable activation function (f), which introduces nonlinearity into the network. The second step of the perceptron is to compute the following expression,

$$\hat{y}(\mathbf{X}) = f(g(\mathbf{X}; \mathbf{W}, b)) = f(\mathbf{W}.\mathbf{X}^{\mathrm{T}} + b) \tag{5.2}$$

Here, the final output or the prediction of the perceptron, $\hat{y}(\mathbf{X})$ is also called an *activation*. The choice of an activation function is crucial. Functions such as *sigmoid*, *tanh* or *sign* are typically used for classification tasks, whereas *ReLU* and *Hard Tanh* are often preferred for regression problems. The output layer often uses the linear (identity) activation function. These activation functions are defined and displayed in Fig. 5.2.

After calculating the *activation* over several such perceptrons[2], the final activation or the prediction of the model is then compared to the actual value of the output. The goal is to reproduce the true output value by minimizing the error in the prediction. For this, a suitable loss function (L) is used, which basically estimates the difference between the predicted value and the true value. Some popular loss functions are mentioned below.

[2] In Fig. 5.1, we have four perceptrons for the hidden layer and one for the output layer, so it makes five perceptrons in total.

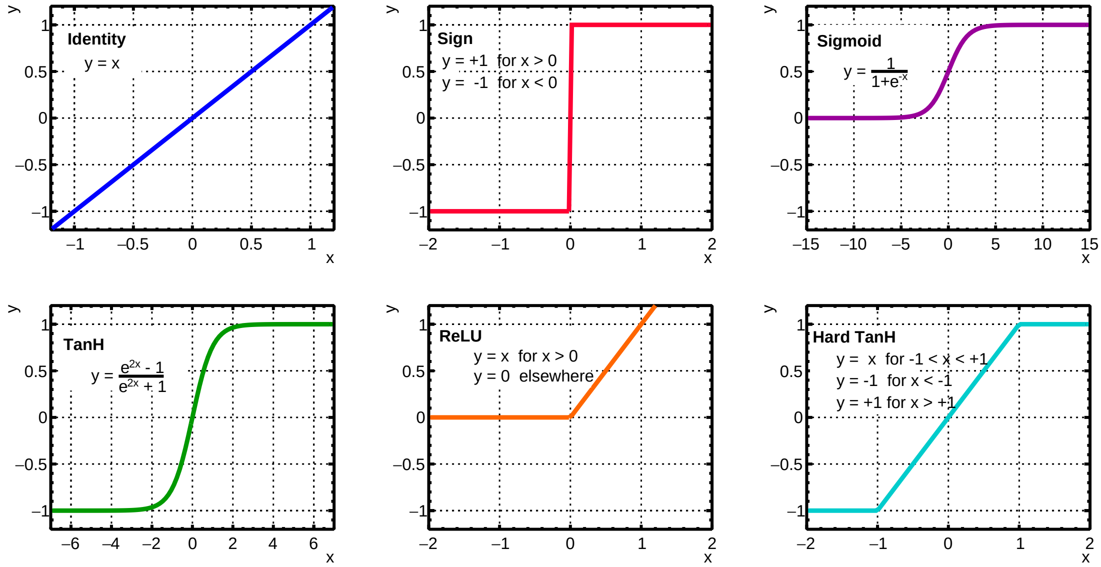

Figure 5.2: Definition and nature of a few popular activation functions.

Least-squares:

$$l(y_i, \hat{y}(x_i)) = \frac{1}{2}(y_i - \hat{y}(x_i))^2 \tag{5.3}$$

Least-absolute-deviation:

$$l(y_i, \hat{y}(x_i)) = |y_i - \hat{y}(x_i)| \tag{5.4}$$

Huber:

$$l(y_i, \hat{y}(x_i)) = \begin{cases} \frac{1}{2}(y_i - \hat{y}(x_i))^2, & |y_i - \hat{y}(x_i)| \leq \delta \\ \delta(|y_i - \hat{y}(x_i)| - \delta/2), & |y_i - \hat{y}(x_i)| > \delta \end{cases} \tag{5.5}$$

Here, δ is known as the transition point that defines those residual values that are considered to be "outliers," subject to absolute rather than squared-error loss. For residual less than or equal to δ, the Huber loss function becomes the least-squares loss.

The process in which the input values pass through the network to produce an output is called a cycle. In each cycle, the loss function is computed taking a small set of input values, called *batches*, and then the algorithm tries to minimize the loss with respect to the weights and biases. This optimization continues through the entire training dataset in a random order and iteratively adjusts the weights and biases until the convergence criterion is reached. The weights and biases in the network are updated in each cycle, and such a cycle is called an *epoch*. For a single perceptron, the expression for the optimization of weights in the i^{th} training cycle with a loss L_i can be given as,

$$\mathbf{W} \Leftarrow \mathbf{W} - \alpha \frac{\partial L_i}{\partial \mathbf{W}} \tag{5.6}$$

This particular way of updating the weights using gradients is called the gradient descent method. Here, α is called the learning rate, which controls the rate of convergence. Now, to compute these gradients, $\frac{\partial L_i}{\partial \mathbf{W}}$, a closed functional form of the loss function is desired. However, for an MLP, these loss functions are too massive, and it is not easy to write them in closed forms. This creates challenges in the calculation of the gradients. Here, the *backpropagation* technique comes to the rescue, which is well known in the field of neural networks. The process of using a *batch* of inputs to calculate the loss of the outputs is called a *forward phase*. Then, the algorithm computes the gradients of the loss function only at the final output layer. This process is computationally faster. The weights are then updated in a reverse order, starting from the interface of the output layer and the last hidden layer using the chain rule. This is known as the *backward phase*. For a detailed derivation and working of this method, one can refer to Ref. [146]. Once the weights and biases are obtained, the training process is stopped, and the model is frozen to make predictions on a new dataset.

Models based on deep neural networks find many applications in high-energy particle physics. Deep learning models are used in classical papers [147, 148], and problems related to jet tagging [149–151], PID and track reconstruction [152–154] and heavy-ion physics [155–158]. Interested readers may refer [159], which contains an excellent collection of ML papers in particle physics, cosmology, and beyond.

For the implementation of the DNN model, KERAS v2.7.0 deep learning Application Programming Interface (API) [160] with TensorFlow v2.7.0 [161] has been used in this work. The code is developed in PYTHON with the help of the scikit-learn framework [162].

5.3.2 Input to the machine

Heavy-ion collisions produce a multitude of particles in the final state. These particles are detected as they interact with the designated detectors and are reconstructed as tracks. Thus, the track level information such as p_{T}, η, ϕ, and charge can be extracted. These track-level features are often convoluted with various detector effects and can differ from the particle (true) level features. However, heavy-ion collisions simulated using standalone Monte Carlo generators can provide particle-level information. These final state particle kinematics information from the event generator can serve as the input features for any deep neural network. As the particle multiplicity varies from event to event, the variable-sized input features can not be directly fed to the neural network. As a workaround, the two-dimensional binned $(\eta - \phi)$ freezeout surface for all charged hadrons can be used as the primary input feature space. Here, $\eta \in [-0.8, 0.8]$, and $\phi \in [0, 2\pi]$. Additional particle features can be included as different layers of the primary feature space by reweighting the existing bins. The different weights serve as the extra information necessary for the network. Here, we choose three additional layers with p_{T}, mass, and $\log(\sqrt{s_{\mathrm{NN}}/s_0})$ weights on the $(\eta - \phi)$ space. The term, $\log(\sqrt{s_{\mathrm{NN}}/s_0})$ is related to collision energy[3].

Figure 5.3 demonstrates the three different layers of $(\eta - \phi)$ freezeout surface obtained from a single minimum bias Pb–Pb collision at $\sqrt{s_{\mathrm{NN}}} = 5.02$ TeV from AMPT model [144]. The p_{T}, mass, and energy-weighted plots are shown in

[3] $\sqrt{s_0} = 1$ GeV makes $\sqrt{s_{\mathrm{NN}}/s_0}$ unit-less.

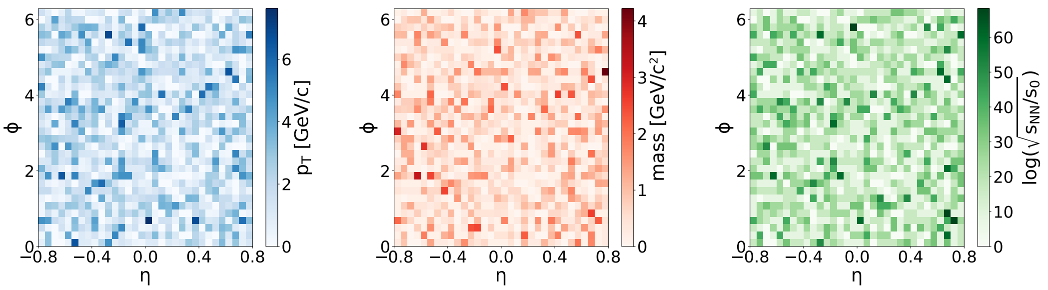

Figure 5.3: The ($\eta-\phi$) freezeout surface obtained from a single minimum bias Pb–Pb collision at $\sqrt{s_{\rm NN}} = 5.02$ TeV from AMPT with 32×32 bins each, displaying the three layers of input for the deep neural network [144].

blue, red, and green colors, respectively. The choice of 32×32 bins for each layer has been decided carefully, looking into the model performance, complexity, parameter space, and resource requirement, which is covered in Section 5.3.3. The three layers of the input space provide a combination of 3072 ($= 32 \times 32 \times 3$) features for each collision. The numerical values of these features are then extracted from the respective bin contents and converted into a linear array of dimension 1×3072. All charged particles within the midrapidity range of $|\eta| < 0.8$ are taken into account. For the centrality-dependent studies, including the quality assurance figures, particles with $0.2 < p_{\rm T} < 5.0$ GeV/c are considered; however, for the transverse momentum-dependent studies, we prefer particles with $p_{\rm T} > 0.15$ GeV/c unless mentioned otherwise. This is done to maintain consistent kinematics criteria for data comparison. Finally, the input array is normalized using the *"L2 Norm"*, which ensures the square root of the sum of squares of the elements in the array equals one. This is also known as the Euclidean norm. This array normalization creates a machine-friendly representation of data. This measure is also crucial as it aids in expediting the convergence of the regression estimator by maintaining numerical stability throughout the computation.

5.3.3 Training and quality assurance

The left plot of Fig. 5.4 shows the schematics of the deep neural network (DNN) architecture used in this work. The network begins with an input vector of dimension 1×3072, followed by four hidden layers having $128, 256, 256, 256$ neurons each. All these layers use a rectified linear unit activation function, which is defined as $\mathrm{ReLU}(x) = \max\{0, x\}$ [163]. The output layer consists of a single node, which is v_2, and it uses a linear activation function. The deep neural network uses *adam* algorithm as the optimizer [164] with the mean-squared error (MSE) as the loss function, which is given by

$$\mathrm{Loss(MSE)} = \frac{1}{N_{\mathrm{events}}} \sum_{n=1}^{N_{\mathrm{events}}} \left(v_{2_n}^{\mathrm{true}} - v_{2_n}^{\mathrm{pred.}}\right)^2. \tag{5.7}$$

All layers are fully connected dense layers. Regularization methods such as the *L2 regularization* and *dropout* are found to hamper the model performance, hence they are excluded [144, 145]. To mitigate any over-fitting[4] issues, a simple early-stopping callback is implemented. This method calls back the training if the model performance is not improved over a certain number of epochs, specified as the patience level. Here, the optimizer runs with a maximum of 60 epochs with 32 batch sizes and an early stopping patience level of a maximum of 10 epochs. The number of events in the training, validation, and testing dataset are obtained by splitting the total simulated events in the input data in 8:1:1, respectively. The model is trained on event-by-event data of all charged particles obtained from 2×10^5 minimum bias Pb–Pb collisions at $\sqrt{s_{\mathrm{NN}}} = 5.02$ TeV simulated with the AMPT model. All other hyperparameters of the optimizer and dense layers are kept at their default values.

The right plot in Fig. 5.4 shows the evolution of the mean squared loss function versus epoch size during the training and validation runs of the proposed deep

[4]Over-fitting refers to the scenario where the model picks up superfine details of the data during training yet performs poorly on a validation dataset.

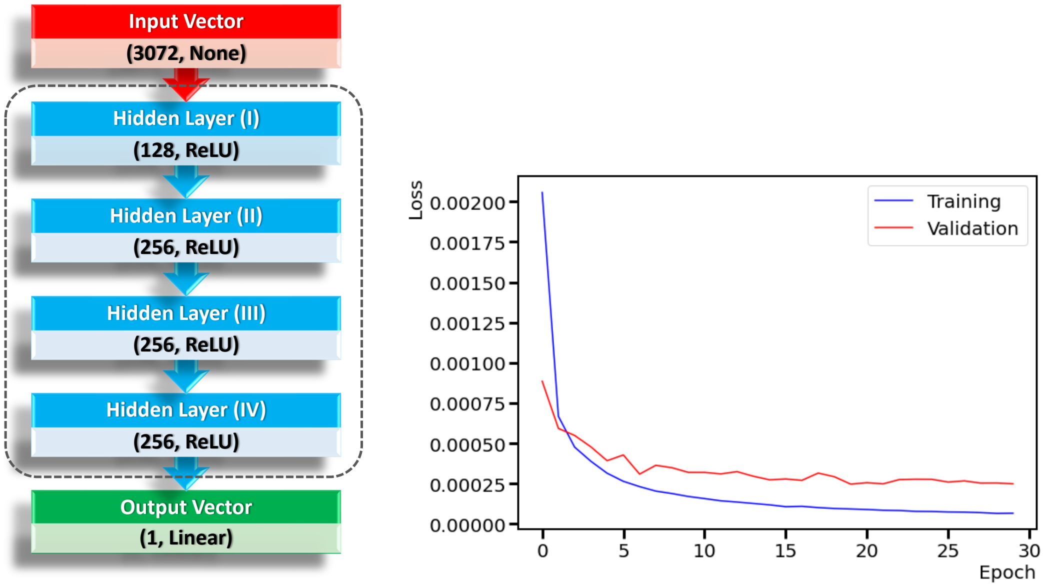

Figure 5.4: Left: Schematics of the deep neural network architecture with the number of nodes in each layer and the corresponding type of activation function mentioned. Right: Evolution of the mean squared loss function versus epoch size during the training and validation runs of the proposed deep neural network [144, 145].

neural network. Both the training and validation curves show a quick fall between epoch sizes 0 to 5. Thereafter, the loss function keeps decreasing smoothly with the increase in the epoch size. After a particular epoch, the training is called back using the early stopping mechanism as the losses start to saturate. This also ensures minimal over-fitting. At the final epoch, the model achieves a loss difference of the order of 10^{-4} between the losses of training and validation curves. This is reasonable for optimal training. The training for the DNN estimator is now complete, and the model parameters are frozen.

To further validate the training on a testing dataset, we obtain the event-by-event predictions for v_2 from the DNN model and plot it against the actual values of 10K minimum bias Pb–Pb collisions at $\sqrt{s_{\rm NN}} = 5.02$ TeV from AMPT simulation as shown in the left plot of Fig. 5.5. The mean absolute error (MAE),

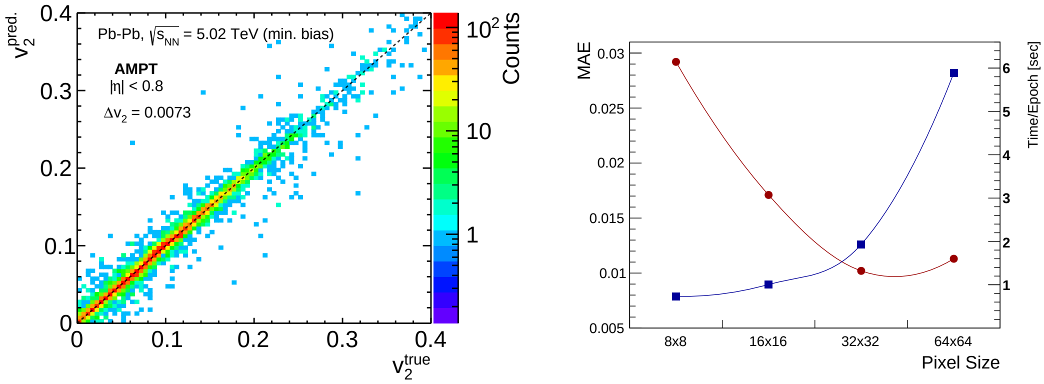

Figure 5.5: Left: Event-by-event predictions versus the true values of elliptic flow plotted for 10K minimum bias Pb–Pb collisions at $\sqrt{s_{\rm NN}}$ = 5.02 TeV from the AMPT model. Right: Mean absolute error on testing data and time/epoch in seconds during training for various input bin size [144, 145]

which is defined in Eq. 5.8, is found to be $\Delta v_2 = 0.0073$. The DNN achieves a decent accuracy as the $v_2^{\rm pred.} = v_2^{\rm true}$, shown as a dashed line, is densely populated, indicating a one-to-one correlation between the machine prediction and true values of v_2.

$$\Delta v_2(\mathrm{MAE}) = \frac{1}{N_{\rm events}} \sum_{n=1}^{N_{\rm events}} |v_{2_n}^{\rm true} - v_{2_n}^{\rm pred.}| \tag{5.8}$$

Table 5.1: Benchmarking of the DNN estimator with different input bin sizes in the $(\eta - \phi)$ space for training with 50K events and testing with 5K events.

Bin size	Input neurons	MAE	Epoch	Time(sec)/Epoch	Trainable parameters
8×8	192	0.0292	18	1.679	189,569
16×16	768	0.0171	28	1.909	263,297
32×32	3072	0.0102	30	2.684	558,209
64×64	12288	0.0113	60	6.001	1,737,857

To further evaluate the effect of input bin size, the DNN model is trained and tested across a number of different input bin sizes. The training is done in the same settings as reported earlier in this section, with 50K training events and 5K testing events. The performance of the DNN model is reported in Tab. 5.1 for 8×8, 16×16, 32×32, and 64×64 bin sizes. The right plot of Fig. 5.5 also shows the MAE on testing data and time/epoch in seconds during training for various input bin sizes. By increasing the input bin size, the MAE starts to decrease; however, it starts to rise for the final case with 64×64 bin size, giving a minimum of $\Delta v_2 = 0.0102$ for 32×32 bin size. The training time per epoch in seconds shows a smooth rising trend with increasing bin size. This rise in the training time is due to the increased number of input neurons and trainable parameters with increasing bin size. However, the model with 64×64 bin size takes almost thrice the time required for the training of the model with 32×32 bin size. Therefore, the optimal choice of the input bin size is taken to be 32×32 with respect to prediction accuracy and efficient training time. This bench-marking is performed on a machine with Intel (R) Core(TM) i5-8279U (released Q2'19), which has four cores (eight threads) clocked at a base frequency of 2.40 GHz and has a max turbo boost frequency of 4.10 GHz [165]. The system has 8 GB of LPDDR3 RAM clocked at 2133 MHz. Slight discrepancies in the benchmarking values are expected by using different machine configurations due to the stochastic nature of the training process.

5.3.4 Systematic uncertainty

In experiments, the measured track-level information is usually convoluted with several detector effects. This appears in the measured quantity as a shift of the mean, a change of the variance, or both. Thus, the input features considered in this study can also suffer from these effects. To test the sensitivity of the proposed DNN estimator, the model is first trained on a dataset without any noise, and then the trained model is tested on a noisy dataset. The additional noise factor is randomly generated following the recipe mentioned below.

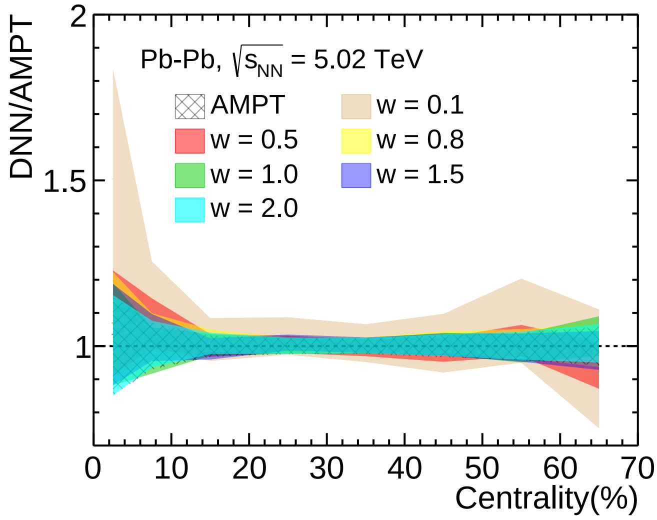

Figure 5.6: The DNN model predictions on a noisy dataset compared to the AMPT simulation without any noise. The smaller value of the parameter w corresponds to a greater noise in the dataset [144].

If we denote the value of j^{th} feature in i^{th} event to be $F_{i,j}$, then we can evaluate the standard deviation associated with j^{th} feature as σ_j. In large events limit, each of these features should describe a Gaussian density profile, following the central limit theorem. Here, we assume that any noise, $X_{i,j}$, associated with $F_{i,j}$ should be proportional to a random number in $(-\sigma_j, \sigma_j)$. Thus, we can generate noise such that $X_{i,j} \in (-\sigma_j, \sigma_j)$ by assuming a random uniform distribution. Now, we introduce a weight factor w, which can control the degree of the noise. Finally, we can obtain the feature value convoluted with noise, $F^*_{i,j}$, given as, $F_{i,j} \to F^*_{i,j} = F_{i,j} + X_{i,j}/w$. The factor w can control the width of the final distribution, as a smaller value of w would broaden the width of the feature distribution and change its true shape. Hence, a smaller value of w corresponds to a higher magnitude of noise and *vice versa*.

Figure 5.6 shows the DNN model predictions on a noisy dataset compared to the AMPT simulation without any noise by varying the degree of noise from low to high [144]. The ratio shows the degree of agreement between the machine prediction and the simulation. If the model is stable and robust to additional noise, the ratio should be exactly equal to one. The width of the bands shows the statistical uncertainty associated with each centrality class. It is observed that smaller values of w (*e.g.*, $w = 0.1$), which induce a greater noise to the data, result in a larger deviation from the true value. However, for a reasonable degree of noise, *e.g.*, $w = 0.5$, the model predictions are indeed close to the true values, meaning the model is quite robust and stable, and it is not very sensitive to the presence of additional noise in the data. For a given centrality bin with noise factor $w = 0.5$, the maximum deviation of the DNN model from simulation can be taken as the systematic uncertainty associated with the same centrality bin. The estimated systematic uncertainties are then assigned to the centrality-wise predictions described in Fig. 5.7. In the absence of detector-level simulation, this method provides a reasonable estimation of the systematic uncertainties; however, studying the model with full detector-level simulation can be taken as an outlook of the current study, and it is not covered in this work.

Before going to the discussion of results obtained using the DNN estimator, we would like to emphasize here that convolutional neural networks (CNN) and PointNet models have recently gained popularity in addressing similar supervised regression problems such as the estimation of impact parameter in high-energy heavy-ion collisions by using image-like inputs [158, 166, 167]. Thus, we also encourage the exploration of CNN- and PointNet-model-based approaches for the estimation of elliptic flow and higher-order flow coefficients, which are specialized algorithms for handling image-like inputs, and it is beyond the scope of the current study.

5.4 Results

In this section, the model predictions for the centrality, energy, and transverse momentum dependence of elliptic flow for all charged particles and identified light-flavor hadrons are discussed. The constituent quark number scaling, the evolution of the crossing point of baryon-meson elliptic flow, and the effect of p_{T} dependent training on the prediction of v_2 are also covered in this section.

5.4.1 Centrality and energy dependence

Figure 5.7 represents the DNN predictions for the centrality dependence of p_{T}-integrated elliptic flow for Pb–Pb collisions at $\sqrt{s_{\mathrm{NN}}} = 2.76$ and 5.02 TeV [144]. Results from AMPT simulation and ALICE [115] are shown for comparison. The DNN, AMPT, and ALICE results are shown in red, blue, and black markers, respectively. The solid and checked red bands represent the bin-wise statistical and systematic uncertainties, respectively. With the current settings and similar kinematics cuts, the AMPT string melting model can describe the centrality dependence of elliptic flow data from ALICE for both collision energies. This is also presented in the bottom ratio plots, where the ratio of AMPT to data lies close to unity across the centrality classes. However, for the extreme centrality bins *i.e.*, $(0-10)\%$ and $(60-70)\%$ case, AMPT has a larger deviation from ALICE compared to the other centrality bins. This might be the result of different flow estimation methods adopted in AMPT and ALICE. For ALICE, a two-particle correlation method with $|\Delta\eta| > 1.0$ is used, whereas for the AMPT case, we use the standard event-plane technique for the elliptic flow estimation.

The DNN predictions for the centrality dependence of elliptic flow are in excellent agreement with AMPT for both collision energies. This is evident from the bottom-most DNN to AMPT ratio plots, which lie flat on the unity line for all the centrality bins. This suggests that the DNN model, trained at one

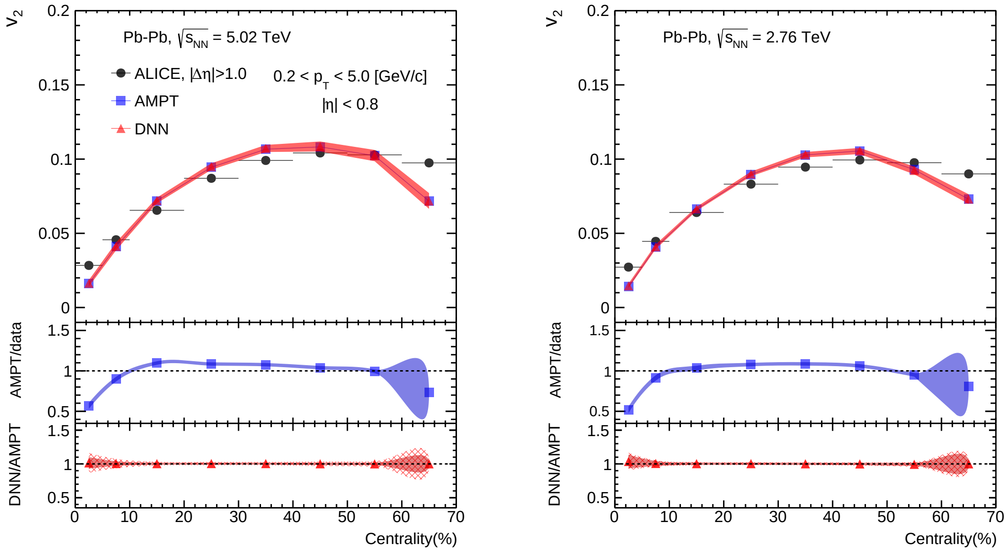

Figure 5.7: DNN predictions for the centrality dependence of p_{T}-integrated elliptic flow for Pb–Pb collisions at $\sqrt{s_{\mathrm{NN}}}$ = 2.76 and 5.02 TeV [144]. Results from AMPT simulation and ALICE [115] are shown for comparison.

energy, *i.e.*, Pb–Pb collisions at $\sqrt{s_{\mathrm{NN}}}$ = 5.02 TeV, can successfully estimate the elliptic flow at another energy, *i.e.*, Pb–Pb collisions at $\sqrt{s_{\mathrm{NN}}}$ = 2.76 TeV along with the same energy it is trained on. By training the model with the selected input features on a minimum bias dataset at a higher collision energy, the DNN model can learn and preserve the particle correlations to estimate the individual centrality-wise elliptic flow coefficients at the same or lower energies. This becomes more convincing from Fig. 5.8, where the DNN estimator is applied to different collision systems across RHIC to LHC energies.

Figure 5.8 shows the DNN predictions and AMPT results for the transverse momentum dependence of elliptic flow, $v_2(p_{\mathrm{T}})$, for $\pi^{\pm}$, $\mathrm{K}^{\pm}$, and $\mathrm{p}+\bar{\mathrm{p}}$, and all charged hadrons ($h^{\pm}$). The results include Au–Au collisions at $\sqrt{s_{\mathrm{NN}}}$ = 200 GeV, Pb–Pb collisions at $\sqrt{s_{\mathrm{NN}}}$ = 2.76 and 5.02 TeV, and Xe–Xe collisions at $\sqrt{s_{\mathrm{NN}}}$ = 5.44 TeV [145]. The measurements for the top central $(0-10)\%$, mid-central $(40-50)\%$, and a peripheral $(60-70)\%$ cases are shown. Similar to Fig. 5.7, a

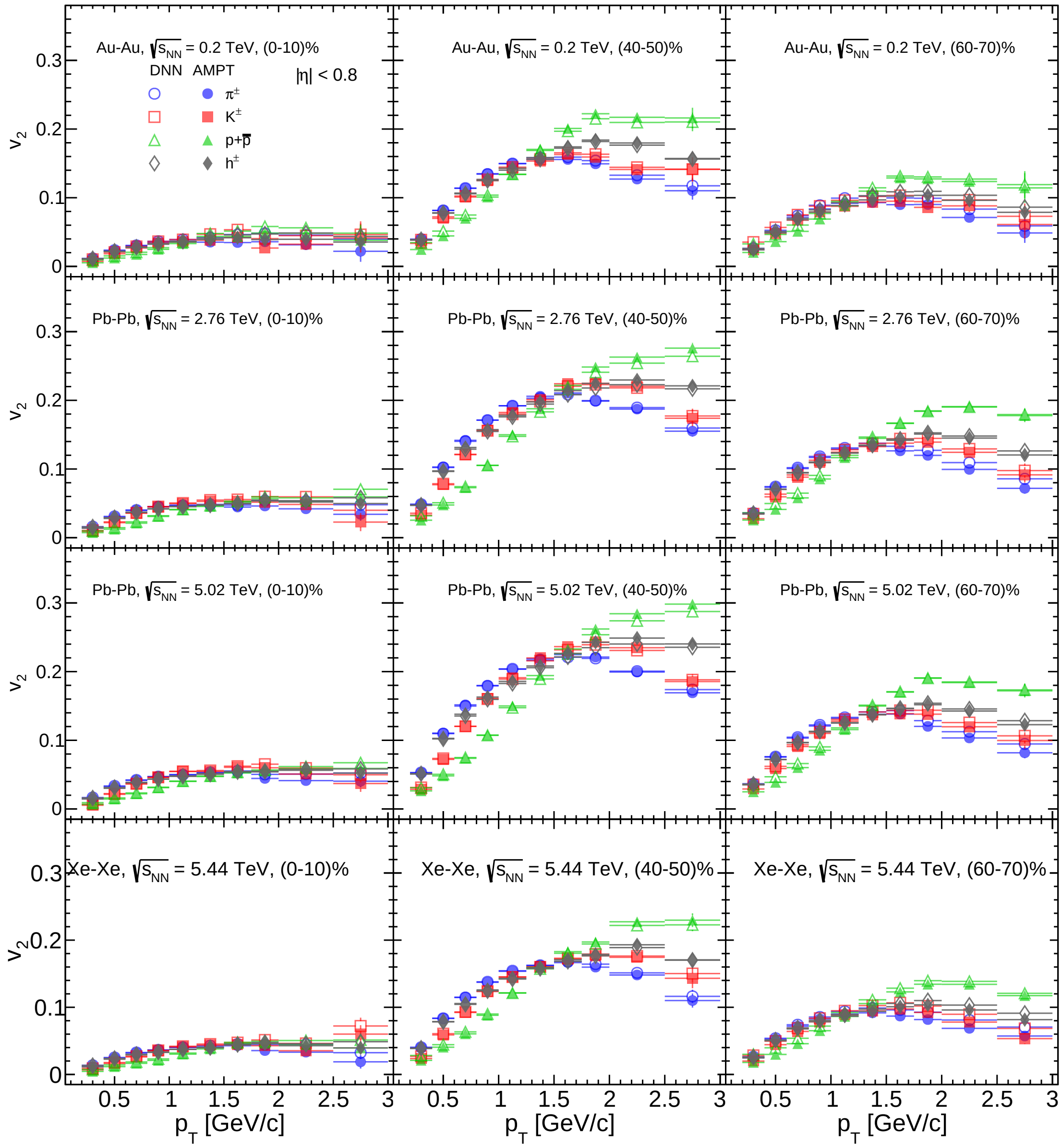

Figure 5.8: DNN predictions and AMPT results for the transverse momentum dependence of elliptic flow for $\pi^{\pm}$, $K^{\pm}$, and $p+\bar{p}$, and all charged hadrons ($h^{\pm}$) [145].

clear centrality dependence of elliptic flow is also observed in Fig. 5.8, as the initial geometrical anisotropy keeps on increasing from central to peripheral collisions, so does the elliptic flow; however, due to the smaller size and shorter lifetime of the QGP fireball towards the most peripheral collisions, the initial spatial anisotropy does not get fully transformed into the final state particle azimuthal anisotropy. This reduces the value of elliptic flow in $(60-70)\%$ centrality case as compared to the mid-central collisions. In the low transverse momentum region, (*i.e.*, $p_{\rm T} \lesssim 1.5$ GeV/c), a mass ordering of $v_2(p_{\rm T})$ is observed, with the lighter particles having more elliptic flow than the heavier ones, following the order, $v_2^{\pi^\pm} > v_2^{K^\pm} > v_2^{p+\bar{p}}$. This behavior is usually attributed to the presence of strong radial flow in the medium, which imposes an azimuthally symmetric velocity boost to all particles along with the hydrodynamic response of the initial spatial anisotropy. However, in the intermediate-$p_{\rm T}$, the baryon and meson $v_2(p_{\rm T})$ split up into two distinct branches with $v_2^{\rm (Baryons)} > v_2^{\rm (Mesons)}$. This effect could arise from the quark recombination mechanism of hadronization, which plays a dominant role at the intermediate-$p_{\rm T}$ and is already implemented in the AMPT string melting model [168].

Now, to compare between the $v_2(p_{\rm T})$ trends of DNN and AMPT, the DNN-to-AMPT ratio is plotted in Fig. 5.9 for $\pi^\pm$, $\rm K^\pm$, and $\rm p+\bar{p}$, and all charged hadrons ($h^\pm$) [145]. The results for Au–Au collisions at $\sqrt{s_{\rm NN}} = 200$ GeV, Pb–Pb collisions at $\sqrt{s_{\rm NN}} = 2.76$ and 5.02 TeV, and Xe–Xe collisions at $\sqrt{s_{\rm NN}} = 5.44$ TeV in $(0-10)\%$, $(40-50)\%$, and $(60-70)\%$ centrality cases have been shown. For the mid-central case, the DNN-to-AMPT ratio is almost one, indicating excellent agreement between the prediction and true values. However, for the most central and peripheral cases, a larger deviation with higher statistical uncertainty is seen across all the collision systems. Similar effects can also be seen in the DNN-to-AMPT ratio plots for the extreme centrality bins in Fig. 5.7. We argue that this effect is purely statistics-driven since in a minimum bias training dataset, the probability of events occupying the extreme centrality bins is quite less as compared to the mid-central collisions. As the current model is trained with a minimum bias dataset, it is exposed to a limited number of examples from both these extreme centrality bins. Similarly, the slight mismatch of the proton v_2 at low-$p_{\rm T}$ and the pion v_2 at intermediate-$p_{\rm T}$ can also be attributed

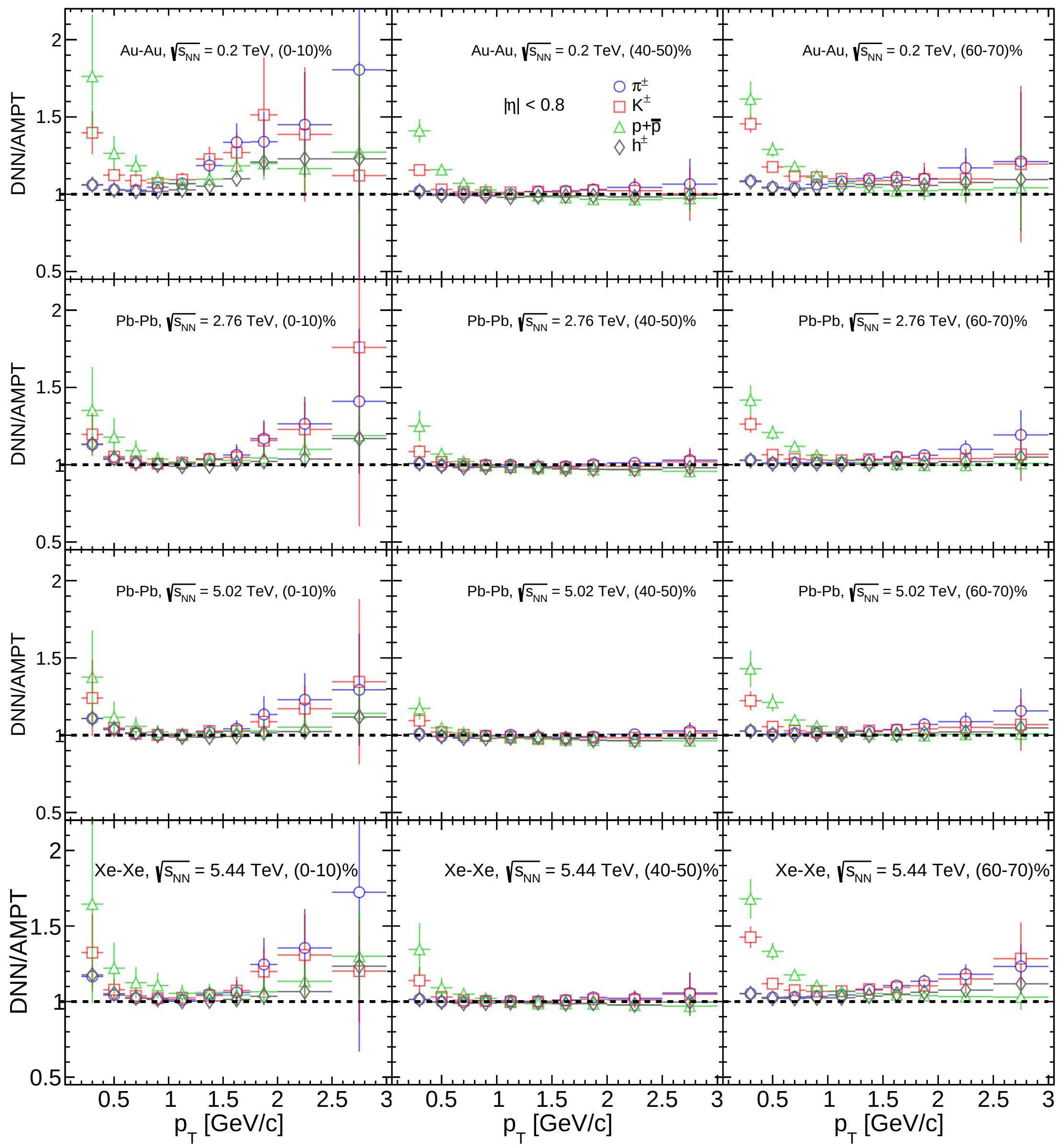

Figure 5.9: Ratio of DNN predictions to AMPT results for the transverse momentum dependence of elliptic flow for $\pi^{\pm}$, $K^{\pm}$, and $p + \bar{p}$, and all charged hadrons ($h^{\pm}$) [145].

to the lack of the training statistics in the respective p_T domains. To solve this issue, we suggest using a collaborative learning model for deep neural networks as described in Ref. [169]. The collaborative learning models can build one single

DNN model while being trained on different types of data with the same input features, irrespective of the sample size. This means the DNN estimator can be trained individually on centrality-wise data with different numbers of events in each centrality, yet having a single set of optimized model parameters. This could possibly solve this issue of training sample bias due to different numbers of events in different centrality bins. This is out of the scope of the present study, and it is not covered here.

5.4.2 Constituent quark number scaling

At low-p_{T}, the mass of the particle plays an important role in generating v_2 as seen from the observed mass ordering at lower p_{T} regime in Fig. 5.8. If the mass ordering is driven by the hydrodynamic expansion of the medium having spatial pressure gradients, then the observed $v_2(E_{\mathrm{T}}^{\mathrm{kin.}})$ should be identical for all particle types at low-p_{T}. Here, $E_{\mathrm{T}}^{\mathrm{kin.}} = m_{\mathrm{T}} - m_0$ is the transverse kinetic energy, $m_{\mathrm{T}} = \sqrt{p_{\mathrm{T}}^2 + m_0^2}$, is the transverse mass and m_0 is the rest mass of the particle. This kinetic energy scaling of elliptic flow at low-p_{T} is indeed observed in experiments [124]. At intermediate-p_{T}, $v_2(E_{\mathrm{T}}^{\mathrm{kin.}})$ divides into two branches grouped by baryons and mesons separately. In this regime, the constituent quarks play a significant role in delivering flow to the hadrons instead of the mass of the hadrons. When the constituent quark number scaling is applied to $v_2(E_{\mathrm{T}}^{\mathrm{kin.}})$, it shows a better scaling than $v_2(p_{\mathrm{T}})$ [124].

Figure 5.10 shows $v_2(E_{\mathrm{T}}^{\mathrm{kin.}}/n_q)$ for Au–Au collisions at $\sqrt{s_{\mathrm{NN}}} = 200$ GeV, Pb–Pb collisions at $\sqrt{s_{\mathrm{NN}}} = 2.76$ and 5.02 TeV, and Xe–Xe collisions at $\sqrt{s_{\mathrm{NN}}} = 5.44$ TeV in $(0-10)\%$, $(40-50)\%$, and $(60-70)\%$ centrality cases [145]. The predictions from the DNN estimator are shown along with the AMPT values. Here, for baryons, the number of constituent quarks, $n_q = 3$, and for mesons, $n_q = 2$. The scaling seems to be valid for all particles at lower $E_{\mathrm{T}}^{\mathrm{kin.}}/n_q$; however, the proton seems to break the scaling at intermediate $E_{\mathrm{T}}^{\mathrm{kin.}}/n_q$. The violation

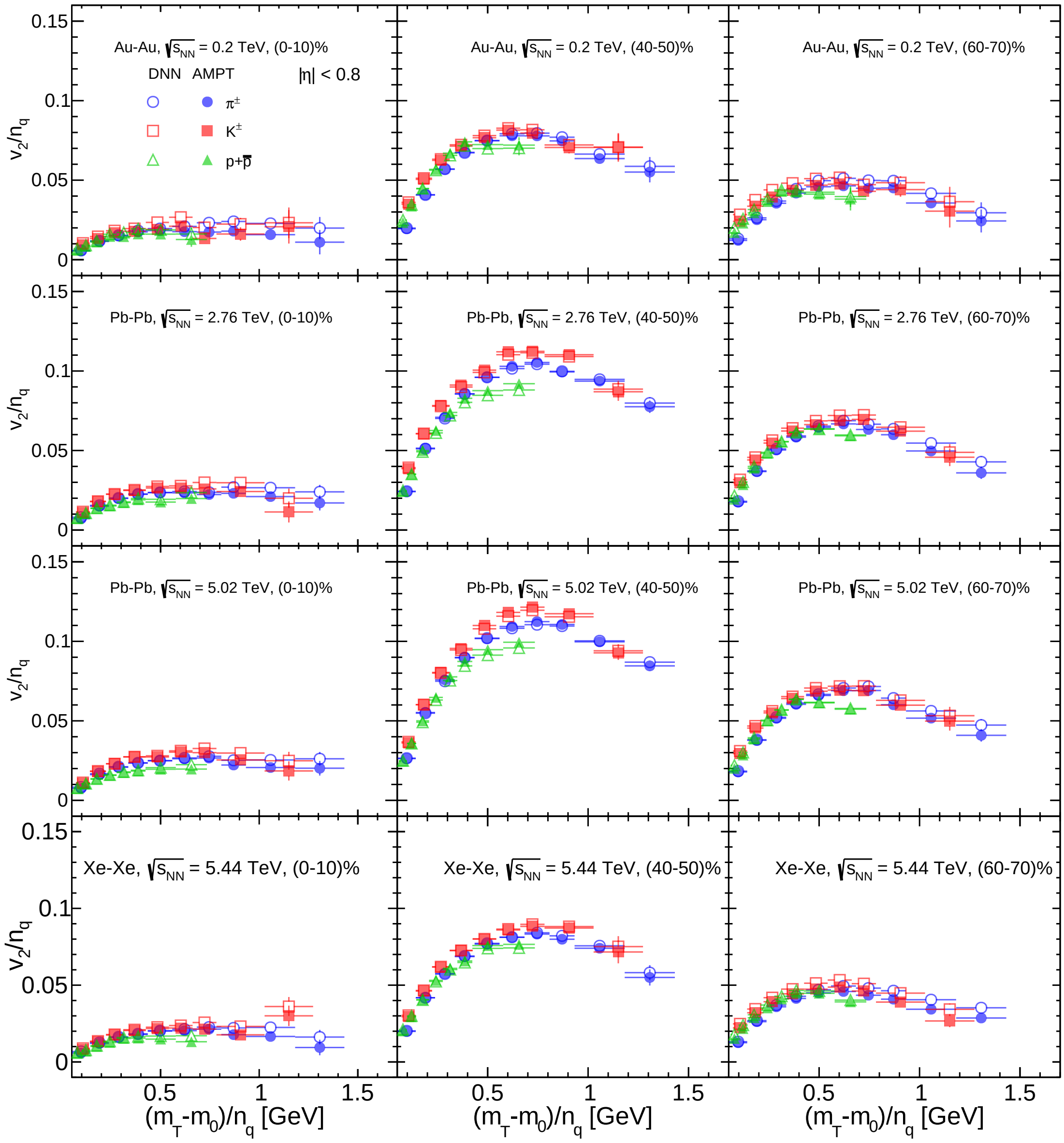

Figure 5.10: DNN predictions and AMPT results for the constituent quark number scaling in different centrality classes in different collision systems from RHIC to LHC energies [145].

of scaling is more prominent at the LHC energy than at RHIC. Similar scaling behavior has been reported in Refs. [114, 170]. The DNN predictions are in line with the AMPT values. This suggests that the proposed DNN estimator can recover the particle-species-dependent scaling behavior for different centrality classes for different collision systems from RHIC to LHC energies. Since the input features and the particle correlations that are fed to the DNN estimator are obtained from AMPT simulation, it is expected that the DNN trends follow the AMPT values closely as reported in Fig. 5.8 and 5.10.

5.4.3 Evolution of crossing point

The appearance of higher flow for baryons than mesons and a relative enhancement of baryon yield over meson yield at intermediate p_{T} are usually accredited to the quark coalescence picture of hadronization. This behavior is well described by theoretical models having the quark recombination mechanism. However, by studying the crossing point in p_{T} where the separation of baryon-meson elliptic flow occurs, one can also confirm the coalescence picture if the p_{T}-crossing point depends on the centrality, such that the crossing occurs at higher momenta towards the central collisions. As the p_{T}-crossing point separates the baryon-meson dependent elliptic flow behavior at intermediate p_{T} from their mass-dependent behavior at low p_{T}, it shows the transition to the dominance of constituent quarks from the dominance of mass of the hadrons in generating elliptic flow in the medium.

Figure 5.11 shows the p_{T}-crossing point ($p_{\mathrm{T}}^{\mathrm{cross}}$) between the pion and proton elliptic flow for different centrality classes in various collision systems considered in this study [145]. The vertical error bars represent the difference between pion-proton and kaon-proton crossing points in p_{T}. The ALICE results are also presented for comparison [111, 171, 172]. From the first glance, it is observed that the $p_{\mathrm{T}}^{\mathrm{cross}}$ gradually shifts towards higher transverse momenta while moving from peripheral to central collisions. Also, the $p_{\mathrm{T}}^{\mathrm{cross}}$ shows energy dependence with crossing occurring at slightly higher p_{T} at higher collision energies. The shift of $p_{\mathrm{T}}^{\mathrm{cross}}$ to higher transverse momenta occurs due to the formation of a denser

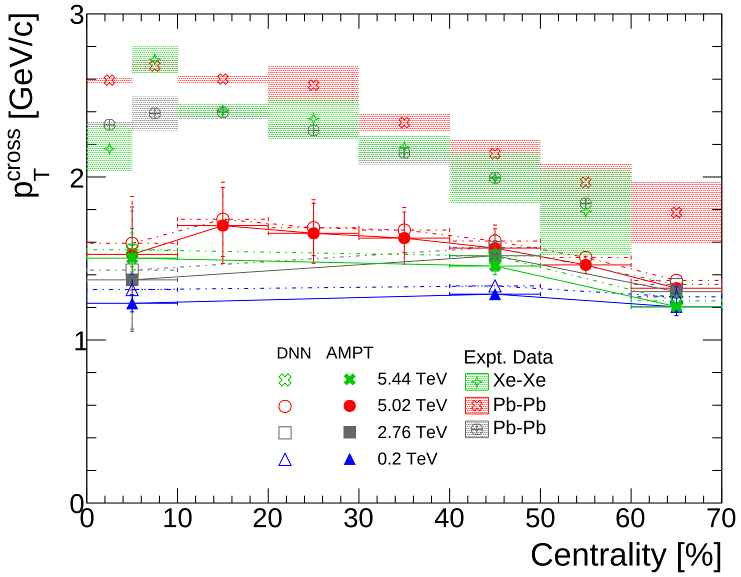

Figure 5.11: The baryon-meson elliptic flow crossing point, $p_{\mathrm{T}}^{\mathrm{cross}}$, at the intermediate p_{T} regime plotted against the centrality of the collisions [145]. The ALICE results are obtained from Refs. [111, 171, 172].

partonic medium and the presence of stronger radial flow towards the higher centrality and higher collision energy. This effect is observed both in the AMPT simulation with quark coalescence picture and the ALICE results. However, the AMPT curves only reproduce the qualitative trend as compared to ALICE. The DNN predictions closely follow the AMPT curves for all the systems under study, meaning the DNN estimator can not only predict the identified light-flavor elliptic flow but also retain the information of their p_{T} crossing points, thus adding a more quantitative hold on the level of prediction for the elliptic flow of identified particles.

5.4.4 Effect of transverse-momentum-dependent training

Figure 5.12 shows the effect of transverse-momentum-dependent training on DNN predictions for pion, kaon, and proton elliptic flow separately. The results include the transverse momentum-dependent elliptic flow predictions for $(40-50)\%$ central Pb–Pb collisions at $\sqrt{s_{\rm NN}} = 5.02$ TeV from three different DNN models, each trained with particles in a different transverse momentum range. For testing pur-

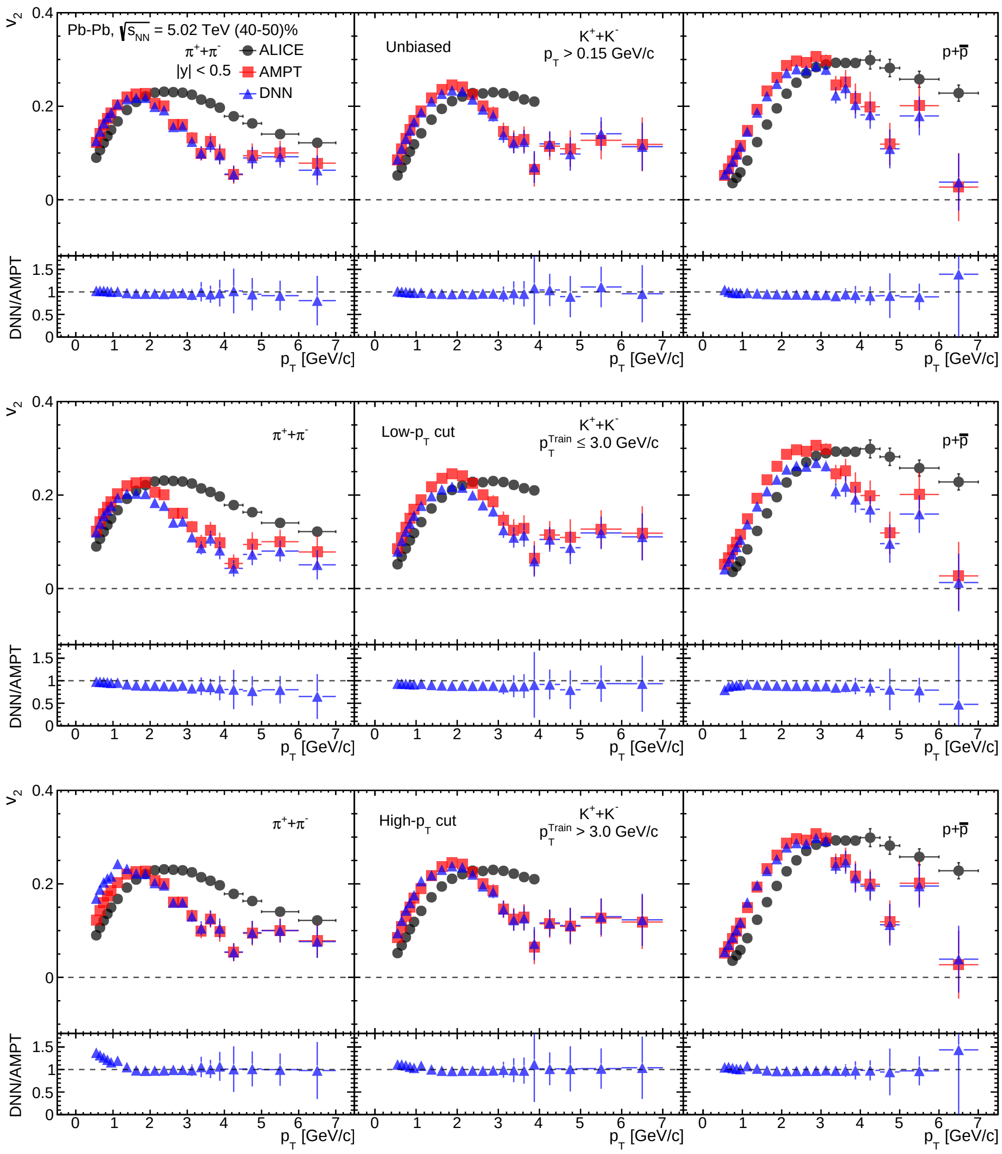

Figure 5.12: Effect of transverse-momentum-dependent training on the DNN predictions of identified particle elliptic flow. The results for $(40-50)\%$ central Pb–Pb collisions at $\sqrt{s_{\rm NN}} = 5.02$ TeV with models trained on an unbiased (top), low-$p_{\rm T}$ (middle), and high-$p_{\rm T}$ (bottom) particle groups are presented [145]. The ALICE results are shown for comparison [171].

poses, however, a similar dataset is used for all three DNN models with particles in $|y| < 0.5$ with $p_{\rm T} > 0.5$ GeV/c. These kinematics cuts have been considered to compare the DNN predictions with the ALICE results [171]. The three models are trained on the minimum bias Pb–Pb collisions at $\sqrt{s_{\rm NN}}$ = 5.02 TeV from AMPT with identical model architecture and hyperparameter settings.

The top panel shows the results from the unbiased training case, where the DNN model is trained with particles in $|\eta| < 0.8$ with $p_{\rm T} > 0.15$ GeV/c. Since the training involves particles for the complete range of $p_{\rm T}$ (shown here up to 7.0 GeV/c), the DNN model is able to capture the maxima of the $v_2(p_{\rm T})$ curve, which is somewhere around, $p_{\rm T}|_{v_2^{\rm max}} \sim 3.0$ GeV/c depending on the particle type. Thus, the DNN model is able to capture the transition behavior of $v_2(p_{\rm T})$ curve with a change of positive (rising in $p_{\rm T}$) to negative (falling in $p_{\rm T}$) slope. The DNN model follows the AMPT curve closely, as can be seen from the bottom ratio plots, where the ratio is fairly lying on top of the unity line. The AMPT values for $v_2(p_{\rm T}) \lesssim 3.0$ GeV/c are in excellent agreement with ALICE; however, beyond this point, the AMPT curves fall faster than that of ALICE. At high-$p_{\rm T}$, elliptic flow suffers significantly from path length-dependent effects such as energy loss due to the high momentum partons traversing the medium along with the fragmentation picture taking over the coalescence mode of hadronization. With a proper description and inclusion of these high-$p_{\rm T}$ effects, AMPT might also be able to describe the $v_2(p_{\rm T})$ trend beyond $p_{\rm T}|_{v_2^{\rm max}} > 3.0$ GeV/c.

Now, to study the transverse-momentum-dependent training effects on the DNN model, we split the training dataset into two groups. The low-$p_{\rm T}$ group comprises of particles in midrapidty ($|\eta| < 0.8$) with $p_{\rm T}^{\rm Train} \leq 3.0$ GeV/c, and the high-$p_{\rm T}$ group comprises of particles in midrapidty ($|\eta| < 0.8$) with $p_{\rm T}^{\rm Train} >$ 3.0 GeV/c. Consequently, this introduces a bias in the DNN training since the transition behavior of $v_2(p_{\rm T})$ around $p_{\rm T}|_{v_2^{\rm max}} \sim 3.0$ GeV/c is captured only in the training dataset of the low-$p_{\rm T}$ group, however, this information is missing in the training dataset of the high-$p_{\rm T}$ group. After the successful training, these two

DNN models are applied to predict the $v_2(p_{\rm T})$ curve in the full $p_{\rm T}$-range. The predictions are shown in the middle and bottom panels of Fig. 5.12 for the low-$p_{\rm T}$ and high-$p_{\rm T}$ group, respectively. Although the models are trained on different particle kinematics information, it is interesting to observe that both the DNN models can explain the full $v_2(p_{\rm T})$ curve up to a reasonable extent by extrapolating the results for the missing regions of training. The particle correlations captured and encoded in the network can somehow reproduce the global curve of $v_2(p_{\rm T})$ including the transition behavior around $p_{\rm T}|_{v_2^{\rm max}}$ irrespective of its domain of training. This fairly indicates that the DNN model adopted in the study using the three layers of input features is capable enough to map the global $p_{\rm T}$ dependence of elliptic flow, although the existence of such a theoretical mapping function is nontrivial in the literature.

On comparing the DNN-to-AMPT ratio plots between the low-$p_{\rm T}$ trained DNN model and the unbiased case, it is observed that for pion and kaon, the model trained on low-$p_{\rm T}$ group deviates from unity only at intermediate to high $p_{\rm T}$. This is expected as the particle kinematics information for $p_{\rm T} > 3.0$ GeV/c is absent in the training. However, the same ratio for proton shows a reverse trend with a significant deviation from unity visible at even low-$p_{\rm T}$. This observation suggests that for the prediction of pion and kaon elliptic flow, the DNN model gains more information from low-$p_{\rm T}$. This is exactly the opposite for the proton case, where more weightage is assigned to the DNN model from high $p_{\rm T}$ particles.

To verify this hypothesis, we can compare the DNN-to-AMPT ratio plots between the high-$p_{\rm T}$ trained DNN model and the unbiased case. Here, since the model lacks the low-$p_{\rm T}$ information, a greater deviation from unity is observed for pion and kaon at low-$p_{\rm T}$ with a very good description for the high-$p_{\rm T}$ part of the curves. However, again, the proton curve shows a peculiar behavior. By training the model with only high-$p_{\rm T}$ particles, the DNN model describes the proton $v_2(p_{\rm T})$ curve reasonably well for the complete $p_{\rm T}$ range. This observation is in line with the last statement of the previous paragraph. This strengthens our understanding that for pion and kaon, the DNN model gains more weightage from the low-p_{T} particles, whereas for the case of proton, the high-p_{T} particles play a more decisive role.

5.5 Summary

To summarize everything discussed so far, this study implements a feed-forward deep neural network estimator to effectively calculate the elliptic flow coefficient in heavy-ion collisions on an event-by-event basis. Input features include three layers of weighted $(\eta - \phi)$ distribution of the final-state particles. This also takes transverse momentum, mass, and a term related to energy as additional input features. The DNN estimator is first trained on simulated minimum bias Pb–Pb collisions at $\sqrt{s_{\mathrm{NN}}} = 5.02$ TeV using AMPT string melting model and then applied to Pb–Pb collisions at $\sqrt{s_{\mathrm{NN}}} = 2.76$ TeV, Xe–Xe collisions at $\sqrt{s_{\mathrm{NN}}} = 5.44$ TeV and Au–Au collisions at $\sqrt{s_{\mathrm{NN}}} = 200$ GeV. The proposed DNN model could successfully reproduce the centrality, transverse momentum, and collision energy dependence of elliptic flow. In addition, the elliptic flow for identified light-flavor hadrons and their constituent quark number scaling behavior could also be predicted using the DNN estimator. In the absence of any detector effects, the current model is exposed to an event-by-event random noise fluctuation to test its stability and accuracy. This also helped estimate the systematic uncertainty. The model is found to be relatively stable and robust under random noise and fluctuation in the dataset. Although the training of the DNN model is time-consuming, applying the fully trained model to estimate elliptic flow is much faster than any of the conventional methods. Additionally, training and testing of the proposed DNN model using actual data can be cumbersome and prone to various detector effects, yet it should be explored to check the applicability of the method. The prediction capability of the ML models for higher-order coefficients can also be explored in the future.

It is worth noting that machine learning models heavily depend on the training dataset, specifically on the input-output correlations. This dataset obtained using Monte Carlo simulations relies on certain underlying physics processes, including model fitting to the experimental data. However, none of the models available in the literature can simultaneously reproduce every feature of the actual data. Hence, the ML models are biased in terms of their training. Since the ML models follow the simulation dataset for their learning, phenomenological models that describe the data as closely as possible should always be preferred for the training.

Chapter 6

Summary and Outlook

In this thesis, the first measurement of event topology dependence of inclusive J/ψ production in pp collisions at $\sqrt{s} = 13$ TeV with ALICE at the LHC has been reported. This study implements transverse spherocity as the event-shape classifier to distinguish events based on their geometrical shape. The forward muon spectrometer of ALICE is used to reconstruct J/ψ in its electromagnetic decay channel, $J/\psi \rightarrow \mu^+\mu^-$. For the estimation of spherocity, midrapidity tracklets ($|\eta| < 0.8$) are reconstructed using the Silicon Pixel Detector, which is the innermost central barrel detector in ALICE. The V0 scintillator detectors with a pseudorapidity coverage of $2.8 < \eta < 5.1$ (V0A) and $-3.7 < \eta < -1.7$ (V0C) have been used for the estimation of event multiplicity. The muon spectrometer is used for the event selection through the unlike-sign dimuon trigger, which is the essential event selection criteria for this analysis. It also measures the muon transverse momentum down to zero p_{T} in the pseudorapidity coverage of $-4.0 < \eta < -2.5$. To improve the spherocity resolution, an additional event selection cut of $N_{\mathrm{tracklets}} \geq 10$ has been imposed. All the measurements are performed in the highest multiplicity class of V0M $(0-10)\%$. We report the dimuon invariant mass distribution, tail parameter estimation, p_{T} differential fit to the invariant mass distribution, p_{T} differential yield extraction for J/ψ

in the jetty, S_0-integrated, and isotropic events. The systematic uncertainty is also estimated by varying the fit ranges and using different sets of empirical fit functions. Finally, the p_{T} differential J/ψ yield ratio of jetty events over S_0-integrated events and isotropic events over S_0-integrated events have been reported. With the current statistics and spherocity resolution, it appears that the inclusive J/ψ production in pp collisions is enhanced in events that are jet dominated. The jetty to S_0-integrated yield ratio is further enhanced at higher p_{T}. This may be due to the increased production of nonprompt J/ψ at high p_{T} in jetty events. Nonprompt J/ψ's are produced from flavor-changing weak decays of beauty hadrons. On the other hand, inclusive J/ψ production is reduced in isotropic events at low and high p_{T}; however, a slight enhancement is observed for the intermediate p_{T}. Overall, the trend of inclusive yield of J/ψ appears to show a reverse trend as compared to the light-flavor hadrons and strange hadrons production in pp collisions. For a solid conclusion, increased statistics and improved spherocity resolution are necessary for such analysis, which can be further addressed in the Run 3 data taking with ALICE at the LHC.

Further, as an outlook of the present analysis, it would be an added advantage if machine learning-based tagging for the prompt and nonprompt J/ψ separation could be performed with ALICE at the LHC. Spherocity as an event classifier can then be applied to study the production of prompt and nonprompt J/ψ and its multiplicity dependence, which can reveal more information about the charm quark production dynamics in the presence of possible QGP-like environment in high-multiplicity pp collisions at the LHC. Such preliminary explorations using machine learning-based taggers have already been reported in Refs. [173, 174]; however, the event topology-based approach is yet to be explored. This can be the next step in studying charm production in high-multiplicity pp collisions in data and MC model-based simulations.

This thesis reports the first implementation of a transverse spherocity-based event-shape technique in heavy-ion collisions to study the second-order anisotropic flow coefficient, elliptic flow (v_2). For this purpose, the AMPT model with string melting mode is used to simulate Pb–Pb collisions at $\sqrt{s_{\rm NN}}$ = 5.02 TeV. This uses a quark coalescence picture for parton to hadron conversion. It is found that transverse spherocity can successfully decouple the events based on their azimuthal topology in heavy-ion collisions. This is evident from the azimuthal momentum correlation (p_x vs. p_y) as a function of spherocity. This study implements the two-particle correlation method for the estimation of elliptic flow. By using a proper pseudorapidity gap between the particle pairs, one can substantially reduce the effect of nonflow from the calculation. This is validated by comparing the estimated elliptic flow between AMPT and PYTHIA models. Since PYTHIA does not include any collective behavior, the resultant flow appears to be zero, which means residual nonflow effects are successfully subtracted from the final flow estimation. The magnitude or the modulation of the two-particle azimuthal correlation function ($C(\Delta\phi)$) depends strongly on spherocity selection. This again adds to the understanding that spherocity can be used as an event shape classifier in heavy-ion collisions. The low-S_0 events produce a stronger correlation signal than the S_0-integrated case, while the high-S_0 events have the smallest signal peaks. This hints towards the presence of a higher elliptic flow component in the low-S_0 events than the S_0-integrated events. High-S_0 events seem to contribute the least to the elliptic flow. The appearance of double peaks in the away-side ($\Delta\phi \sim \pi$) for the high-S_0 events is usually associated with the finite contribution of the third-order harmonic coefficient in the Fourier series or the triangular flow (v_3) in the system. From the elliptic flow trends as a function of transverse momentum and spherocity selection, it is found that spherocity is anti-correlated with the elliptic flow; however, it is slightly positively correlated with the triangular flow. This means that the low-S_0 events show a higher contribution to elliptic flow while the high-S_0 events have a tiny contribution to v_2. By studying the constituent quark (NCQ) scaling behavior with respect to event spherocity, it is found that at RHIC, the NCQ-scaling is valid for S_0-integrated events while it is violated only for the low-S_0 events. However, at the LHC, the NCQ-scaling is violated for both S_0-integrated and low-S_0 events. The deviation from NCQ-scaling is more prominent for low-S_0 events at the LHC energies.

For the first time, we propose a feed-forward deep neural network (DNN) based estimator to effectively calculate the elliptic flow coefficient in heavy-ion collisions on an event-by-event basis. Input features include three layers of weighted $(\eta-\phi)$ distribution of the final-state particles. This also takes transverse momentum, mass, and a term related to energy as additional input features. The DNN estimator is first trained on simulated minimum bias Pb–Pb collisions at $\sqrt{s_{\rm NN}} =$ 5.02 TeV using AMPT string melting model and then applied to Pb–Pb collisions at $\sqrt{s_{\rm NN}} = 2.76$ TeV, Xe–Xe collisions at $\sqrt{s_{\rm NN}} = 5.44$ TeV and Au–Au collisions at $\sqrt{s_{\rm NN}} = 200$ GeV. The proposed DNN model could successfully reproduce the centrality, transverse momentum, and collision energy dependence of elliptic flow. In addition, the elliptic flow for identified light-flavor hadrons and their constituent quark number scaling behavior could also be predicted using the DNN estimator. In the absence of any detector effects, the current model is exposed to an event-by-event random noise fluctuation to test its stability and accuracy. This also helped estimate the systematic uncertainty. The model is found to be relatively stable and robust under random noise and fluctuation in the dataset. Although the training of the DNN model is time-consuming, applying the fully trained model to estimate elliptic flow is much faster than any of the conventional methods.

Bibliography

[1] D. Griffiths, Introduction to elementary particles, 2^{nd} edition, Wiley-Vch (2008).

[2] S. L. Glashow, Nucl. Phys. **22**, 579 (1961).

[3] A. Salam and J. C. Ward, Phys. Lett. **13**, 168 (1964).

[4] S. Weinberg, Phys. Rev. Lett. **19**, 1264 (1967).

[5] Introduction to High Energy Heavy Ion Collision. C.Y. Wong, World Scientific (1994).

[6] H. Perkins, Introduction to High Energy Physics, Cambridge University Press (2012).

[7] A. Deur, S. J. Brodsky and G. F. de Teramond, Nucl. Phys. **90**, 1 (2016).

[8] R. L. Workman *et al.* (Particle Data Group), PTEP **2022**, 083C01 (2022)

[9] "The Frontiers of Nuclear Science, A Long Range Plan," arXiv:0809.3137 [nucl-ex].

[10] S. Borsanyi, G. Endrodi, Z. Fodor, A. Jakovac, S. D. Katz, S. Krieg, C. Ratti and K. K. Szabo, JHEP **11**, 077 (2010).

[11] S. Borsanyi, Z. Fodor, C. Hoelbling, S. D. Katz, S. Krieg and K. K. Szabo, Phys. Lett. B **730**, 99 (2014).

[12] X. Luo, Nucl. Phys. A **956**, 75 (2016).

[13] A. Bazavov *et al.* (HotQCD Collaboration), Phys. Rev. D **90**, 094503 (2014).

[14] W. Busza, K. Rajagopal and W. van der Schee, Ann. Rev. Nucl. Part. Sci. **68**, 339 (2018).

[15] H. Elfner and B. Müller, J. Phys. G **50**, 103001 (2023).

[16] M. Kliemant, R. Sahoo, T. Schuster and R. Stock, Lect. Notes Phys. **785**, 23 (2010).

[17] W. Florkowski, "Phenomenology of Ultra-Relativistic Heavy-Ion Collisions," World Scientific (2010).

[18] https://particlesandfriends.wordpress.com/2016/10/14/evolution-of-collisions-and-qgp/ (Accessed on 07 May 2024)

[19] M. L. Miller, K. Reygers, S. J. Sanders and P. Steinberg, Ann. Rev. Nucl. Part. Sci. **57**, 205 (2007).

[20] J. L. Albacete and C. Marquet, Prog. Part. Nucl. Phys. **76**, 1 (2014).

[21] W. Israel and J. M. Stewart, Annals Phys. **118**, 341 (1979).

[22] H. Song, S. A. Bass, U. Heinz, T. Hirano and C. Shen, Phys. Rev. C **83**, 054910 (2011) [erratum: Phys. Rev. C **86**, 059903 (2012)].

[23] S. Acharya *et al.* (ALICE Collaboration), Eur. Phys. J. C **80**, 693 (2020).

[24] J. Adam *et al.* (ALICE Collaboration), Nature Phys. **13**, 535 (2017).

[25] P. Koch, B. Muller and J. Rafelski, Phys. Rept. **142**, 167 (1986).

[26] U. W. Heinz, Nucl. Phys. A **566**, 205C (1994).

[27] S. Margetis, K. Safarik and O. Villalobos Baillie, Ann. Rev. Nucl. Part. Sci. **50**, 299 (2000).

[28] R. S. Bhalerao, "Relativistic heavy-ion collisions," arXiv:1404.3294 [nucl-th], doi: 10.5170/CERN-2014-001.219

[29] U. Heinz and R. Snellings, Ann. Rev. Nucl. Part. Sci. **63**, 123 (2013).

[30] R. Baier, D. Schiff and B. G. Zakharov, Ann. Rev. Nucl. Part. Sci. **50**, 37 (2000).

[31] T. Niida and Y. Miake, AAPPS Bull. **31**, 12 (2021).

[32] T. Sakaguchi (PHENIX Collaboration), PoS **HardProbes2018**, 035 (2019).

[33] K. Aamodt *et al.* (ALICE Collaboration), Phys. Lett. B **696**, 30 (2011).

[34] S. Chatrchyan *et al.* (CMS Collaboration), Eur. Phys. J. C **72**, 1945 (2012).

[35] T. Matsui and H. Satz, Phys. Lett. B **178**, 416 (1986).

[36] S. Acharya *et al.* (ALICE Collaboration), Phys. Rev. Lett. **132**, 042301 (2024).

[37] A. Adare *et al.* (PHENIX Collaboration), Phys. Rev. Lett. **98**, 232301 (2007).

[38] A. Adare *et al.* (PHENIX Collaboration), Phys. Rev. C **84**, 054912 (2011).

[39] B. Abelev *et al.* (ALICE Collaboration), Phys. Rev. Lett. **109**, 072301 (2012).

[40] R. Sahoo, Springer Proc. Phys. **248**, 357 (2020).

[41] R. Sahoo, AAPPS Bull. **29**, 16 (2019).

[42] R. Sahoo and T. K. Nayak, Curr. Sci. **121**, 1403 (2021).

[43] V. Khachatryan *et al.* (CMS Collaboration), Phys. Lett. B **765**, 193 (2017).

[44] T. Sjöstrand, arXiv:1310.8073 [hep-ph].

[45] A. Ortiz, G. Paic and E. Cuautle, Nucl. Phys. A **941**, 78 (2015).

[46] A. Ortiz, Adv. Ser. Direct. High Energy Phys. **29**, 343 (2018).

[47] G. Bencédi (ALICE Collaboration), Nucl. Phys. A **982**, 507 (2019).

[48] A. Banfi, G. P. Salam and G. Zanderighi, JHEP **1006**, 038 (2010).

[49] L. Evans and P. Bryant, JINST **3**, S08001 (2008).

[50] G. Aad *et al.* (ATLAS Collaboration), JINST **3**, S08003 (2008).

[51] S. Chatrchyan *et al.* (CMS Collaboration), JINST **3**, S08004 (2008).

[52] A. A. Alves, Jr. *et al.* (LHCb Collaboration), JINST **3**, S08005 (2008).

[53] K. Aamodt *et al.* (ALICE Collaboration), JINST **3**, S08002 (2008).

[54] https://cds.cern.ch/record/2800984 (Accessed on 18 Apr 2024)

[55] https://cds.cern.ch/record/2263642 (Accessed on 18 Apr 2024)

[56] B. Abelev *et al.* (ALICE Collaboration), J. Phys. G **41**, 087002 (2014).

[57] E. Bruna, A. Dainese, M. Masera, and F. Prino, https://cds.cern.ch/record/1225497.

[58] D. Elia, B. Ghidini, and M. Nicassio, https://cds.cern.ch/record/1225499.

[59] ALICE Collaboration, P. Cortese et al., "ALICE technical design report on forward detectors: FMD, T0 and V0," CERN-LHCC-2004-025.

[60] E. Abbas *et al.* (ALICE Collaboration), JINST **8**, P10016 (2013).

[61] ALICE Collaboration, “ALICE technical design report of the dimuon forward spectrometer,” CERN-LHCC-99-22.

[62] ALICE Collaboration, C. W. Fabjan, L. Jirdén, V. Lindestruth, L. Riccati, D. Rorich, P. Van de Vyvre, O. Villalobos Baillie, and H. de Groot, ALICE trigger data-acquisition high-level trigger and control system: Technical Design Report. Technical Design Report ALICE. CERN, Geneva, 2004. http://cds.cern.ch/record/684651.

[63] H. Engel, T. Alt, T. Breitner, A. G. Ramirez, T. Kollegger, M. Krzewicki, J. Lehrbach, D. Rohr, and U. Kebschull, “The alice high-level trigger read-out upgrade for lhc run 2,” Journal of Instrumentation 11, C01041 (2016).

[64] A. Kurkela and A. Mazeliauskas, Phys. Rev. Lett. **122**, 142301 (2019).

[65] E. Cuautle, R. Jimenez, I. Maldonado, A. Ortiz, G. Paic and E. Perez, arXiv:1404.2372 [hep-ph].

[66] G. P. Salam, Eur. Phys. J. C **67**, 637 (2010).

[67] A. Khuntia, S. Tripathy, A. Bisht and R. Sahoo, J. Phys. G: Nucl. Part. Phys. **48**, 035102 (2021).

[68] S. Tripathy, A. Bisht, R. Sahoo, A. Khuntia and Malavika P. S, Adv. High Energy Phys. 2021, 8822524 (2021).

[69] S. Prasad, N. Mallick, D. Behera, R. Sahoo and S. Tripathy, Sci. Rep. **12**, 3917 (2022).

[70] ALICE Analysis Note on original $\pi/K/p$ as a function of S_0: https://alice-notes.web.cern.ch/system/files/notes/analysis/673/2017-Aug-10-analysis_note-Vislavicius_PIDSpectraVsSpherocity_v4.pdf

[71] ALICE Analysis note of original $N_{\rm ch}$ as a function of S_0: https://alice-notes.web.cern.ch/system/files/notes/analysis/634/2018-Feb-14-analysis_note-ALICE_analysis_note_rev2.pdf

[72] S. Acharya *et al.* (ALICE Collaboration), arXiv:2310.10236 [hep-ex].

[73] I. Bautista, A. F. Téllez and P. Ghosh, Phys. Rev. D **92**, 071504 (2015).

[74] C. Bierlich, G. Gustafson, L. Lönnblad and A. Tarasov, JHEP **03**, 148 (2015).

[75] S. Gieseke, P. Kirchgaeßer and S. Plätzer, Eur. Phys. J. C **78**, 99 (2018).

[76] J. R. Christiansen and P. Z. Skands, JHEP **08**, 003 (2015).

[77] ALICE Analysis Note of Resonance production vs. S_0: https://alice-notes.web.cern.ch/system/files/notes/analysis/961/2023-10-09-Spherocity_ALICE_Analysis_Note_v8.pdf

[78] ALICE Analysis Note of multiplicity dependent J/ψ production in pp collisions at 13 TeV, https://alice-notes.web.cern.ch/system/files/notes/analysis/734/2021-04-19-jpsimult_v9.pdf

[79] J. Y. Ollitrault, Phys. Rev. D **46**, 229 (1992).

[80] J. E. Bernhard, J. S. Moreland and S. A. Bass, Nature Phys. **15**, 1113 (2019).

[81] J. E. Parkkila, A. Onnerstad, S. F. Taghavi, C. Mordasini, A. Bilandzic, M. Virta and D. J. Kim, Phys. Lett. B **835**, 137485 (2022).

[82] G. Aad *et al.* (ATLAS Collaboration), Phys. Rev. C **92**, 034903 (2015).

[83] A. M. Poskanzer and S. A. Voloshin, Phys. Rev. C **58**, 1671 (1998).

[84] Z. W. Lin, C. M. Ko, B. A. Li, B. Zhang and S. Pal, Phys. Rev. C **72**, 064901 (2005).

[85] C. Bierlich, G. Gustafson, L. Lönnblad and H. Shah, JHEP **10**, 134 (2018).

[86] X. N. Wang and M. Gyulassy, Phys. Rev. D **44**, 3501 (1991).

[87] B. Zhang, Comput. Phys. Commun. **109**, 93 (1998).

[88] Z. W. Lin and C. M. Ko, Phys. Rev. C **65**, 034904 (2002).

[89] Y. He and Z. W. Lin, Phys. Rev. C **96**, 014910 (2017).

[90] B. Li, A. T. Sustich, B. Zhang and C. M. Ko, Int. J. Mod. Phys. E **10**, 267 (2001).

[91] B. A. Li and C. M. Ko, Phys. Rev. C **52**, 2037 (1995).

[92] V. Greco, C. M. Ko and P. Levai, Phys. Rev. C **68**, 034904 (2003).

[93] R. J. Fries, B. Muller, C. Nonaka and S. A. Bass, Phys. Rev. Lett. **90**, 202303 (2003).

[94] R. J. Fries, B. Muller, C. Nonaka and S. A. Bass, Phys. Rev. C **68**, 044902 (2003).

[95] S. Tripathy, S. De, M. Younus and R. Sahoo, Phys. Rev. C **98**, 064904 (2018).

[96] C. Loizides, J. Kamin and D. d'Enterria, Phys. Rev. C **97**, 054910 (2018) Erratum: [Phys. Rev. C **99**, 019901 (2019)].

[97] T. Sjöstrand, S. Ask, J. R. Christiansen, R. Corke, N. Desai, P. Ilten, S. Mrenna, S. Prestel, C. O. Rasmussen and P. Z. Skands, Comput. Phys. Commun. **191**, 159-177 (2015).

[98] B. Andersson, G. Gustafson and B. Nilsson-Almqvist, Nucl. Phys. B **281**, 289 (1987).

[99] S. Acharya *et al.* (ALICE Collaboration), Eur. Phys. J. C **79**, 857 (2019).

[100] N. Mallick, R. Sahoo, S. Tripathy and A. Ortiz, J. Phys. G **48**, 045104 (2021).

[101] S. A. Voloshin, A. M. Poskanzer and R. Snellings, Landolt-Bornstein **23**, 293 (2010).

[102] S. Voloshin and Y. Zhang, Z. Phys. C **70**, 665 (1996).

[103] B. B. Abelev et al. (ALICE Collaboration), JHEP **1506**, 190 (2015).

[104] S. A. Voloshin, Nucl. Phys. A **715**, 379 (2003).

[105] D. Molnar and S. A. Voloshin, Phys. Rev. Lett. **91**, 092301 (2003).

[106] H. Sato and K. Yazaki, Phys. Lett. B **98**, 153 (1981).

[107] C. B. Dover, U. W. Heinz, E. Schnedermann and J. Zimanyi, Phys. Rev. C **44**, 1636 (1991).

[108] J. Adams *et al.* (STAR Collaboration), Phys. Rev. Lett. **92**, 052302 (2004).

[109] S. S. Adler *et al.* (PHENIX Collaboration), Phys. Rev. Lett. **91**, 182301 (2003).

[110] K. Aamodt *et al.* (ALICE Collaboration), Phys. Rev. Lett. **105**, 252302 (2010).

[111] B. B. Abelev *et al.* (ALICE Collaboration), JHEP **06**, 190 (2015).

[112] S. Acharya *et al.* (ALICE Collaboration), arXiv:2206.04587 [nucl-ex].

[113] S. Singha and M. Nasim, Phys. Rev. C **93**, 034908 (2016).

[114] N. Mallick, S. Tripathy and R. Sahoo, Eur. Phys. J. C **82**, 524 (2022).

[115] J. Adam *et al.* (ALICE Collaboration), Phys. Rev. Lett. **116**, 132302 (2016).

[116] M. Aaboud *et al.* (ATLAS Collaboration), Phys. Rev. C **96**, 024908 (2017).

[117] G. Aad *et al.* (ATLAS Collaboration), Phys. Rev. C **86**, 014907 (2012).

[118] S. Chatrchyan *et al.* (CMS Collaboration), Phys. Rev. C **89**, 044906 (2014).

[119] K. Aamodt *et al.* (ALICE Collaboration), Phys. Lett. B **708**, 249 (2012).

[120] V. Khachatryan *et al.* (CMS Collaboration), Phys. Rev. C **92**, 034911 (2015).

[121] M. Aaboud *et al.* (ATLAS Collaboration), Eur. Phys. J. C **78**, 142 (2018).

[122] B. I. Abelev *et al.* (STAR Collaboration), Phys. Rev. C **75**, 054906 (2007).

[123] S. Afanasiev *et al.* (PHENIX Collaboration), Phys. Rev. Lett. **99**, 052301 (2007).

[124] A. Adare *et al.* (PHENIX Collaboration), Phys. Rev. Lett. **98**, 162301 (2007).

[125] S. A. Bass, M. Gyulassy, H. Stoecker and W. Greiner, J. Phys. G **25**, R1-R57 (1999).

[126] K. Aamodt *et al.* (ALICE Collaboration), Phys. Rev. Lett. **107**, 032301 (2011).

[127] B. B. Abelev *et al.* (ALICE Collaboration), Phys. Rev. C **90**, 054901 (2014).

[128] M. Csanad, T. Csorgo, A. Ster, B. Lorstad, N. N. Ajitanand, J. M. Alexander, P. Chung, W. G. Holzmann, M. Issah and R. A. Lacey, Eur. Phys. J. A **38**, 363 (2008).

[129] P. F. Kolb, P. Huovinen, U. W. Heinz and H. Heiselberg, Phys. Lett. B **500**, 232 (2001).

[130] B. B. Back *et al.* (PHOBOS Collaboration), Phys. Rev. C **72**, 051901 (2005).

[131] S. A. Bass and A. Dumitru, Phys. Rev. C **61**, 064909 (2000).

[132] C. Nonaka and S. A. Bass, Phys. Rev. C **75**, 014902 (2007).

[133] D. Teaney, J. Lauret and E. V. Shuryak, arXiv:nucl-th/0110037 [nucl-th].

[134] T. Hirano, U. W. Heinz, D. Kharzeev, R. Lacey and Y. Nara, Phys. Lett. B **636**, 299 (2006).

[135] W. Zhao, W. Ke, W. Chen, T. Luo and X. N. Wang, Phys. Rev. Lett. **128**, 022302 (2022).

[136] S. Wang, Y. Z. Jiang, Y. M. Liu, D. Keane, D. Beavis, S. Y. Chu, S. Y. Fung, M. Vient, C. Hartnack and H. Stoecker, Phys. Rev. C **44**, 1091 (1991).

[137] N. Borghini, P. M. Dinh and J. Y. Ollitrault, Phys. Rev. C **63**, 054906 (2001).

[138] R. S. Bhalerao, N. Borghini and J. Y. Ollitrault, Nucl. Phys. A **727**, 373 (2003).

[139] R. S. Bhalerao, J. Y. Ollitrault, S. Pal and D. Teaney, Phys. Rev. Lett. **114**, 152301 (2015).

[140] M. Hippert, D. Dobrigkeit Chinellato, M. Luzum, J. Noronha, T. Nunes da Silva and J. Takahashi, Phys. Rev. C **101**, 034903 (2020).

[141] A. M. Sirunyan *et al.* (CMS Collaboration), Phys. Rev. C **96**, 064902 (2017).

[142] Z. Liu, W. Zhao and H. Song, Eur. Phys. J. C **79**, 870 (2019).

[143] F. G. Gardim, F. Grassi, P. Ishida, M. Luzum and J. Y. Ollitrault, Phys. Rev. C **100**, 054905 (2019).

[144] N. Mallick, S. Prasad, A. N. Mishra, R. Sahoo and G. G. Barnaföldi, Phys. Rev. D **105**, 114022 (2022).

[145] N. Mallick, S. Prasad, A. N. Mishra, R. Sahoo and G. G. Barnaföldi, Phys. Rev. D **107**, 094001 (2023).

[146] Charu C. Aggarwal, Neural Networks and Deep Learning, Springer Cham, ISBN 978-3-031-29642-0 (2023). doi: 10.1007/978-3-031-29642-0

[147] B. H. Denby, Comput. Phys. Commun. **49**, 429 (1988).

[148] L. Lonnblad, C. Peterson and T. Rognvaldsson, Phys. Rev. Lett. **65**, 1321 (1990).

[149] L. de Oliveira, M. Kagan, L. Mackey, B. Nachman and A. Schwartzman, JHEP **07**, 069 (2016).

[150] P. T. Komiske, E. M. Metodiev and M. D. Schwartz, JHEP **01**, 110 (2017).

[151] Y. C. J. Chen, C. W. Chiang, G. Cottin and D. Shih, Phys. Rev. D **101**, 053001 (2020).

[152] S. Farrell, P. Calafiura, M. Mudigonda, Prabhat, D. Anderson, J. R. Vlimant, S. Zheng, J. Bendavid, M. Spiropulu and G. Cerati, *et al.* arXiv:1810.06111 [hep-ex].

[153] D. Belayneh, F. Carminati, A. Farbin, B. Hooberman, G. Khattak, M. Liu, J. Liu, D. Olivito, V. Barin Pacela and M. Pierini, *et al.* Eur. Phys. J. C **80**, 688 (2020).

[154] P. Goncharov, E. Schavelev, A. Nikolskaya and G. Ososkov, AIP Conf. Proc. **2377**, 040004 (2021). arXiv:2109.08982 [physics.data-an].

[155] L. G. Pang, K. Zhou, N. Su, H. Petersen, H. Stöcker and X. N. Wang, Nature Commun. **9**, 210 (2018).

[156] Y. S. Zhao, L. Wang, K. Zhou and X. G. Huang, arXiv:2105.13761 [hep-ph].

[157] G. Bíró, B. Tankó-Bartalis and G. G. Barnaföldi, arXiv:2111.15655 [hep-ph].

[158] P. Xiang, Y. S. Zhao and X. G. Huang, arXiv:2112.03824 [hep-ph].

[159] M. Feickert and B. Nachman, arXiv:2102.02770 [hep-ph]. https://github.com/iml-wg/HEPML-LivingReview

[160] F. Chollet, *et al.* https://keras.io/

[161] M. Abadi, A. Agarwal, P. Barham, E. Brevdo, Z. Chen, C. Citro, G. S. Corrado, A. Davis, J. Dean and M. Devin, *et al.* arXiv:1603.04467 [cs.DC]. https://www.tensorflow.org/

[162] F. Pedregosa *et al.*, J. Mach. Learn. Res. **12**, 2825 (2011). https://dl.acm.org/doi/10.5555/1953048.2078195

[163] X. Glorot, A. Bordes, and Y. Bengio, *Proceedings of the Fourteenth International Conference on Artificial Intelligence and Statistics, Ft. Lauderdale, USA, PMLR Workshop and Conference Proceedings* (2011), pp. 315–323, https://proceedings.mlr.press/v15/glorot11a.html

[164] D. P. Kingma and J. Ba, arXiv:1412.6980 [cs.LG].

[165] Available online: https://www.intel.com/content/www/us/en/products/sku/191070/intel-core-i58279u-processor-6m-cache-up-to-4-10-ghz/specifications.html (Accessed 31 March 2024)

[166] X. Zhang, Y. Huang, W. Lin, X. Liu, H. Zheng, R. Wada, A. Bonasera, Z. Chen, L. Chen and J. Han, *et al.* Phys. Rev. C **105**, 034611 (2022).

[167] M. Omana Kuttan, J. Steinheimer, K. Zhou, A. Redelbach and H. Stoecker, Phys. Lett. B **811**, 135872 (2020).

[168] J. Tian, J. H. Chen, Y. G. Ma, X. Z. Cai, F. Jin, G. L. Ma, S. Zhang and C. Zhong, Phys. Rev. C **79**, 067901 (2009).

[169] G. Song, and W. Chai, arXiv:1805.11761 [stat.ML].

[170] A. Adare *et al.* (PHENIX Collaboration), Phys. Rev. C **85**, 064914 (2012).

[171] S. Acharya *et al.* (ALICE Collaboration), JHEP **09**, 006 (2018).

[172] S. Acharya *et al.* (ALICE Collaboration), JHEP **10**, 152 (2021).

[173] S. Prasad, N. Mallick and R. Sahoo, Phys. Rev. D **109**, 014005 (2024).

[174] K. Goswami, S. Prasad, N. Mallick, R. Sahoo and G. B. Mohanty, arXiv:2404.09839 [hep-ph] [Phys. Rev. D (In press)].